Studying molecule-surface interactions using magnetically manipulated molecular beams

Yosef Alkoby

College of Science

Swansea University

Submitted to Swansea University in fulfilment of the requirements for the degree programme

Doctor of Philosophy

2021

Abstract

Molecular beam techniques contribute crucial knowledge for a wide range of research fields and applications[1, 2]. The goal of this PhD thesis is to contribute to the development of the new magnetic molecular interferometry technique and use it to study fundamentally important molecule-surface systems in their ground state. The thesis describes both surface scattering experiments and the development of new instrumentation and experimental methods which make this technique more powerful and insightful. The development, characterisation and testing of a new direct beam line, capable of magnetically analysing the molecular beam without scattering from a surface, is presented. This new addition to the instrument enables gathering important information about the composition and properties of the molecular beam and its response to magnetic fields. This type of information will be particularly crucial when extending the interferometry technique to molecules where the magnetic Hamiltonian is not well known. Scattering experiments of hydrogen beams from graphene, copper and salt surfaces were performed, gaining unique quantum information about the scattering process. Using magnetic manipulation, we can characterise the different quantum rotational projection states of the molecules before and after scattering from a surface and detect subtle changes in the quantum state during the scattering event.

Both the scattering and the direct beam experiments presented in the thesis, were analysed by solving the magnetic evolution quantum mechanically. The results show that the scattering of hydrogen from a lithium-fluoride (001) surface into different diffraction channels, is highly dependent on the rotational projection states, i.e. the orientation of the molecular rotation of the incident molecules. In contrast, the specular scattering of flat copper, Cu(111), and graphene surfaces shows no obvious change in the rotational state populations upon scattering. Further helium and deuterium beams experiments are presented, enhancing our understanding of the molecular magnetic interferometer and validating our analysis methods.

To Noam and Yuvali ,

"May the good Lord shine a light on you
Make every song your favorite tune
May the good Lord shine a light on you
Warm like the evening sun"

Mick Jagger and Keith Richard

Acknowledgements

First and foremost I am extremely grateful to my supervisors, Prof. Gil Alexandrowicz and Dr. Helen Chadwick for their invaluable advice, continuous support, and patience during my PhD study. Their immense knowledge and plentiful experience have encouraged me in all the time of my academic research and daily life. I would like to thank all the members in the Surface-Science group at Swansea Uneversity. It is their kind help and support that have made my study and life in the UK a wonderful time. Finally, I would like to express my gratitude to my parents, my wife and my son. Without their tremendous understanding and encouragement in the past few years, it would be impossible for me to complete my study.

Declaration

This work has not previously been accepted in substance for any degree and is not being concurrently submitted in candidature for any degree.

Signed [redacted] (candidate)

Date 22/11/21

STATEMENT 1

This thesis is the result of my own investigations, except where otherwise stated. Where correction services have been used, the extent and nature of the correction is clearly marked in a footnote(s). Other sources are acknowledged by footnotes giving explicit references. A bibliography is appended.

Signed [redacted] (candidate)

Date 22/11/21

STATEMENT 2

I hereby give consent for my thesis, if accepted, to be available for photocopying and for inter-library loan, and for the title and summary to be made available to outside organisations.

Signed [redacted] (candidate)

Date 22/11/21

Contents

List of Figures

LIST OF FIGURES

LIST OF FIGURES

List of Tables

LIST OF TABLES

1

Introduction

The interaction between molecules and surfaces is of major importance in many research fields and applications, from star formation in the inter-stellar medium to production of fertilisers [1, 2]. For those fields and applications to develop, it is crucial to know how to calculate the forces between a molecule and a surface, forces which reflect the molecule-surface interaction potential. For example, having such capabilities would allow us to predict the outcome of a surface reaction, search for an ideal catalyst for a surface based reaction or provide useful insights into the mechanism of the reaction and how it can be controlled.

The complexity of gas-surface reactions makes the interaction potential impossible to calculate using accurate quantum mechanical methods, instead calculations are made by using some approximation method technique, usually density functional theory (DFT) [4]. These approximations result in major uncertainties, making it difficult to interpret experimental observations and produce reliable predictions. New, more accurate, theoretical methods are constantly being developed, however this development requires experimental data to compare with and benchmark the accuracy of the theoretical method.

One type of measurement which has been used to benchmark our understanding of surfaces in general, and the interactions of atom and molecules with surfaces in particular, is scattering experiments. A wide range of surface-scattering experiments have been performed over the years, providing insight into both the interaction of the atoms / molecules of the beam with the surface and the surface properties [5, 6]. The knowledge extracted from performing such experiments

depends on what type of scattering experiment is performed. For example, elastic helium scattering measurements can use the diffraction intensities to resolve the surface structure [7], whereas time of flight measurements have the ability to resolve the beam velocity and consequently the time of flight before and after the scattering event, making it possible to study inelastic scattering and characterise the surface phonons [8, 9]. Another scattering technique which is closely related to the methods technique presented in this thesis is helium spin-echo (HSE). [10, 11, 12]. HSE uses magnetic manipulation to measure small changes in the energy of the ^{3}He beam particles due to the collision with the surface. Measuring these energy changes makes it possible to detect ultra-fast motion of atoms and molecules adsorbed on a surface, motion which in turn tells us about forces adsorbed molecules experience.

A sub-category of scattering experiments are those which isolate specific molecular quantum states before and after a collision. These experiments, also known as state-to-state measurements, provide a particularly useful comparison between experiments and theory, as they reduce the number of unknowns and free parameters and the uncertainty they introduce. Typically, molecular states are selected by sophisticated photo-excitation schemes, making them inapplicable to ground state molecules. In this thesis we present the instrumental development and first experimental results of a new scientific instrument called the magnetic molecular interferometer (MMI). The MMI is capable of performing state-to-state experiments of ground state molecules scattering from a surface. The molecular quantum states which are controlled and measured are the nuclear spin states and the rotational projection states, m_J which are the quantum analogue of the orientation of the rotational motion of the molecule.

Fig. 1.1 shows a schematic of the setup, a detailed description of the instrument and the different elements along the beam line is provided in the next chapter. In this setup, a molecular beam is formed and passed through a state selector (magnetic hexapole lens) which creates an initial bias in the populations of the different quantum states of the beam. The beam continues through an electromagnet, B1, which forms a homogeneous magnetic field in the beam path and allows continuous coherent control over the molecular quantum states, and in particular allows us to change the rotational orientation of the molecules which

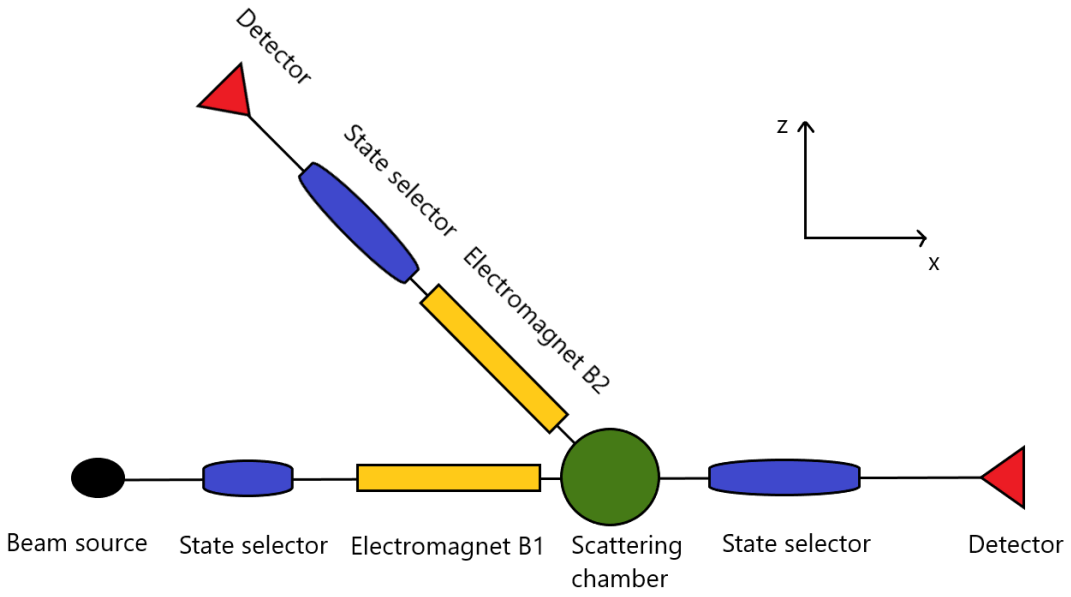

Figure 1.1: Schematic of the machine setup - a representation of the different elements in the machine.

will reach the scattering chamber. Here the beam can either scatter from a surface of a sample or in the absence of a sample, continue along the x axis. In the case of scattering from a surface, the beam enters a second electromagnet (B2) and a second state selection stage before it arrives in the detection region, this combinations of elements allows us to change and measure the quantum states of the scattered molecules. The scattering configuration of the MMI setup allows us to both control and measure the rotational projection states and through this to study how this changes the scattering event. State-to-state scattering experiments performed in this configuration produce interference patterns which provide insight into the molecule-surface interaction potential.

In a non-scattering experiment, the beam exits the scattering chamber in a straight line and enters a second state selector through which it continuous into the detection region. This straight through configuration, which is described in detail in chapter 3, avoids the surface scattering event and the uncertainties this gives rise to, and allows us to measure the behavior of the selected states of the beam while controlling the magnetic field in the first electromagnet. These type

of experiments verify our understanding of the magnetic manipulation techniques and assess the magnetic beam profiles along the beam line. This verification is important for our signal analysis techniques described in chapter 2 and applied in chapter 4 and 5. Furthermore, the ability to perform direct analysis will be important for future studies of molecules where the magnetic Hamiltonian is not yet determined.

The potential of our experimental technique to generate unique benchmarks is demonstrated by the experimental results presented in chapter 4. In this case, the MMI is used to study the collision of a ground state H_2 molecule with a lithium fluoride (LiF) surface. From the results, the scattering matrix in various diffraction channels is extracted. The scattering matrix we are referring to, describes the change of the rotational projection quantum states of the beam molecules (both in terms of magnitude and in terms of phase) during the scattering event. These changes are sensitive to both the long and short term interaction potential between the approaching particle and the surface. While theoretical calculations of scattering matrices exist [13, 14] the ability to check the validity of such calculations, did not exist before the work presented here. The empirical determination of scattering matrix elements is made possible by coherent control over the rotational projection (m_J) quantum states of the beam particle (molecular hydrogen in this case) before and after the collision with the surface. Our results provide an experimental benchmark for any future calculations of the interaction of H_2 with a LiF surface.

The primary gas used in our molecular beam experiments is molecular hydrogen, the most abundant molecule in the universe, which plays an important role in numerous existing and futuristic industrial processes. H_2 also has the advantage that it is a simple molecule, this allows us to simulate its propagation through magnetic fields and also mean that existing theoretical methods have more of a chance to calculate its interaction with surfaces.

1.1 Ground-state hydrogen molecule

Hydrogen molecules are composed of two hydrogen atoms, each one consisting of a proton and electron. The total electronic spin of the ground state is zero,

however the nuclear spin state is more complex and is the result of adding two spin $\frac{1}{2}$ particles. A natural basis to describe the four possible nuclear spin states of the two nuclei would be by the different possible spin $\frac{1}{2}$ projection combinations where $\uparrow$ and $\downarrow$ marks the spin up and down projection states of each proton i.e, $|\uparrow\uparrow\rangle\,|\uparrow\downarrow\rangle\,|\downarrow\uparrow\rangle$ and $|\uparrow\uparrow\rangle$. However, it is convenient to change to a different basis which can be expressed as a superposition of these states:

- combinations which have a total spin, I=1, and the following spin projections:

$$\begin{aligned} m_I = 1 \qquad & |\uparrow\uparrow\rangle\,, \\ m_I = 0 \quad & \tfrac{1}{\sqrt{2}}[|\uparrow\downarrow\rangle + |\downarrow\uparrow\rangle\,, \\ m_I = -1 \qquad & |\downarrow\downarrow\rangle\,, \end{aligned} \tag{1.1}$$

- and combinations which have a total spin, I=0, and just one spin projection

$$m_I = 0 \quad \tfrac{1}{\sqrt{2}}[|\uparrow\downarrow\rangle - |\downarrow\uparrow\rangle\,. \tag{1.2}$$

The first three states, form one type of spin isomer, a triplet, which has a total spin I=1 (can be seen by applying the total spin operator to the linear combinations) are referred to as ortho-hydrogen ($o-H_2$). The second spin isomer is the singlet I=0, with a projection of $m_I = 0$, referred to as para-hydrogen ($p-H_2$). The advantage of this alternative basis is that it separates the states into two groups with well-defined symmetries which has implications for the rotational states. The three I=1 states are symmetric with respect to proton interchange. Since the protons themself are fermions, the total wavefunction of H_2 should be antisymmetric with respect to particle exchange. This forces the I=1 states to have antisymmetric rotational wavefunction corresponding to odd J, where J marks the total rotational quantum number. Similar arguments lead to the fact that the single I=0 state has to have symmetric rotational wavefunctions corresponding to even J.

A ground state molecular ensemble is made of mixture of $o-H_2$ and $p-H_2$ molecules with rotational quantum numbers J=1 and J=0 respectively and a relative population weight of 3:1 due to the different number of spin projection

states. In our molecular beam experiments, due to the cold temperature of the expansion, the additional cooling in the jet expansion and the relatively large spacing between rotational states in hydrogen, we are not expecting any other rotational state to be populated significantly.

1.1.1 Rotational states

Molecules with J=0 do not rotate and have no angular momentum. Molecules in the J=1 states have 3 different projections of their angular momentum on some axis (the quantisation axis) , $m_J = -1, 0, 1$. These projections represent how the molecules are rotating in space. Let us look at an example where the molecules approach a surface and we choose a quantisation axis which is perpendicular to that surface. Fig. 1.2 illustrates the orientation and the different rotations with respect to the surface environment. Molecules with $m_J = 0$ will rotate as

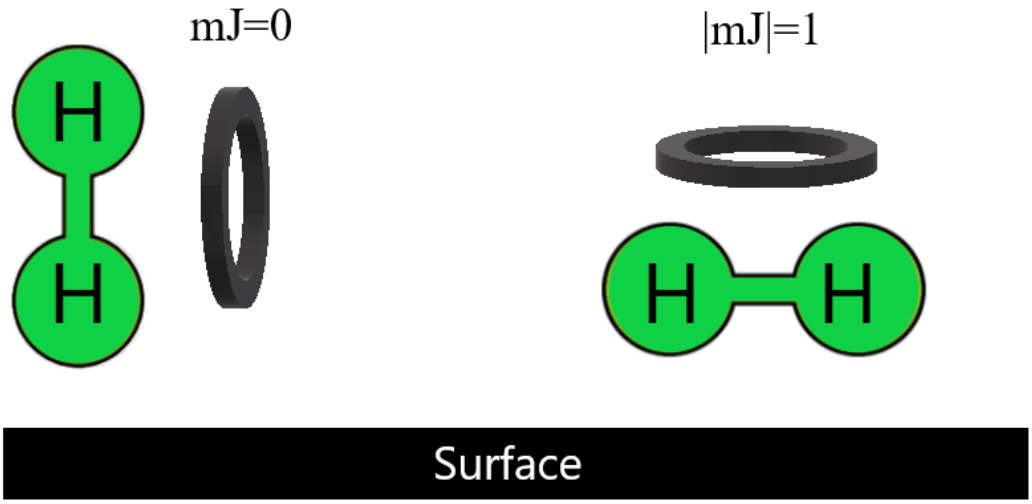

Figure 1.2: Rotational state projection of J=1 - with respect to the surface normal

cartwheel, a rotation around an axis parallel to the surface. Molecules with $m_J = \pm 1$ will rotate as clockwise helicopter or anti-clockwise helicopter, a rotation around an axis perpendicular to the surface.

1.2 Stereodynamic studies of molecule-surface interaction.

As we briefly mentioned above, the ability to control the quantum states of atoms and molecules is particularly beneficial if we want to study some interaction process in detail, and its dependence on the initial state. While it is quite common to control and measure electronic, vibrational and rotational states of a molecule, the rotation projection states of a molecule, which are nearly degenerate, are particularly difficult to control and measure. Both the orientation and the rotational orientation of a molecule can affect the outcome of a molecule-surface collision. The field studying these effects is often called stereodynamics.

There are two main approaches to control or observe rotational projection states which can be used (or used in combination). One is through specific photo-excitation schemes of molecules which alters the quantum state population distribution and the other is deflection of molecules within inhomogeneous fields (magnetic and electric), separating the quantum states in space. One severe restriction of these techniques is that they are typically applicable only to a rather small sub-set of systems (photo-excited states, polar molecules and/or paramagnetic molecules). A second restriction is that even when it is possible to prepare molecules with a particular rotation projection state, the coupling between the different internal degrees of freedom can lead to a rather quick mixing of these states [15], making it either difficult or impossible to incorporate these techniques in many molecule-surface scattering experiments. While these restriction have limited the amount of systems which could have been studied in the past, quite a few systems have been measured successfully and provided us with important insight into how the stereodynamics affects the probability for scattering, rotationally inelastic scattering, trapping and dissociation of molecules colliding with surfaces. Below are examples for a few of these studies, mentioning the techniques which were used and a very brief summary of the results of these studies.

Kurahashi et al.[16] measured the sticking probability of molecular oxygen on a Ni(111) surface and found that changing the orientation of the spin state with respect to the surface changed the sticking. The experimental method makes

use of the paramagnetic properties of O_2 to perform selective focusing of states. The same technique was also used to study rotational state dependence in the scattering of O_2 from highly oriented pyrolytic graphite and LiF(001) surfaces [17]. They discovered that the rotational alignment of the molecules is strongly related to the angular distribution of the scattered molecules, energy losses from the collision and the trapping probability. This group also combined a time-of-flight analysis with their state selection method in order to characterize the velocities and quantum states of paramagnetic atomic/molecular beams without scattering[18]. They used beams of ground state O_2 and metastable helium, and were able to measure the velocity distribution of the different quantum states.

Auerbach et al.[19] demonstrated that in the case of the dissociative adsorption of D_2 on a Cu(111) surface there is a preference for molecules with rotational orientation parallel to the surface rather than perpendicular, due to a lower activation barrier in broadside collision. The D_2 which was measured was formed by exposing one side of a thin Cu single crystal to D_2, the D atoms diffuse through the crystal to the other side where they meet on the surface and react to form a D_2 molecule which then desorbs from the Cu(111) surface. They used a resonance-enhanced multiphoton ionization (REMPI) scheme to ionize specific (ν, J) states of the desorbing molecules, then by changing the polarisation of the probe light to be either parallel or perpendicular to the surface normal, they were able to determine the degree of alignment of the desorbing D_2 as a function of velocity, using a time-of-flight (TOF) technique by measuring the scattered D_2 molecules as a function of the arrival time and internal state. Finally, using detailed balance arguments they related the rotational projection populations of the desorbing D_2 molecules on one side of the Cu crystal to the rotational projection dependency of the dissociative adsorption which created the D atoms on the other side of the crystal.

Yoder et al.[20] studied the stereodynamics of the chemisorption on Ni(100) of vibrationally excited methane. State selection was achieved using a linearly polarized infrared excitation, and the results showed an increase in methane reactivity when the laser polarisation is parallel to the surface, which was related to the alignment of the vibrationally excited rotational state of the incident molecules .

Bartels et al.[21] observed orientation dependence of NO molecules upon scattering with a Au(111) surface. They prepared the NO($\nu = 3$) excited state by means of a high-resolution infrared laser system and used a high voltage electrode to control the orientation of the molecule between N-end collision and O-end collision. They showed that the vibrational relaxation of the molecule is enhanced when the molecule approaches the surface with the N atom toward the surface by measuring the REMPI signal of the scattered molecules.

1.3 Thesis overview

Chapter 2 provides a detailed overview of the elements of the scientific instrument from Fig. 1.1 along with some of the theoretical background necessary for understanding how these elements function and combine together to form the complete experimental setup.

Chapter 3 describes a major development of the instrument which allows us to measure molecular beams travelling through magnetic hexapoles and a tuneable homogeneous magnetic field without scattering from a surface. The principles underlying the design are explained and both theoretical and experimental results are presented for beams of ^3He,^4He, D_2 and H_2.

In chapter 4, the magnetic molecular interferometer (MMI) is used to extract the scattering matrix from a molecular beam surface scattering experiment. A demonstration for the case of H_2/LiF(001) experiments is presented, along with a detailed explanation on the method.

Chapter 5 shows the work from scattering experiments of ^4He and H_2 from a graphene surface that was grown on a copper film. The results presented in this chapter show an example of a molecule-surface system which appears to not modify the quantum rotational state of hydrogen molecules during the collision.

The last chapter presents an overview and briefly discusses possible future work.

2

Basic elements and principles of the experimental and analysis methods

In this chapter the elements of the basic magnetic molecular interferometer setup will be described and the role they play in performing the magnetic manipulation experiments will be introduced. The basic principles underlying our modelling methods will be explained, and the magnetic field profile measurements, which are an essential ingredient for accurately modelling and analysing the results will be presented.

2.1 Introduction to the system

We now describe the different elements of the machine. Fig. 2.1 shows a 3-D model of the entire system. Starting from the source chamber (a in Fig. 2.1) we expand an atomic / molecular beam into the chamber through a small temperature controlled aperture (nozzle). During the supersonic expansion the beam cools down resulting in a reduction of both the kinetic energy spread and the population of higher rotational states (rotational cooling). The cooling process continues until a specific point away from the nozzle, where we skim the beam centre with a special shaped conical aperture called a skimmer, which allows only the central part of the beam to pass and continue through the machine. After

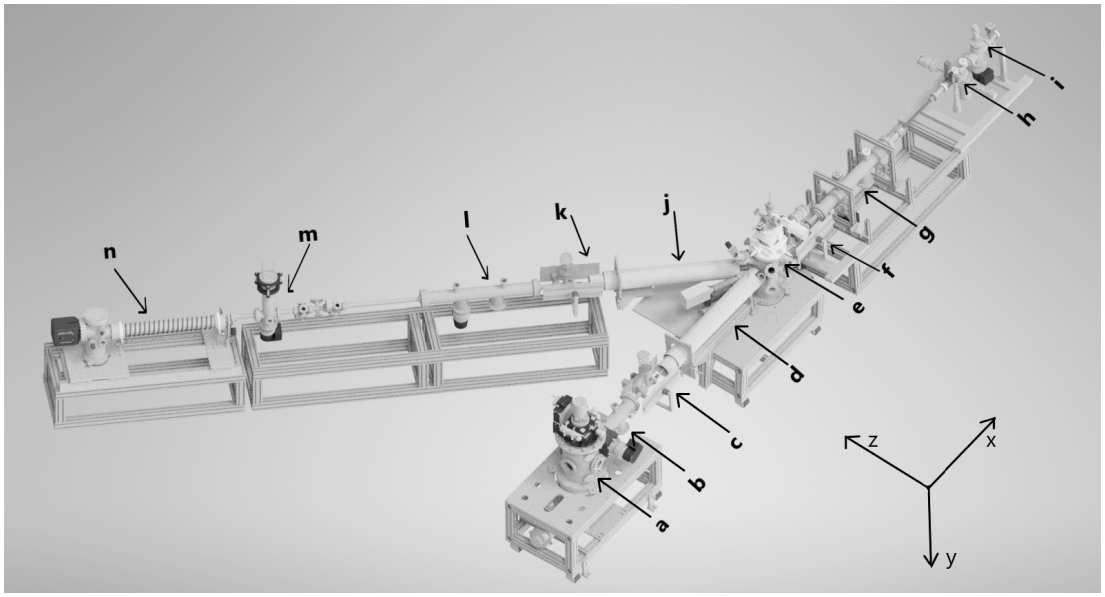

Figure 2.1: Dimensional drawing of the system - (a) source chamber, (b) magnetic lens, (c) dipole region, (d) first electromagnet, (e) scattering chamber, (f) dipole region, (g) magnetic lens, (h) 2-D profile stage (i) detection region, (j) second electromagnet, (k) dipole region, (l) magnetic lens, (m,n) detection regions.

exiting the skimmer and passing through two more apertures which are used for differential pumping (reducing the pressure), the beam enters the first magnetic lens (b in Fig. 2.1). The magnetic lens consists of a series of magnetic hexapole fields which deflect the trajectories of beam particles as a function of their magnetic moment (a detailed description can be found later in the text). The next element is the dipole field (c in Fig. 2.1), a combination of electromagnets and mu-metal plates are used to create dipolar magnetic field in the z direction, so that is the defined quantization axis of the particles. Exiting the dipole region, the beam travels through a zero magnetic field region into the first electromagnet (d in Fig. 2.1, referred to as B1 further in the text). The electromagnet produces a homogenous magnetic field in the direction of the beam axis, controllable by the current which passes through it. The beam then continues into the scattering chamber (e in Fig. 2.1). Here there are two modes, one for performing direct beam analysis experiments described in detail in chapter 3 and the other is for surface scattering experiments such as those presented in chapter 4 and 5.

For direct beam analysis, the sample is moved out of the beam path and the

beam continues directly out of the scattering chamber and into another dipole region (f in Fig. 2.1), this field defines the quantisation axis along which we will analyse the beam. The dipole field connects into a second magnetic lens (g in Fig. 2.1), which deflects the particle trajectories as function of their magnetic moments and acts as a state selector. The next element in the beam line after the second magnetic lens is the 2-D scanner stage (h in Fig. 2.1) which allows measuring a 2-D intensity profile of the beam. Finally, the beam enters a detection stage (i in Fig. 2.1) where we have a mass spectrometer to monitor the partial pressure increase in the chamber due to our beam particles. The above setup (elements a to i in Fig. 2.1) will be referred to later on in the text as direct beam setup and is used to profile the atomic / molecular beam, characterise the magnetic fields along the beam line and study our modelling of the propagation of the quantum states in our setup.

For surface scattering experiments we position a sample in the beam path and measure a fraction of the beam which scattered from the surface of the sample into a second arm of the machine (j to n in Fig. 2.1). The elements along the scattering arm of the machine are similar but not identical to those of the direct beam setup. The scattered beam exits the scattering chamber into a second electromagnet (j in Fig. 2.1, referred to as B2 further in the text). As with B1, B2 allows manipulation of the quantum states, however, in this case the manipulation is of the scattered particles. The beam then exits B2 into a zero magnetic field region and later into a dipole region (k in Fig. 2.1) which defines the quantisation axis which will be used to analyse the scattered beam. The dipole field connects into a magnetic lens (l in Fig. 2.1) which performs the state selection of the particles which continue towards the first detection region (m in Fig. 2.1, mass spectrometer). After the first detection region we assembled a second detection stage (n in Fig. 2.1) which is far more sensitive than the first but is restricted to measuring low mass particle beams. With this setup (elements a-e, j-n in Fig. 2.1) we can investigate various gas-surface systems by characterise the beam intensity while changing the magnetic field in the solenoids, before and after scattering. The v-shaped system is referred to in the text as the magnetic molecular interferometer (MMI).

2.2 Atomic / molecular beams

There are several reasons and motivations for using atomic or molecular beam techniques to study different phenomena that are hard if not impossible to study otherwise. In particular, after the supersonic expansion collisions between the beam particles become negligible, allowing us to obtain well defined particle properties (e.g. direction and velocity). Also, by introducing customised and controlled surroundings to the beam, such as magnetic field gradients or constant magnetic fields, the effect of those perturbations upon the beam can be measured and state selection can be performed.

2.2.1 Applications in surface studies

Atomic and molecular beams have been particularly useful in studying the interaction between the beam particles and crystal surfaces as well as the properties of the surfaces themselves. Examples include determining the structure of surfaces and adsorbate overlayers, measuring phonon dispersion, measuring surface diffusion and studying elastic, inelastic and reactive scattering of the beam particles [22, 23, 24, 25].

A key feature of the molecular beam technique is the ability to create a well-defined internal state population that is limited to a small number of energy states. This provides experimental benchmarks for studying the behaviour of matter[6, 24].

2.2.2 Creating a supersonic beam

The process of creating a supersonic beam involves an expansion of a gas through an aperture (nozzle). The gas is expanded from a reservoir at high pressure into a vacuum chamber, the ratio between the pressures in the reservoir and the vacuum chamber, will determine the behaviour of the beam in terms of its flow velocity and other state variables [26]. To describe our experiments, we start with a pressure of P_0 (reservoir) behind a nozzle of diameter d and let the gas expand into a chamber with base pressure of P_b (vacuum chamber). For a supersonic expansion, the beam velocity will grow as the flow area increases (further away

from the nozzle) up to a point called the Mach disk. The location of the Mach disk can be derived from the ratio P_0/P_b [26]

$$\frac{X_M}{d} = 0.67\sqrt{\frac{P_0}{P_b}}, \tag{2.1}$$

where d is the nozzle diameter and X_M is the location of the Mach disk on the expansion axis. Fig. 2.2 shows the location of the Mach disk as a function of the pressure ratio. The flow velocity increases as the flow area increases and

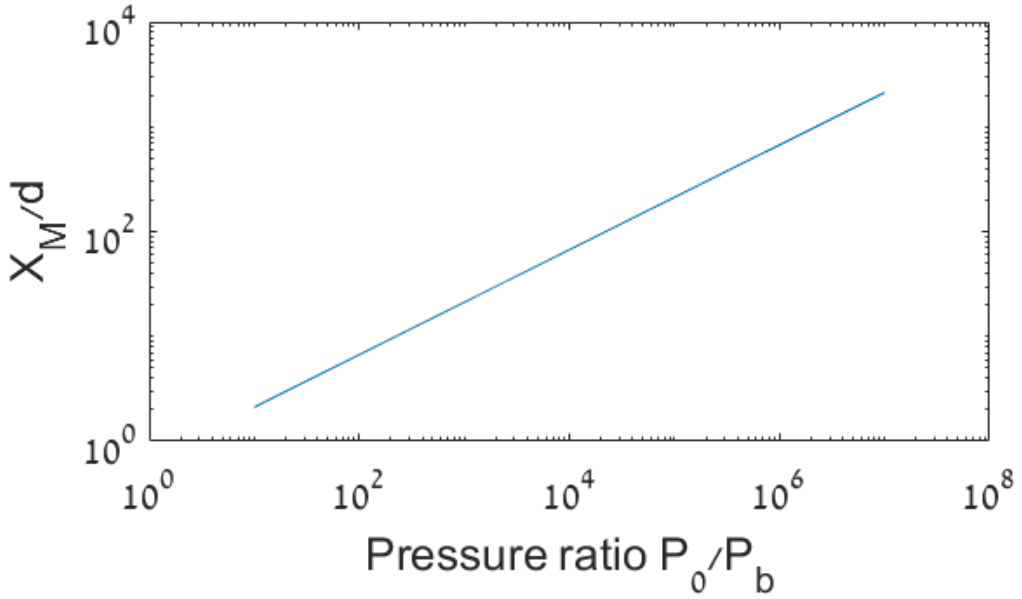

Figure 2.2: Location of the Mach disk - plot of Eq. 2.1

the beam adjusts to the low pressure in the chamber. This results in the beam travelling faster than the speed of sound, and because the boundary condition information is travelling at the speed of sound, the beam is essentially unaware of the boundary conditions. This ends with a shock wave (barrel shock, having its source at the Mach disk), a region with large density, temperature, pressure and velocity gradients. The shock wave provides the mechanism to reduce the flow speed to less than the speed of sound. The region of supersonic speed is referred to as the zone of silence and we use this region for the extraction of the centreline beam by introducing a skimmer in the beam path inside the supersonic region.

Fig. 2.3 shows a schematic of the expansion up to its jet boundaries.

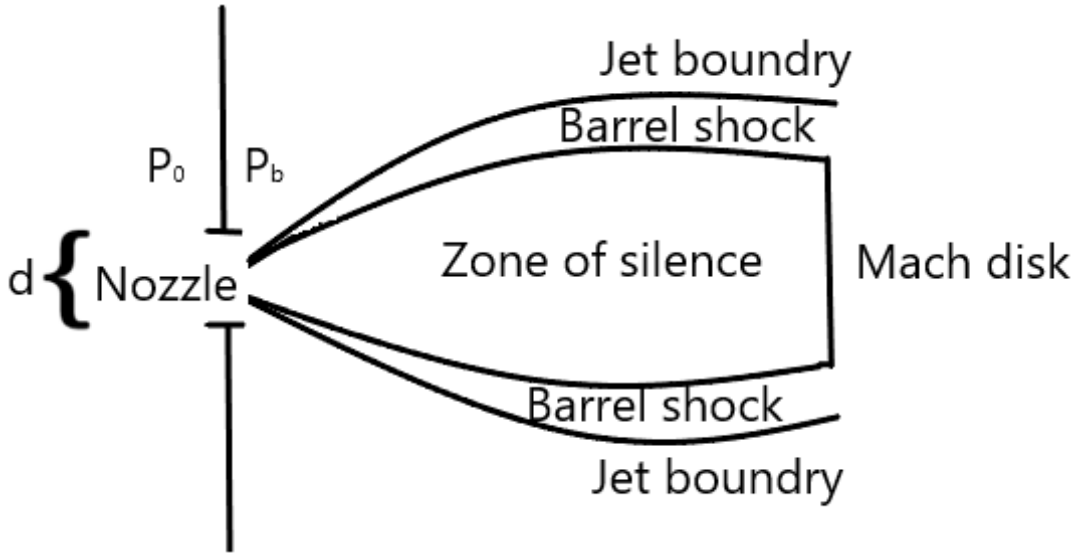

Figure 2.3: Beam expansion - schematic of the different expansion regions mentioned in the text.

The terminal velocity of the expansion is given by

$$v_\infty = \sqrt{(\frac{2k_B}{m}(\frac{\gamma}{\gamma-1})T)}, \tag{2.2}$$

where k_B is the Boltzmann constant, T is the nozzle temperature and γ is the heat capacity ratio which for monatomic beam -

$$\gamma = \frac{C_P}{C_V} = \frac{5/2k_B}{3/2k_B} = 5/3, \tag{2.3}$$

where C_P, C_V are the heat capacities at constant pressure and volume. The kinetic energy for a monoatomic beam can be written as

$$\frac{1}{2}mv_\infty^2 = \frac{5}{2}k_BT. \tag{2.4}$$

For an ideal supersonic expansion, the beam will move precisely at the terminal velocity (as the beam has no spread in temperature / energy therefore only a single velocity is expected), but in fact, for a realistic setup, there will al-

ways be a distribution of velocities around the terminal velocity. For the case of molecules like hydrogen which have a large spacing between the ground and excited rotational energy levels, the terms for the velocity and energy written above (for a monatomic beam) are still valid as long as our nozzle temperature remains cold enough and the beam is in its rotational ground states (J=0,J=1), leaving only energy exchange between translation degrees of freedom. From the skimmer onwards, our beam is an ensemble of particles with a distribution of velocities that can be determined from the analysis of experimental measurements. The conditions we typically use for hydrogen are a nozzle temperature of 100 K, $P_0 = 500\,\text{mbar}$, $P_b = 1 \times 10^{-4}\,\text{mbar}$, this results in a mean beam velocity of 1450 m/s and a velocity distribution with a full width at half maximum of about 5% of the mean velocity.

2.3 State selection

As first verified experientially from the Stern-Gerlach experiments[27], introducing a magnetic field gradient in the path of a spin 1/2 particle beam will spilt the trajectories of the two quantum states corresponding to the two possible spin projections, $m_I = \pm\frac{1}{2}$. This discovery led to the development of various types of experiments where the different states within a beam, that have a magnetic moment (either electronic spin, nuclear spin or rotational magnetic moment), are deflected [28].

2.3.1 Magnetic focusing

The beam which exits the skimmer, passes through two differential pumping stages and then passes through a magnetic lens which is created by a hexapole magnetic field[29]. To understand the function of the hexapole field, we will focus on molecular hydrogen, in its lowest energy rotating state, with nuclear and rotational numbers equal to 1 (I=1,J=1). For each projection state of I ($m_I = -1, 0, 1$) we have 3 rotational projection states leading to 9 states. The beam which enters the hexapole field consists of all possible state configurations – the 9 pure states, i.e. $(m_I = 1, m_J = 1)$, $(m_I = 1, m_J = 0)$, $(m_I = 1, m_J = -1)$, $(m_I =$

$0, m_J = 1)$, $(m_I = 0, m_J = 0)$, $(m_I = 0, m_J = -1)$, $(mI = -1, mJ = 1)$, $(m_I = -1, m_J = 0)$, $(m_I = -1, m_J = -1)$ and all the possible super position states. While the superposition states enter the hexapole, we can assume that they are dephased at the end of the hexapole and the beam can be treated as an ensemble of pure states, by pure state we mean a defined m_I, m_J state and not a superposition of different m_I, m_J states. This follows the calculations of Utz et al [30] who simulated the original Stern and Gerlach experiment and showed that the strong magnetic field gradients cause the Ag molecules to exit the field in a pure state regardless of how they entered the field (in any superposition of spin states). We assume that as long as the energy difference between the states and the field gradient of our magnetic lens is large enough, we can treat the hydrogen molecules exiting the hexapole as pure states. Within this picture, where the beam is an ensemble of all possible pure quantum states, we can now understand how the hexapole magnetic field works as a polariser. To do this we need to evaluate the different forces experienced by different quantum states, depending on their magnetic moment, the value of which is different for all 9 states.

We know that the force on a magnetic moment subjected to a magnetic potential is

$$\mathbf{F} = -\nabla U_p, \tag{2.5}$$

and our potential is

$$U_p = -\boldsymbol{\mu} \cdot \mathbf{B}, \tag{2.6}$$

where μ and $\mathbf{B}$ are the magnetic moment and magnetic field respectively. From Eq. 2.6 it is clear that the energy is higher when the spin is anti-aligned with the magnetic field. Inserting the potential into Eq. 2.5 will yield an expression for the force-

$$\mathbf{F} = -\nabla U_p = \mu \nabla |\mathbf{B}| = (m_J \mu_J + m_I \mu_I) \nabla |\mathbf{B}|, \tag{2.7}$$

where μ_J and μ_I are the rotational and nuclear magnetic moment. The equation for a hexapole field, in polar coordinates is

$$\mathbf{B}_{HEX} = 3C_3 r^2 (cos3\theta \hat{\mathbf{r}} - sin3\theta \hat{\boldsymbol{\theta}}). \tag{2.8}$$

Our magnetic field magnitude is $|\mathbf{B}_{HEX}| = 3C_3 r^2$ and the gradient is proportional

to the radial distance from the hexapole centre,

$$\nabla|\mathbf{B}_{HEX}| \propto r\hat{\mathbf{r}}. \tag{2.9}$$

Returning to the example of hydrogen, the magnetic moment is a combination of the nuclear magnetic moment (I) and the rotational magnetic moment (J) which is about 5 times smaller than the nuclear one [3], hence the nuclear magnetic moment will be the dominant contribution to the focusing of the molecules.

Molecules with a negative magnetic moment will experience a negative force (i.e. pulling them towards the centre of the beam axis), a positive force (away from the beam centre) acts on molecules with positive magnetic moment, while on molecules with approximately zero magnetic moment (even for m_I=0, m_J=0 it is not identically zero due to the spin-rotation coupling), the force is negligible in comparison with the other two and the trajectories of the molecules are not affected by the hexapole field (resulting in essentially straight trajectories).

As a result, the molecules with $m_I = -1$ (including $m_J = -1, 0, 1$) get focused while moving through the hexapole and molecules with $m_I = 1$ (including $m_J = -1, 0, 1$) get deflected out of the beam and eventually are extracted from the chamber by the vacuum pumps. Also molecules with m_I=0 will be slightly deflected or focussed depending on their rotational projection state ($m_J = -1, 0, 1$). The overall effect of the magnetic focusing stage, is to introduce a difference in the transmission probabilities throughout the machine of the different initial states, a difference which is later manipulated in the solenoid, B1.

An important element which is positioned between the magnetic lens and solenoid is a hexapole to dipole transition element. The role of this element is to adiabatically rotate the magnetic moments which are initially aligned with respect to the local field directions within the hexapole (which vary according to the hexapole field equation written above), towards a common direction defined by a dipolar magnetic field. This allows us to use a well defined quantisation axis to describe the rotational projection and spin states, before they enter B1 and are coherently manipulated. Fig. 2.4 illustrates a schematic of the scattering experiment with the different axis representation.

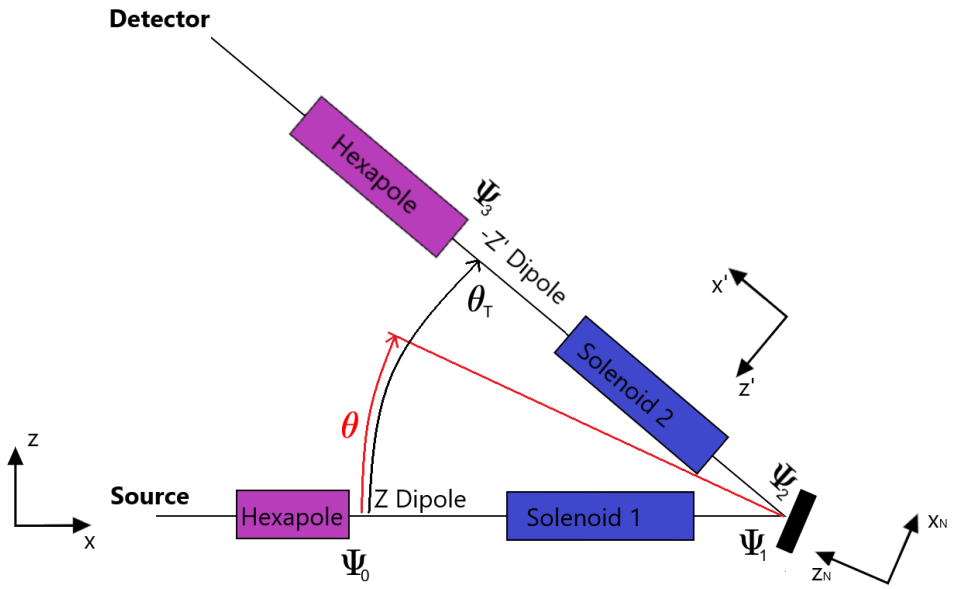

Figure 2.4: Schematic of surface scattering experiment - with marks to the different elements described in the text

2.4 Magnetic field coherent control

As the beam propagates through the magnetic field solenoid, the quantum state (nuclear and rotational) and its projection onto the different base states (the "population") can be altered as a function of the applied magnetic field strength and we can coherently control the wavefunction, i.e., alter the complex amplitude of the superposition quantum state (magnitude and phase). In order to understand the control over the different states, we will look at the relatively simple example of a beam of spin 1/2 particles.

2.4.1 Spin 1/2 in a magnetic field

The wave function of the beam particles changes as function of field and time of flight, and if we know the Hamiltonian we can coherently control the wavefunction. Our starting point will be particles exiting the magnetic hexapole with a pure wave function with respect to the $\hat{z}$ quantisation axis, i.e. their spin projection is either along the $+\hat{z}$ or the $-\hat{z}$ direction. Since the particles enter a solenoid field pointing in the $-\hat{x}$ direction it is convenient to re-express the wavefunctions in $\hat{x}$ frame, which can be done using a $\pi/2$ rotation around the $\hat{y}$ axis (For a full derivation see [31]).

$$|x_n\rangle = R^{\dagger}(\pi/2)\,|z_n\rangle\,, \tag{2.10}$$

where R is the rotation matrix, $|x_n\rangle$ and $|z_n\rangle$ are the eigenvectors of the Hamiltonian for magnetic fields along the $\hat{x}$ and $\hat{z}$ directions. The evolution of the particle in time obtained by solving the Schrödinger equation is simply

$$|\psi(t)\rangle = \sum_n A_n e^{-i\omega_n(B)t}\,|x_n\rangle. \tag{2.11}$$

Here A_n (n=1,2) are the expansion coefficients determined from the initial condition, $\hbar\omega_n(B) = E_n$ are the eigenenergies of the system in the presence of B field, $n = 1, 2$ for the case of spin 1/2 system. These two energies are

$$E_1 = -\frac{\hbar\gamma}{2}B\ ,\ E_2 = \frac{\hbar\gamma}{2}B \tag{2.12}$$

where γ is the gyromagnetic ratio. The expansion coefficients can be easily expressed by the initial state-

$$A_n = \langle z_n | R(\pi/2) | \psi(t=0) \rangle \,, \tag{2.13}$$

And the evolution of the initial state can be expressed as

$$|\psi(t)\rangle = R^{\dagger}(\pi/2) \left[\sum_n |z_n\rangle \, e^{-i\omega_n(B)t} \, \langle z_n| \right] R(\pi/2) \, |\psi(t=0)\rangle \,. \tag{2.14}$$

The probability for measuring a particle with respect to its initial and final state is

$$P_{fi} = |\, \langle z_{final}| \, R^{\dagger}(\pi/2) \left[\sum_n |z_n\rangle \, e^{-i\omega_n(B)t} \, \langle z_n| \right] R(\pi/2) \, |z_{initial}\rangle \,|^2. \tag{2.15}$$

Choosing a proper basis $|z_1\rangle = \left(\begin{smallmatrix}1\\0\end{smallmatrix}\right)$ $|z_2\rangle = \left(\begin{smallmatrix}0\\1\end{smallmatrix}\right)$ and the energies from Eq. 2.12, the state to state probabilities can be expressed as

$$P_{fi} = |\, \langle z_{final}| \begin{pmatrix} \cos\left(\frac{\gamma}{2}Bt\right) & i\sin\left(\frac{\gamma}{2}Bt\right) \\ i\sin\left(\frac{\gamma}{2}Bt\right) & \cos\left(\frac{\gamma}{2}Bt\right) \end{pmatrix} |z_{initial}\rangle \,|^2, \tag{2.16}$$

$$P_{11} = P_{22} = \cos^2\left(\frac{\gamma}{2}Bt\right), \tag{2.17}$$

$$P_{21} = P_{12} = \sin^2\left(\frac{\gamma}{2}Bt\right) \tag{2.18}$$

the above equations show the probability of finding a particle in a particular state.

2.4.2 Simulating the molecular beam signal

The initial molecular beam expansion is assumed to have an equal population in each of its rotational and nuclear quantum states. Trajectory calculations are performed in order to extract the transmission probabilities of each state through the first and second hexapoles. p_n denotes the probability for any of the beam initial states through the first hexapole and p_f, denotes the probability for any of the beam final states through the second hexapole.

The region between the two hexapoles is simulated using a mixed quantum and classical approach where the centre of mass is treated classically and the magnetic part of the Hamiltonian, containing the interactions of the nuclear spins and the rotational magnetic moments with the magnetic field and with each other, is treated quantum mechanically. This approach has been shown to lead to identical results to a fully quantum mechanical calculation as long as the magnetic fields are not extremely large [32]. Starting with the Hamiltonian

$$\hat{H}(B) = \frac{\hbar^2 k^2}{2m} + H_R(B), \tag{2.19}$$

where $\hbar k$ and m are the momentum and mass of the particle and $H_R(B)$ is the Hamiltonian by Ramsey[3]-

$$\frac{H_R(B)}{h} = -a\frac{\mathbf{I}\cdot\mathbf{B}}{B} - b\frac{\mathbf{J}\cdot\mathbf{B}}{B} - c\mathbf{I}\cdot\mathbf{J} + d\left(3\left(\mathbf{I}\cdot\mathbf{J}\right)^2 + \frac{3}{2}\mathbf{I}\cdot\mathbf{J} - \mathbf{I}^2\cdot\mathbf{J}^2\right). \tag{2.20}$$

The first two terms which depend on the external magnetic field ($\mathbf{B}$) are the Zeeman energies of the nuclear spin ($\mathbf{I}$) and rotational magnetic moment which is related to the angular momentum ($\mathbf{J}$). The third term represents the coupling interaction between the nuclear spin and the rotational magnetic moment, whereas the fourth term combines the spin-spin magnetic interaction of the two nuclei with the interaction of quadrupole moment. The parameters a, b, c and d, determine the strength of each contribution and were quantified by Ramsey et al. [3] for the case of H_2 and D_2. For the much simpler case of particles with only nuclear spin like ^3He, $b = c = d = 0$ and $a = \gamma B$ where γ is the particle gyromagnetic ratio. The propagation of the quantum states of the beam particles as function of their flight time is calculated in the first arm, using the z direction as the quantisation axis (see Fig. 2.4). The evolution of the initial wave function Ψ_0 to the wave function Ψ_1, which represents the wavefunction before scattering, is calculated by applying the Hamiltonian in Eq. 2.19 through the measured magnetic field profile. The coherent propagation starts from a position within the z dipole (marked as Ψ_0 in Fig. 2.4), where the field is sufficiently strong to keep the quantum states as pure states (there is no mixing between the 9 initial states). The propagation continues through a weaker section of the dipole into a

zero field region which leads to the first solenoid with its magnetic field pointing along the -x direction. After passing through the solenoid there is a second zero field region up to the surface of the sample, where we denote the wavefunction there as Ψ_1, which we represent in the z basis set. The complete propagation of the initial state through the magnetic field profile can be expressed as an operator $\hat{U}(B_1)$ and Ψ_1 can be written as

$$|\Psi_1(B_1, n)\rangle = \hat{U}(B_1)\,|\Psi_0\rangle = \hat{U}(B_1)\sqrt{p_n}\,|n\rangle\,. \tag{2.21}$$

Because m_I, m_J are not good quantum numbers for the Ramsey Hamiltonian (due to the field independent terms), our basis set $|n\rangle$ is a coherent superposition of the nine m_I, m_J states which we acquire by diagonalising the Ramsey Hamiltonian at every time step to get its eigenfunction. To get from Ψ_1 to Ψ_2 we need to introduce the scattering matrix which governs the scattering process. The quantisation axis of the scattering matrix is chosen to be aligned with the surface normal following an existing convention [33]. In order to use the scattering matrix with the surface normal quantisation axis, Ψ_1 has to be rotated so its quantisation axis is matched with z_N before applying the scattering matrix. After applying the scattering matrix, another rotation has to take place to change the quantisation axis from the surface normal to z', which is chosen to coincide with the dipole field of the spin analyser. The two rotations are around the y axis and the angles can be expressed as

$$\theta_1 = \frac{\pi}{2} - \theta\ ,\ \theta_2 = \frac{\pi}{2} - \theta_T + \theta, \tag{2.22}$$

where θ is the angle from the x axis to z_N and θ_T is the total scattering angle of the machine as illustrated in Fig. 2.4. Implementing the above to calculate Ψ_2 yields

$$|\Psi_2(B_1, n)\rangle = R(\theta_2)\hat{S}R(\theta_1)\overbrace{\hat{U}(B_1)\sqrt{p_n}\,|n\rangle}^{|\Psi_1(B_1,n)\rangle}\,. \tag{2.23}$$

The equation above tells us how to evolve an initial state through a magnetic field. First the state is assigned a probability weight, using results from trajectory bending simulations of the first hexapole lens. The quantum state is then evolved by the propagator $\hat{U}(B_1)$ and the quantisation axis is rotated with the

rotation matrix $R(\theta_1)$ so the scattering matrix can act on the state. After that the quantisation axis is rotated with the rotation matrix $R(\theta_2)$, the state is ready to be propagated through the second arm up to the entrance of the second hexapole and can be expressed as

$$|\Psi_3(B_2, B_1, n)\rangle = \hat{U}(B_2)\,|\Psi_2(B_1, n)\rangle\,, \tag{2.24}$$

with $\hat{U}(B_2)$ being the propagator through the second arm magnetic field profile composed out of a zero field region from the sample up to the second solenoid which creates a field along the -x' direction followed by a zero field and dipole field in the -z' direction until the magnetic field value is high enough to stop mixing of the different m_I, m_J states of the beam. Finally, we need to apply the probabilities of passing through the analyser hexapole into the detector with respect to the final state. The signal is given by

$$S = \sum_f \sum_n \langle \Psi_3(f, B_2, B_1, n) | \Psi_3(f, B_2, B_1, n) \rangle\,, \tag{2.25}$$

with

$$|\Psi_3(f, B_2, B_1, n)\rangle = \sqrt{p_f}\hat{U}(B_2)R(\theta_2)\hat{S}R(\theta_1)\hat{U}(B_1)\sqrt{p_n}\,|n\rangle\,, \tag{2.26}$$

where f,n denote the final and initial states and $\sqrt{p_f}$ is the probability of that final state passing the second magnetic lens and being detected.

In the explanation above, we have not considered the velocity spread of the beam, i.e. the fact that our beam is not monochromatic. In fact, the particles of the beam have a velocity distribution which is affected by the properties of the beam particles and the conditions of the supersonic expansion [34]. The dependence on the particle velocity is embedded in the propagator $\hat{U}$ because particles with different velocities will spend different times within the magnetic fields, which in turn will change the evolution of the quantum state. In order to get the detected signal we must calculate S in equation 2.25 for a reasonable range of velocities and sum the contributions to the signal using weights which correspond to the velocity distribution. The detected signal then can be expressed

as

$$DS = \sum_{v} p_v \sum_{f} \sum_{n} \langle \Psi_3(f, v, B_2, B_1, n) | \Psi_3(f, v, B_2, B_1, n) \rangle \,, \tag{2.27}$$

where v denotes the velocity and p_v the probability of that velocity to occur in the beam.

2.5 Magnetic field profile

Measuring the first and second arm profiles

As mentioned in the previous section, the exact magnetic field profile is necessary for the propagation of the wave function to be correct. The accuracy of the measurement should be on the order of 0.01 Gm in terms of magnetic field integral. The magnetic field along the first and second arms was measured in different sections for each arm of the interferometer, the first section being the strong part of the dipole region which was measured with a Gauss-meter capable of measuring a magnetic field up to 1000 G (Lakeshore instruments model 410) in an axial or perpendicular orientation. After mapping the strong part of the dipole field, the weaker parts of the dipole field were measured with a 3-axis probe Gauss-meter (Alphalab inc. VGM model), capable of measuring the magnetic field in 3 axis simultaneously up to 200 gauss. The same 3-axis probe was used to measure the rest of the first arm with no current in the solenoid to detect any residual magnetic fields within the magnetic shielding of the solenoid. Similar measurement were performed by myself inside the scattering chamber up to the position of the surface. The magnetic field inside the solenoid was measured again while passing a current of 0.75 A through the solenoid to assess the current dependent component of the magnetic field. By the end of this process we obtained a magnetic profile, along the axis and with spacing of points varying from 0.1 mm to 10 mm, composed of x and z components that are current independent and an x field that is current dependent (no y components were detected). The same process was repeated for the second arm, measuring both the current dependent and current independent parts of the magnetic field profile. Fig. 2.5 presents the measured magnetic fields in the first (panel (a)) and second (panel (b)) arms of the machine. The text in the figure relates the different elements of the apparatus to

the position coordinate. The red and blue curves shows the current independent magnetic fields in the z and x direction and the yellow curve show the current dependent magnetic field. Note that to plot all the different components on the same graph, different scales were used with the current independent Bx field multiplied by 5 and the current dependent Bx field and the Bz field attenuated by a factor of 5 and 10 respectively.

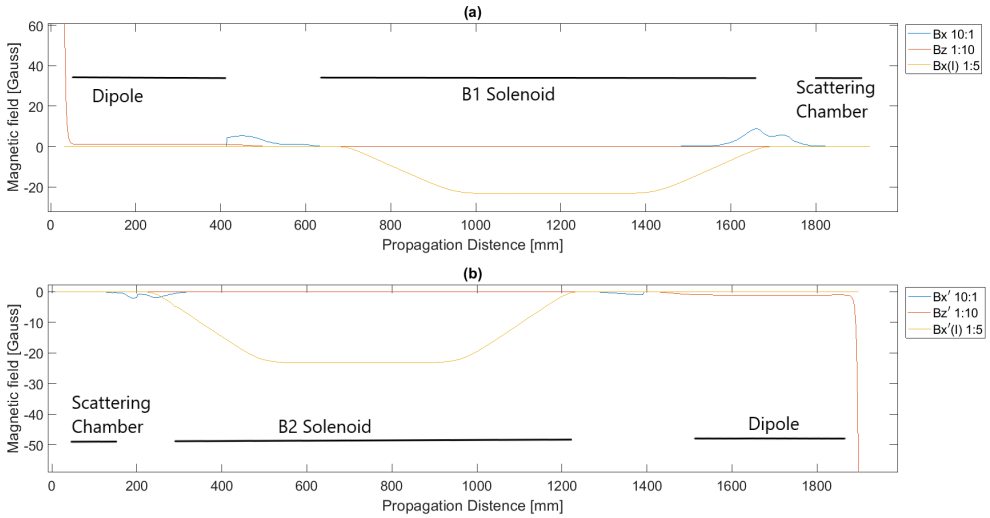

Figure 2.5: Measured magnetic field profile - along the first (a) and second (b) arms. For the weak and strong magnetic fields to be visible we scaled them differently as shown in the legend. The upper panel was measured from the strong dipole in the first arm up to the surface position and the lower panel was measured from the surface position up to the strong dipole in the second arm.

Detailed description of the measuring process

Dipole regions

To enable magnetic field measurements in this region, the vacuum components (marked as c,f and k in Fig. 2.1) had to be removed so that the magnetic probe could pass in the beam line. To measure the dipole region with enough spatial sensitivity, the magnetic probe of the gauss-meter (Lakeshore, model 410) was mounted on a mechanical holder, capable of moving the probe with a resolution of 10 micrometer. The magnetic field profile of the strong dipole (at the exit of the hexapole, see Fig. 2.6) was measured every millimetre so that the exact shape of the field's decay can be noticed. Far enough from the strong dipole,

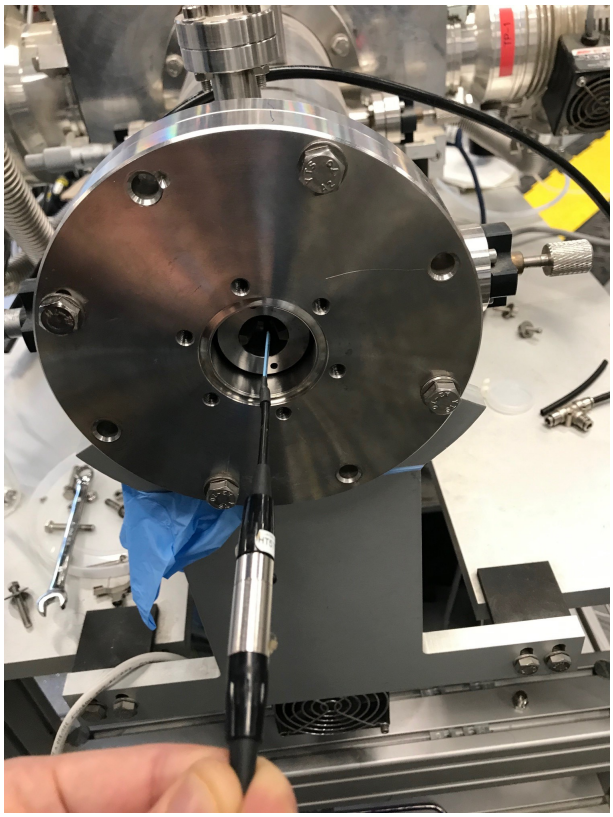

Figure 2.6: Hexapole chamber - with the magnetic probe used in measuring the strong dipole part. Note that this picture is for visualisation of the measurement region, and that during the measurements themselves the probe was held on a mechanical manipulator rather than by hand.

the magnetic field becomes relatively constant on the scale of centimetres. At

this point the magnetic probe was switched to the 3-axis gauss-meter (AlphaLab inc. VGM model) to allow smooth transition into the solenoid tube and measurement of much smaller magnetic fields. The measured field was solely in the z (first hexapole) and -z' (second hexapole) direction with the exception of a small axial field in the beginning of the magnetic shielding regions (mentioned below as well). Fig. 2.7 shows the measured profile in a semi-log plot.

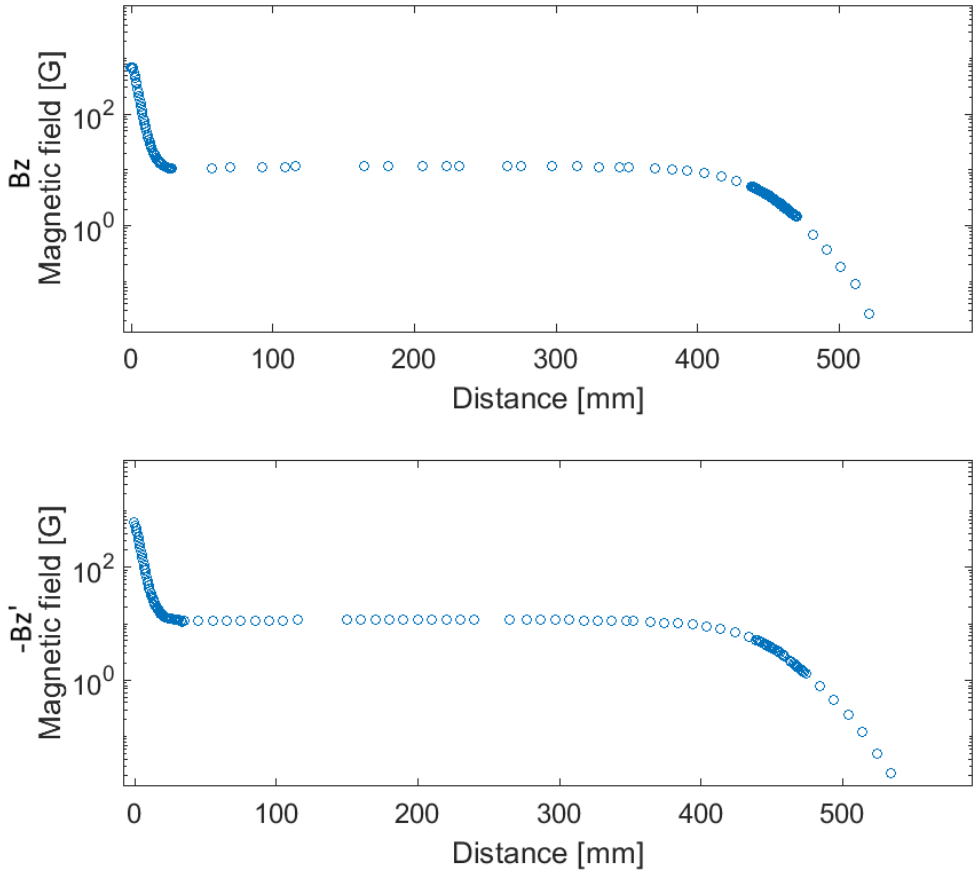

Figure 2.7: Dipole regions magnetic profiles - upper panel shows the first arm dipoles (Bz field) and the lower shows the second arm dipoles (-Bz' field).

Fields within the solenoid coils

The mapping of the solenoids was first performed without any current passing through them, meaning that with the magnetic shielding surrounding them no obvious magnetic field is expected. However, it was found that a residual magnetic

field integral is presence at both ends of the magnetic shielding regions creating non-negligible fields along the beam line directions (x and x'). The magnetic field was measured with the 3-axis gauss-meter, which was mounted on a custom probe mount (built by the Swansea university workshop). The mount allows us to insert the Gauss-meter along the vacuum tube of the solenoids while maintaining a fixed orientation of the gauss-meter. Fig. 2.8 shows the Gauss-meter probe with the mechanical mounting. Once the current independent field was mapped, the current in the coils was set to 0.75 A and the magnetic field profile was re-measured up to the gasket aperture that connects the scattering chamber with the incoming and scattered beam lines. Fig. 2.9 presents the mentioned

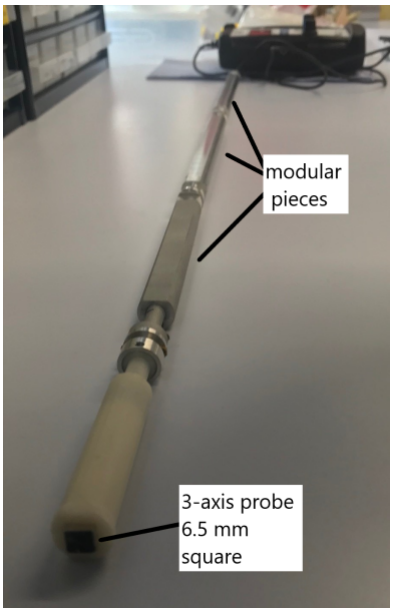

Figure 2.8: 3-axis gauss-meter - with the mount used for measuring

magnetic profiles within the two solenoids with and without applying a current.

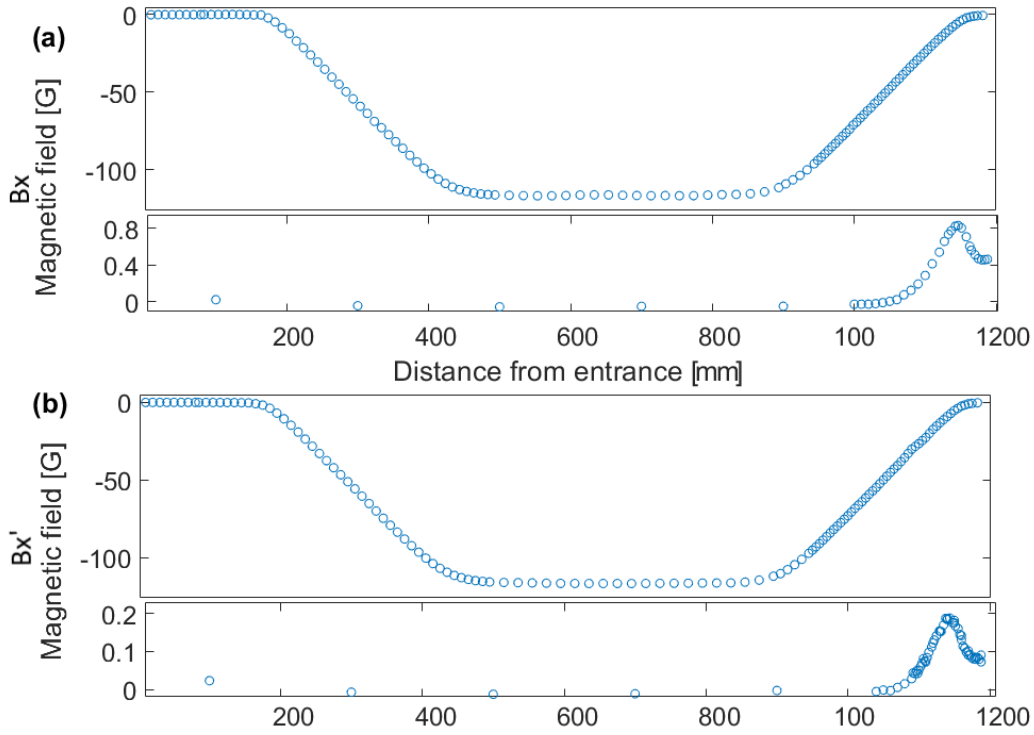

Figure 2.9: Solenoids magnetic field - The magnetic fields within the first (a) and second (b) solenoid coils. Each panel is further divided into two figures showing the current independent (lower figure) and current dependent (upper figure) magnetic fields. The horizontal axis shows the distance from the entrance of the solenoids vacuum tube (the entrance of the beam path in the first and the exit of the beam path in the second) up to the connection with the scattering chamber

Scattering chamber

First, we needed to examine whether the manipulator itself can be considered as a non-magnetic object. Due to mechanical constrains the only way to measure the field near the manipulator was to rotate the manipulator so that we can measure the field by inserting the probe from a different port in the scattering chamber. We measured the magnetic field by rotating the manipulator so that the gauss-meter probe approached the surface in a way which mimicked the way the beam would approach the surface from the first solenoid port and scatter from the surface into the second solenoid port. We used a PVC holder which included a flange connection to the port and a bored through cylinder. The magnetic probe was then fixed to the edge of a tube which was inserted into the bore of the PVC cylinder and could be driven along the centre of the port while

measuring the magnetic field up to the position of the sample surface (illustrated in Fig. 2.10) . These magnetic scans towards the sample surface, were performed

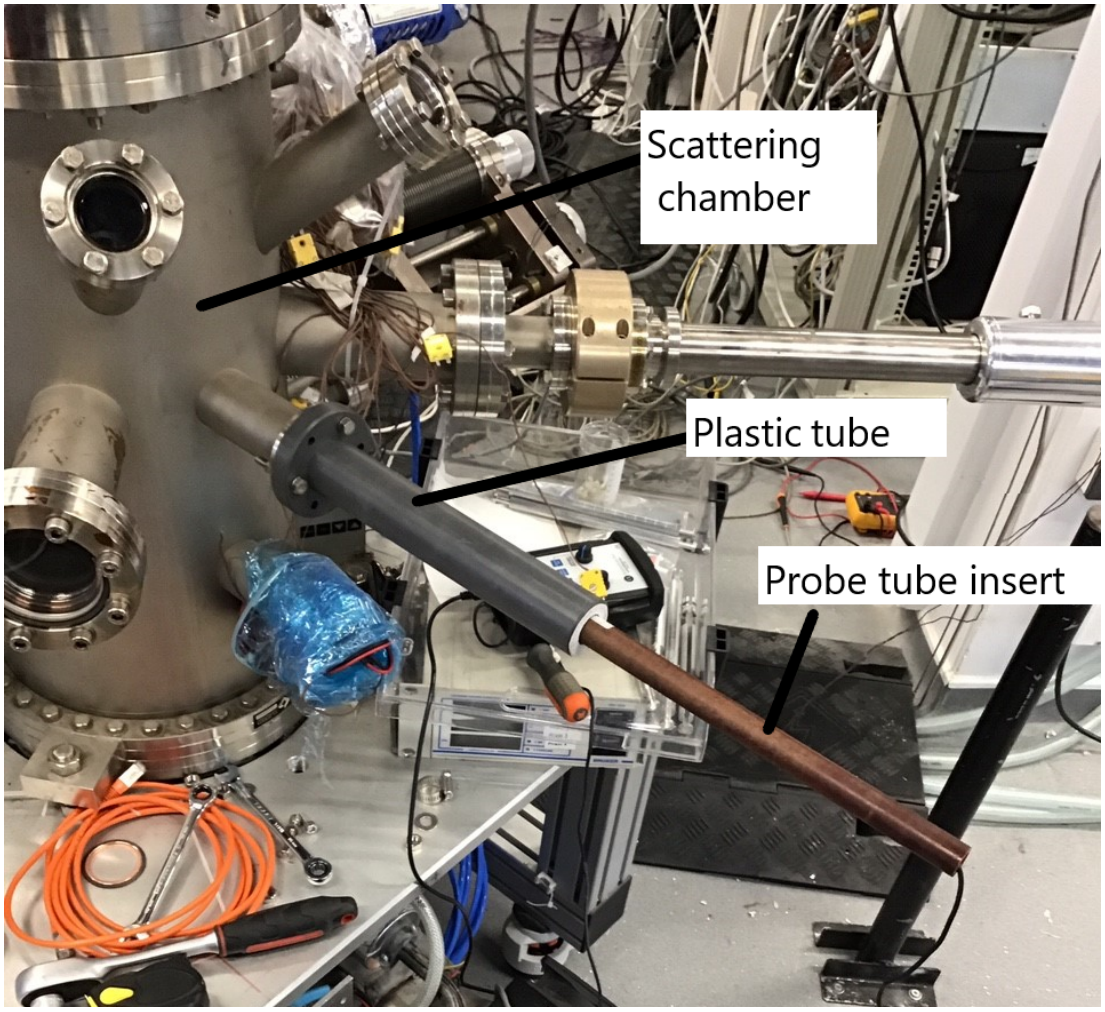

Figure 2.10: Equipment used in measuring the sample magnetic field - with markers to the different parts

at two angles corresponding to the angles through which the particles approach and fly away from the surface, before and after scattering. The measurements revealed a residual magnetic field that cannot be considered negligible (see red curves in Fig. 2.11). As the manipulator was built with non-magnetic materials, the explanation for the measured field was assumed to be the connectors for the K-type thermocouple used to measure the temperature and/or the in-vacuum motor used to control the azimuth angle of the surface. To tackle these aspects, I

replaced the K-type thermocouple with a non-magnetic T-type thermocouple and covered the in-vacuum motor with a mu-shield enclosure that should significantly reduce the magnetic field it creates. After the modification, the residual magnetic field disappeared, allowing us to consider the surroundings of the manipulator as a zero field region (see blue points in Fig. 2.11). The last step was to measure the magnetic field in the absence of the manipulator. The manipulator was taken out of the chamber and the magnetic field was measured from the solenoid gasket aperture up to the nominal surface position. Small residual fields along the beam line were discovered in the connection areas between the scattering chamber and the two solenoids. These fields had noticeable components only along the beam line directions (x and x' directions, see Fig. 2.12), and seem to be a continuation of the residual fields measured on the other side of the aperture gasket, i.e. from the solenoids towards the scattering chamber.

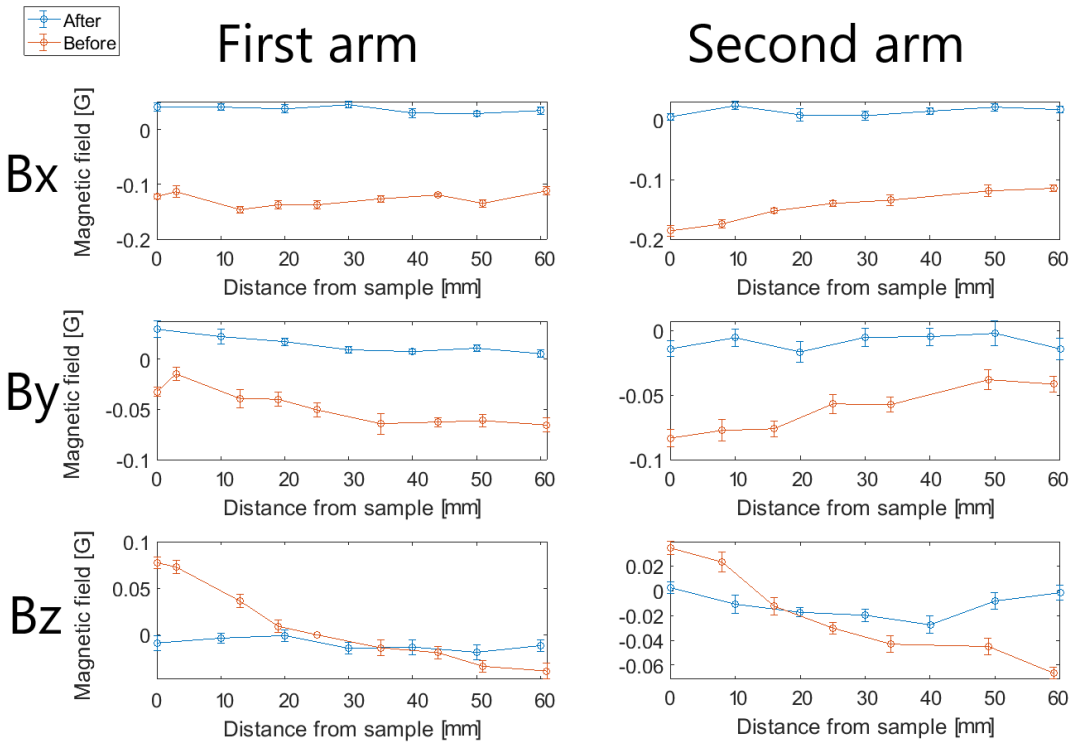

Figure 2.11: The magnetic field near the sample - 3-axis magnetic field profiles before (red) and after (blue) the changes made in the scattering chamber

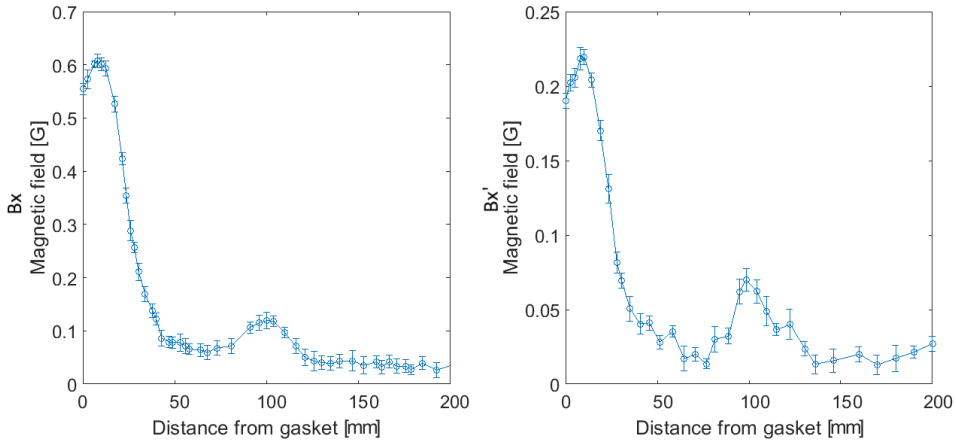

Figure 2.12: Magnetic field profile - the field inside the scattering chamber for the incoming beam (left) and outgoing beam (right). The sample is located at about 200 mm.

2.5.1 Measurement errors and restrictions of the sensors used.

Both Gauss-meters used to map the magnetic field profile have a nominal error of 2 percent of the reading. Another cause for a more systematic error is the actual position and size of the sensors. The probe used in the strong dipole (Lakeshore model 410) has a sensor with a relatively large sensitive area of 2 mm^2. The magnetic field behaviour in the region of the strong dipole part is very sensitive to the position of the sensor and a deviation of 1 mm from the centre axis results in noticeably different magnetic profile in magnitude and orientation. This means that using a probe which measures just one field direction leads to an unavoidable inaccuracy. The level of uncertainty that correspond to the orientation angle is proportional to $1-\cos(\theta)$ where θ is the angle of misalignment, this resulting from the magnetic flux being proportional to $\vec{B}\cdot\hat{n} = Bcos(\theta)$ where $\vec{B}$ is the magnetic field vector and $\hat{n}$ is the sensor surface normal. The nominal error in the sensor angle was estimated to be approximately 5 ° which translates to a deviation of 0.4 percent of the measured reading from the actual field value. The second sensor we used, has a 3-axis sensor (Alphalab inc.), which means all three components are measured simultaneously. However, this sensor is also limited in accuracy in regions where the field changes on a small length scale. All three sensors have

a sensitive are of 0.2mm x 0.2mm, which is relatively small, however they are displaced with respect to each other. The axial sensor is located 0.9 mm above the plane of the horizontal sensors and is shifted by 2.7 mm and 3.6 mm from the sides of the horizontal sensors. These small changes in sensor positions do not lead to significant errors as long as the magnetic field gradients are small enough to not change the field significantly on this scale.

2.6 Detection

In the detection area of the scattering machine there are 2 sets of detectors. The first is a commercial residual gas analysis (RGA , Extrel CMS) capable of measuring a wide range of masses (1-100 amu) with ionization efficiency crudely estimated to be between 1 to 10 counts for every million helium atoms passing through the detector. The second detector is an ultra-high efficiency particle detector (considered to be at least 100 times more efficient than the Extrel), capable of measuring small range of masses (2-4 amu) and is located at the end of the beam line. The detector ionizes the beam's particles using electron bombardment in a magnetic trap, followed by magnetic-sector separation of mass to charge ratio, and finally an electron multiplier that measures the current. The detector is an improved version of a previous magnetic trap detector [35] and was designed by the SMF group at the Cavendish Laboratory, University of Cambridge[36]. The second detector is an extension of the system and is there to allow more sensitivity at a price of less mass selection and long stabilization time while the first is stable and less sensitive.

2. BASIC ELEMENTS AND PRINCIPLES OF THE EXPERIMENTAL AND ANALYSIS METHODS

3

Direct beam analysis

3.1 Introduction

In this chapter I will describe a major modification to the setup which allows it to also investigate the beam without scattering. The modified setup (elements a-i in Fig. 2.1), which can perform quantum state analysis of both the scattered and unscattered beam (although not simultaneously), significantly enhances the type of information which can be resolved from surface scattering experiments. Having a straight through system allows us to study the magnetic field dependency of atomic/molecular beams that have never been investigated and extract the coefficients of the magnetic Hamiltonian for the gas molecules, or verify existing values for systems which have either been measured in a different way in the past or derived theoretically. Another important aspect of a direct beam analysis is the ability to characterize the parameters of the beam itself (energy distribution and rotational state populations) without any interference resulting from surface scattering. These values can then be used with confidence during the analysis of the scattered beam experiments, leaving the changes due to scattering as the only unknown quantities which we want to characterise. Finally, straight through experiments allow us to double check both our characterisation of the magnetic profile and the accuracy of our simulations and gain confidence in our understanding of the experiment itself.

3.2 Key-aspects in the design

To guide the design and check the performance of a direct beam experiment, we chose the case of a ground state molecular hydrogen beam. The dominant I=1, J=1 component of this beam gives rise to 9 different states (3 rotational states corresponding to $J = 1$ and 3 nuclear states corresponding to $I = 1$). Tracking the 9 states through the beam line is complicated enough and will imply that the system is capable of dealing with more than a simple two state system.

3.2.1 Sensitivity

An important criteria for assessing the ability to observe magnetic interference within the measured beam is the absolute difference between the flux of the different states that are being detected. As the beam has 9 different states in total, creating a sufficiently large difference between the probabilities of those states, ensures our ability to measure. The 9 different states mix into a superposition during the flight time of the beam in the solenoid until they reach the analyser magnetic lens. Having a population difference even between just 2 states after passing through the polarising hexapole field will force differences in the populations of all 9 states at the end of the beam and could be easily detected. When designing the direct beam setup, we can control the transition probabilities and consequently the population differences of the beam by choosing the position of the magnetic lenses, their length, where the detector position will be and the size of the apertures along the beam line.

3.2.2 Geometrical constrains

As the lab has a fixed size, there is a limit to the actual length that can be given to certain elements. The size of the lab restricts the total length of the direct arm extension and cannot be more than 3.5 meters, as that will need the lab walls to be removed.

3.2.3 Vacuum considerations

The pressures throughout the beam line (with the exception of within the molecular beam source itself) are low enough to be described as a molecular flow region, the probability of collisions between the particle of the beam is negligible, and the attenuation of the beam due to collision with other gas phase molecules is also negligible. The magnetic lens regions in the machine have a pressure of approximately 10^{-8} mbar. The reason for this is that the magnetic elements cannot be heated to high temperatures without altering their magnetic properties (at around 80 °C) and hence a bake-out of the vacuum system containing the magnetic lens is not allowed, resulting in limited vacuum levels within this region. In our design of the straight through arm, we must take this into account and make sure that the resulting pressure increase in the UHV chambers from those regions will not be larger than the UHV base pressure which is in the order of 10^{-11} mbar. To overcome this, differential pumping is used. The concept is well known in the vacuum community and detailed explanation can be found here [37]. The performance of the differential pumping scheme we apply can be understood by thinking of the differential pumping regions as a buffer between the high vacuum (HV) and ultra high vacuum (UHV) parts of the system. Each differential pumping stage has an aperture at the entrance and exit, to limit the gas throughput between the different parts and maintain the desirable vacuum level in the scattering and detector parts. A second consideration when choosing the aperture size is the influence of the apertures size on the beam. We must choose large enough apertures which do not limit the focused species in the beam, just the background gas flow. In practice the focused species in the molecular beam has a diameter of approximately 2.5 mm at the exit of the scattering chamber which can increase to approximately 4 mm further down the beam line. Fig. 3.1 illustrates a vacuum diagram of the different stages with the nominal pressure values and the chosen aperture diameters. The choice of the aperture diameters was made by considering the following argument, the gas throughput through the pump of the n^{th} stage, Q_n^{Pump} is defined by

$$Q_n^{Pump} = p_n \frac{dV_n}{dt} = p_n S_n, \tag{3.1}$$

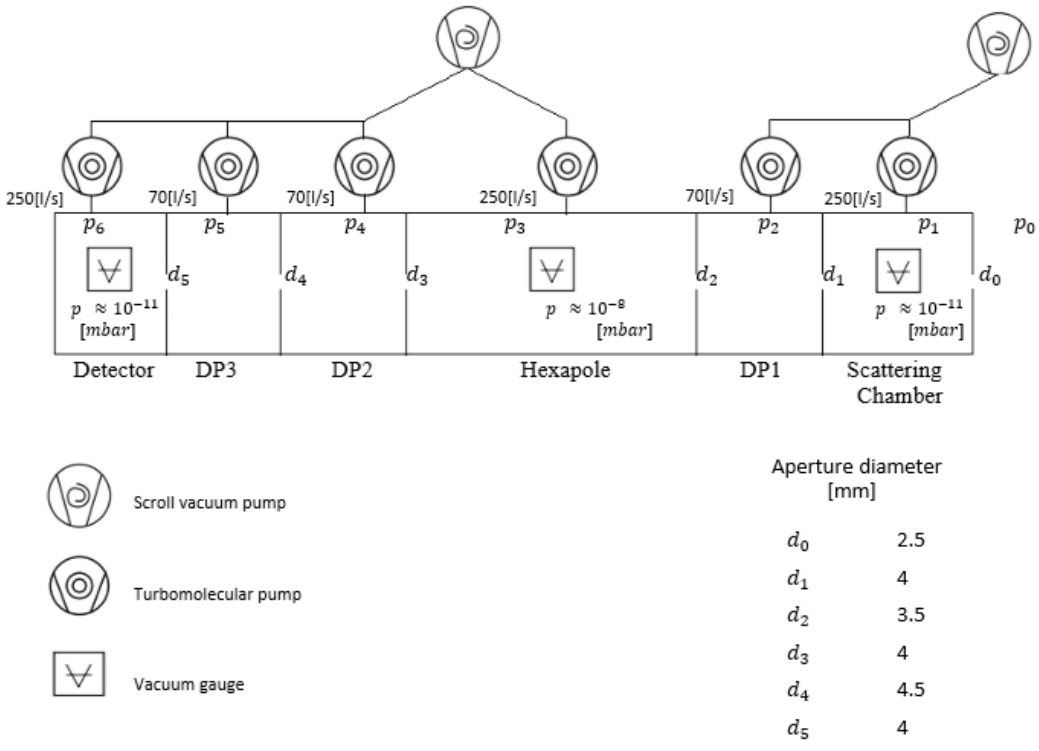

Figure 3.1: Vacuum schematics with apertures position and size - addition to the scattering machine

where p_n is the equilibrium pressure and $\frac{dV}{dt} = S$ is the time derivative of the volume known also as the pumping speed of the n'th element. The net gas throughput of an aperture separating the n'th and n+1 element is given by

$$Q_n^{Aperture} = (p_n - p_{n+1})C_{nn+1}. \tag{3.2}$$

Here C_{nn+1} is the conductance of the aperture between the n and $n+1$ stages. In equilibrium, mass conservation in each stage create a set of linear equation in p_n

$$(p_{n-1} - p_n)C_{n-1n} - (p_n - p_{n+1})C_{nn+1} - p_n S_n = 0. \tag{3.3}$$

Solving for the pressure in the scattering chamber

$$p_1 = \frac{p_0 C_0 + p_2 C_1}{C_0 + C_1 + S_1}, \tag{3.4}$$

where p_0, C_0 and p_2, C_1 are the pressure and aperture's conductance before and after the scattering chamber and S_1 its pumping speed. The conductance of an aperture can be approximated (for nitrogen) by the relation [37]

$$C_{aperture} = 12.1 d^2 \,\mathrm{l/s} \quad \text{d- diameter in cm} \tag{3.5}$$

Within the system configuration, an aperture diameter of 4 mm (marked as d_1 in Fig. 3.1) will restrict the pressure increase in the scattering chamber to about 2×10^{-11} mbar., assuming p_0, p_2 pressures of 1×10^{-8} mbar. Assuming we want a pressure of 10^{-11} mbar in the detector part and solving for p_5 yields

$$p_5 = \frac{p_6(C_5 + S_6)}{C_5}. \tag{3.6}$$

Using an aperture of 4 mm as d_5 and the parameters from Fig. 3.1, p_5 must be on the order of 10^{-9} mbar for the detector pressure to be as low as 10^{-11} mbar, a requirement that is easily fulfilled. The rest of the apertures sizes was chosen to maintain a pressure lower than 10^{-8} mbar in the chambers.

3.2.4 Trajectory simulation

3-D classical simulations of a H_2 molecular beam passing through the apparatus were used in order to establish the optimal configuration for the system extension. The different quantum states of the molecular beam experience a force while travelling inside the first and second hexapole's magnetic fields (elements b and g in Fig. 2.1), the force is proportional to the specific magnetic moment state of the molecule and the gradient of the magnetic field magnitude. The simulation method follows the basic principle used by Jardine et al for the case of helium-3 [29], in the sense that the trajectories are calculated classically whereas the magnetic moments are quantised with respect to the local field axis. Our simulations start with one magnetic μ_1 state (a specific m_I, m_J combination) and go through the following stages:

- We generate a beam from a source (disc), with a diameter of S_0. In the experiment this diameter could be either the size of the nozzle or that of a virtual source with dimensions between that of the nozzle and the skimmer. This depends on the details of the supersonic expansion and whether a secondary expansion takes place within the skimmer [38].

- For simplicity we assign a probability for each velocity, V, using a Gaussian velocity distribution $exp\left(\frac{4\log 2\left(\frac{V}{V_{mean}}-1\right)^2}{dV^2}\right)$ where V_{mean} is the mean velocity and dV is the full width at half maximum chosen to be consistent with the experimental value or considered as a simulation parameter.

- We generate the beam's particles by assigning polar and azimuthal angles from a random distribution and maintaining a uniform density within the beam diameter. Also, a maximal polar angle resulting from the bore size of the first hexapole will determine the maximal polar spread of the generated particles.

- We calculate the free flight of the molecules for each velocity up to the first hexapole.

- We propagate the beam through the hexapole by solving Newton second law (a detailed explanation on the force within the hexapole can be found in section 2.3.1).

$$\frac{d^2}{dt^2}\vec{x} = 3C_{hex1}\frac{\mu_1}{m}\nabla(\vec{x}^2),\ \vec{x}(t_0) = \vec{x_0}\ ,\ \frac{d}{dt}\vec{x}(t_0) = \vec{V_0} \tag{3.7}$$

  by means of the Runge–Kutta method [39], here $\vec{x} = (x, y)$ is the cross section position, ∇ is the gradient operator, $t = \frac{dz}{V}$ is the time spent in the magnetic field at velocity V in a single step of dz and C_{hex1} is the hexapole constant. $\vec{x}_0, \vec{V}_0$ are the initial position and velocity of the particle. The hexapole magnet assembly is composed out of multiple pieces with a gap of 5 mm in between which provides a larger pumping speed of the bore. In our simulations we assume that the force is zero and that there is no change in the magnetic state within these gaps. These assumptions should be valid because the magnetic fields gradients are much smaller in comparison to within the hexapole pieces (by more than order of magnitude), whereas the magnetic field itself is still strong enough to prevent spin rotation mixing.

- We calculate the free flight of the molecules from the exit of the first hexapole up to the entrance of the second hexapole.

- By the time the molecule reaches the second hexapole, due to the long distance between them and the variable field produced by the solenoid B1 (which is not included explicitly in the bending trajectory simulation), state mixing and changes in the magnetic moment of the molecule from μ_1 to μ_2 are expected. The probabilities of this mixing phenomena can be calculated for a given B1 value by means described in detail in section 2.4.2.

- We propagate the beam through the second hexapole using the same equation given above (Eq. 3.7) but using the specific geometry and magnetic properties of the analyser hexapole.

- We calculate the free flight path of the molecules up to the detection region

- We count the fraction of trajectories at the detection part which arrived without hitting any of the apertures along the way, this number is the probability of detection a μ_2 state which started as a μ_1 state.

Within the strong fields in the hexapole, the magnetic moment as a function of the state's projection is given by-

$$\mu_i(m_I, m_J) = m_I\mu_I + m_J\mu_J. \tag{3.8}$$

Here, $i = 1, 2$ denotes for first or second magnetic lens, m_I, m_J are the molecular states corresponding to the projection of the nuclear spin and the rotational magnetic moment, μ_I, μ_J are the corresponding magnetic moments. All the possible combinations of states results, for the case of H_2 in the $I = 1$, $J = 1$ state, in 81 different probabilities to calculate. The code used to generate the simulations was developed based on a previous version of the code used for water and methane molecules and propagation through a single hexapole lens [40]. Changes were made so that the code can track the movement of the particle's trajectories along the entire machine, including both hexapoles. The need to perform 81 different state configuration along the full distance of the hexapole lenses with statistical convergences is a time consuming computational problem, especially for the less focused states. Fortunately, these unfocused states which are hardest to calculate reliably, do not contribute significantly to the measured signal and therefore require reduced accuracy.

3.2.4.1 Results

The results below were generated assuming a beam of Hydrogen molecules exiting the 100 K nozzle (0.02 mm) at 1450 m/s and expanding into the skimmer (0.5 mm) with a velocity spread of 5% FWHM. In order to determine the position of the detection position, we need to take into account geometrical constraints of the beam line elements and the available space in the lab. This restricts the position of the detection position between 4.85 m to 5.15 m from the beam's source position. In the process of optimising the exact position, the difference between successful particle trajectories with initial / final states of $m_J = -1, m_I = -1$

and $m_J = 1, m_I = 0$ was chosen to be an appropriate optimization parameter. Although there are 9 different states, maximizing the difference between the populations of just two is sufficient enough, as these states will mix during their flight time between the magnetic lens according to the Hamiltonian, transferring the differences between populations to other states. Fig. 3.2 illustrates the difference in trajectories that pass a 0.4 mm aperture just before the detection region as a function of the aperture position from the beam's source. As can be seen in Fig.

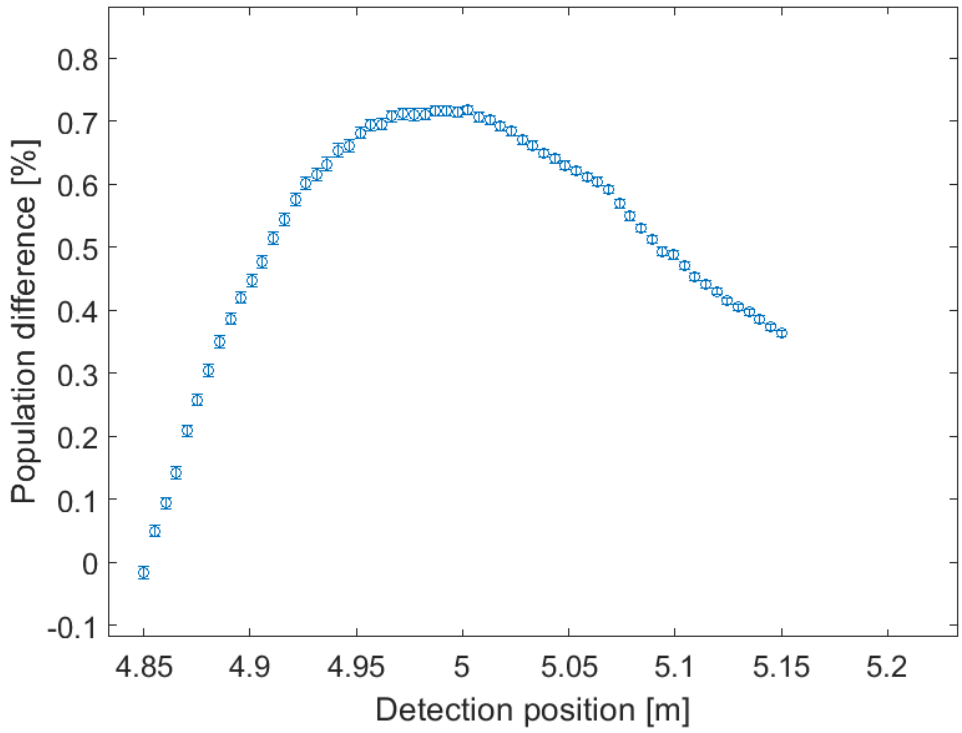

Figure 3.2: Population difference for determining detection position - difference in percentage between $m_J = -1, m_I = -1$ and $m_J = 1, m_I = 0$ trajectories, passing through a 0.4 mm square aperture. The error bars mark one standard deviation from the average value of each point.

3.2, the difference between the number of trajectories is characterised by a maximum approximately 5 m from the source, this result is representative for pairs of states where one of them is chosen from the triplet of focused states $m_I = -1$ and the other is from the triplet of either unfocussed or focused/defocussed states ($m_I = 0$). Correspondingly, $m_I = -1$ we chose to put the detection region within

that maximum region. Fig. 3.3 shows the behaviour of focused and slightly unfocused trajectories along the machine. As can be seen in Fig. 3.3, the focused

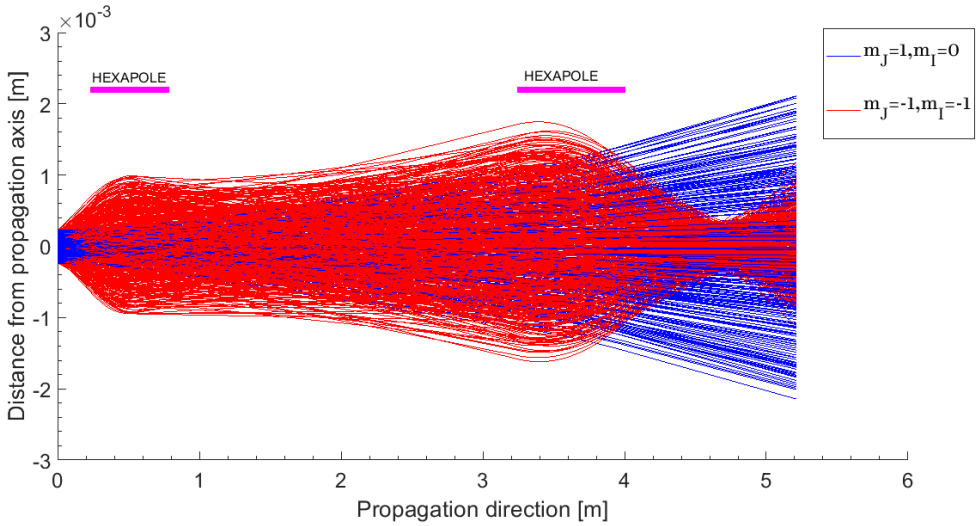

Figure 3.3: Focused and defocused trajectories - $m_J = -1, m_I = -1$ (red) are the focused trajectories and $m_J = 1, m_I = 0$ (blue) are slightly (only due to m_J) defocused trajectories, the hexapoles position and length are marked in magenta

state has a focal point just before 5 m whereas the slightly unfocused state is much more spread around the propagation axis. Fig. 3.4 shows a simulation of the expected molecular hydrogen beam 2-D intensity profile, 5 m from source position. The intensity profile was simulated to mimic an experiment where we scan the position of a 0.4 mm square aperture positioned before the detector. These type of simulations will be compared with experimental results later in this chapter.

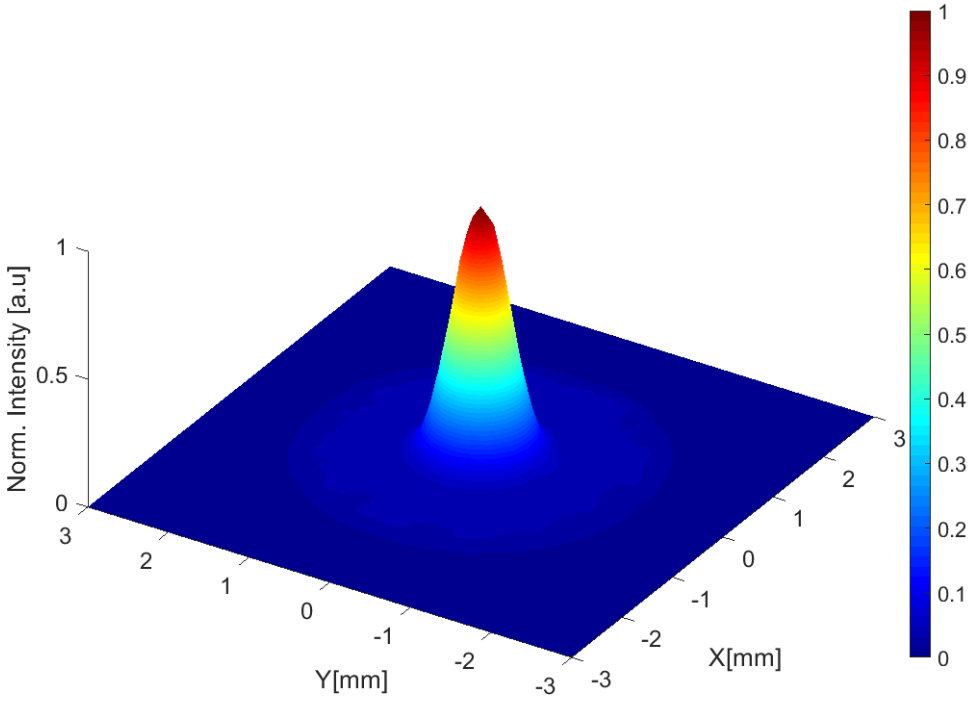

Figure 3.4: H_2 **simulated profile** - simulation of a 2-D profile scan with a square 0.4 mm aperture, the conditions of the simulation are given in the beginning of this section.

3.3 Assembly and measurements

After establishing the position of the detection region , the different elements of the extension were assembled. Fig. 3.5 shows a 3-D model sketch for the extension assembly with the different parts and axis labelled. The main elements of the extension are:

- Weak dipole field (holding field) assembly - Similarly to the dipole fields of a helium spin echo spectrometer [41], a combination of electromagnets and mu-metal plates are used to create dipolar magnetic field in the z direction. The particles enter into this region from the zero field (magnetically shielded) scattering chamber, and undergo a non-adiabatic transition. The term non-adiabatic transitions is used to describe transitions where the magnetic field changes abruptly (with respect to the local Larmor frequencies) and as a consequence of that, the populations of all the m_I and m_J mix.

- Strong dipole field - At the end of the dipole region the field is strengthened up to a value where (1) spin rotational mixing is negligible , i.e. the projection m_I and m_J along the z axis can be considered as constant and (2) the dipole field can be transformed into a hexapole field in an adiabatic transition, this means that the population of m_I and m_J with respect to the strong dipole field direction is maintained and converted into a similar population with respect to the local magnetic fields within the hexapole (which vary in direction for different azimuthal angles).

- Hexapole field (magnetic lens) - As described in more detail in section 2.3.1, within the hexapole field, the trajectories of the different quantum state of the particles bend, and are focused / defocused or unfocused (continue along a straight line) as function of their total magnetic moment. These leads to a significant population bias as function of distance from the centre of the beam, towards those states that are focused.

- Horizontal and vertical scanners - Used to profile the beam in the detection region. Each scanner allows us to position either vertical or horizontal

slits. Fixing one of the scanners at a specific slit size and position, while scanning the second one with the same slit size will produce a 1-D profile measurement integrated over the width of the specific slit size used. 2-D profiles can be measured by moving both scanners.

- Quadrupole Mass spectrometer (QMS) - The QMS (Hiden model HAL-201-RC) is used as a detector for the flux of the beam. The QMS is positioned at the end of the beam line (off the beam axis) and allows us to measure the partial pressure increase in the last chamber due to beam particles making it all the way through the extension.

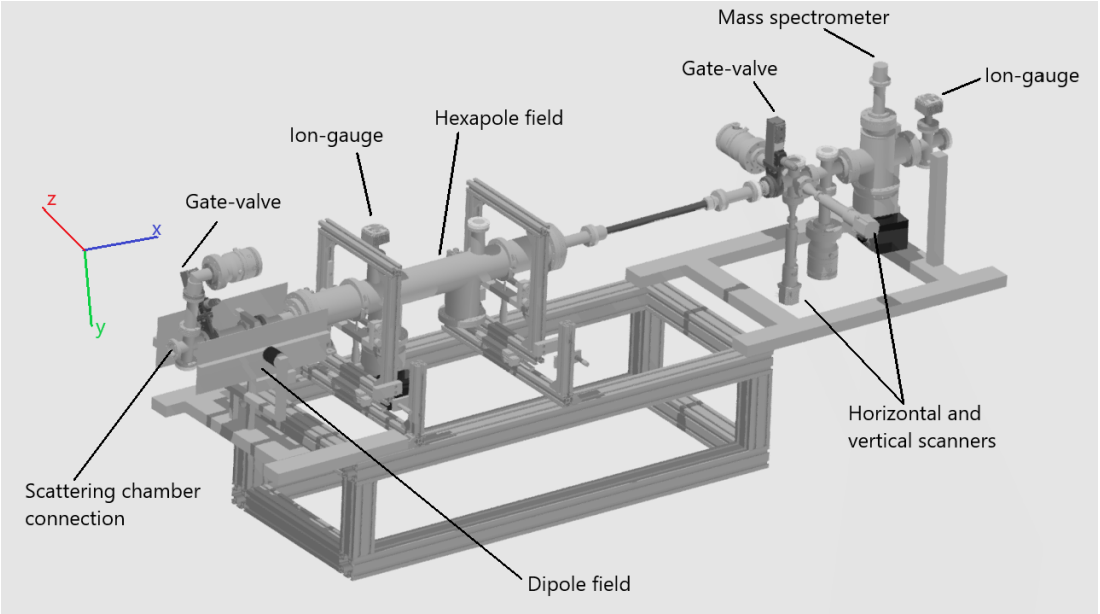

Figure 3.5: 3-D drawing of the direct extension - with pointers to the different elements and the used coordinate system

3.3.1 Dipole field (Holding field)

As can be seen in Fig. 3.5, the next element after the scattering chamber is the dipole field, creating a magnetic dipole field in the z direction. This element used to achieve two effects, the first is to minimize changes to the quantum state from stray magnetic field contributions, like earth's magnetic field and fields from

magnetic metal components of the apparatus. This is crucial as an undefined magnetic field would be impossible to predict and propagate through. A well-defined magnetic field profile is needed and achieved by the z direction dipole. The name holding field is used in the context of holding a predefined magnetic field in this region. The second effect is to define the quantization axis for the particles being measured, as upon entering the dipole field the objective is that their magnetic moment projection on the quantization axis will remain constant during the travel in this region.

To allow us to simulate the coherent propagation within this region (a concept which will be described in more detail further in this chapter), a measurement of the full magnetic profile was needed. Similarly to the profile measurements of the other two arms of the instrument, described in 2.5, we used two different gauss meters to measure the profile. A 3-axis gauss meter for the low field regions and 1-axis gauss meter, with smaller physical dimensions for the region of strong dipole field.

Due to the physical constraints of our measurement setup (the sensor holder), it was impossible to measure the full magnetic profile from the exit of the scattering chamber to the hexapole chamber in one continuous measurement. To tackle this the hexapole chamber was moved so a measurement of the magnetic field from the scattering chamber exit to a position 12.5 cm after the end of the dipole fields could be performed. Then the heaxpole chamber was moved back to its place near the dipole field and a second magnetic profile measurement was performed, focusing on the region leading into the strong dipole (replacing sensors when entering the strong dipole field). Fig. 3.6 shows the measured magnetic field profile starting from the exit of the first hexapole until the entry to the second hexapole. From our measurements we concluded that there are no significant magnetic fields in the y direction throughout the beam path, and only z and x components contribute to the magnetic field profile. Focusing on the extension for direct beam analysis described in this chapter, which corresponds to distances larger than 2000 mm in Fig. 3.6, a small but significant magnetic field in the x direction of up to approximately 2 G, appears at the exit port of the scattering chamber and decays when entering the weak dipole region. Simultaneously, the

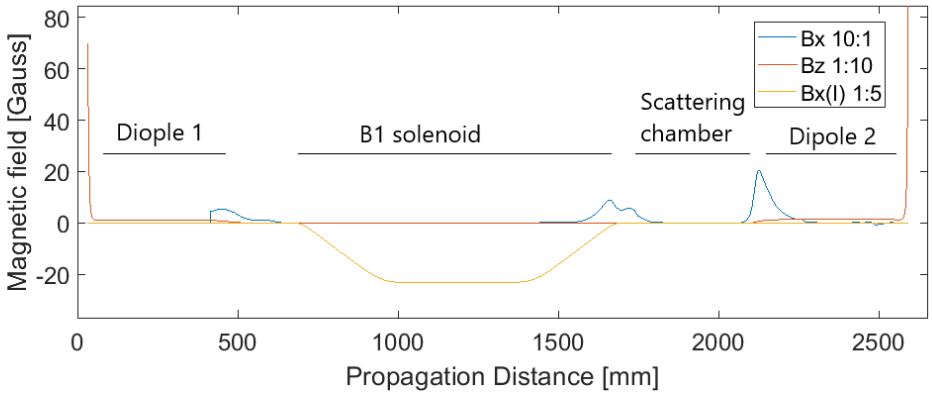

Figure 3.6: Magnetic profile for direct gas analysis - with markers to the different elements. For the weak and strong magnetic fields to be visible we gave them a different scaling, according to the legend.

magnetic field in the z direction increases up to about 14 G (when using a current of 5 A in the electromagnets which drive this field). This z field remains essentially constant for almost 30 cm before starting to decay slightly, at which point, the strong dipole field positioned at the entrance of the hexapole chamber starts dominating, and raises quickly to relatively strong magnetic field values ($> 10^2$ G) where m_I,m_J mixing is negligible, and consequently there is no need to calculate coherent propagation of the quantum state.

3.3.2 Magnetic lens

The next element after the holding field is the hexapole chamber. In this chamber we have a strong dipole field element followed by a dipole to hexapole element followed by a series of hexapole elements, all fields are created by permanent magnets. The purpose of the magnetic lens is to allow for certain states within the molecular beam to be focussed hence having more flux than other states in the detection region.

The hexapole field in the extension was built in the same manner as the analyzer hexapole used in the second scattering arm of the machine and following the optimised design of Dworski et al.[42]. The full hexapole consists of 14 pieces of 50 mm hexapole elements, separated by 5 mm gaps. Each element was built

from 12 permanent magnets, which were cut, magnetized along different directions and assembled within a mild steal yoke to generate the desired hexapole magnetic field within the bore of the element. The magnetic field at the tip of the permanent magnets is about 1.1 T. The field dimensions of each yoke are illustrated in Fig. 3.7 together with an illustration of the field behaviour of an ideal hexapole field. In total we assembled 14 yoke elements with the help of the mechanical workshop at Swansea University. The principle of the assembly was to first arrange the segment inside a pre-yoke element and then press them into the yoke (for detailed explanation see [43]).

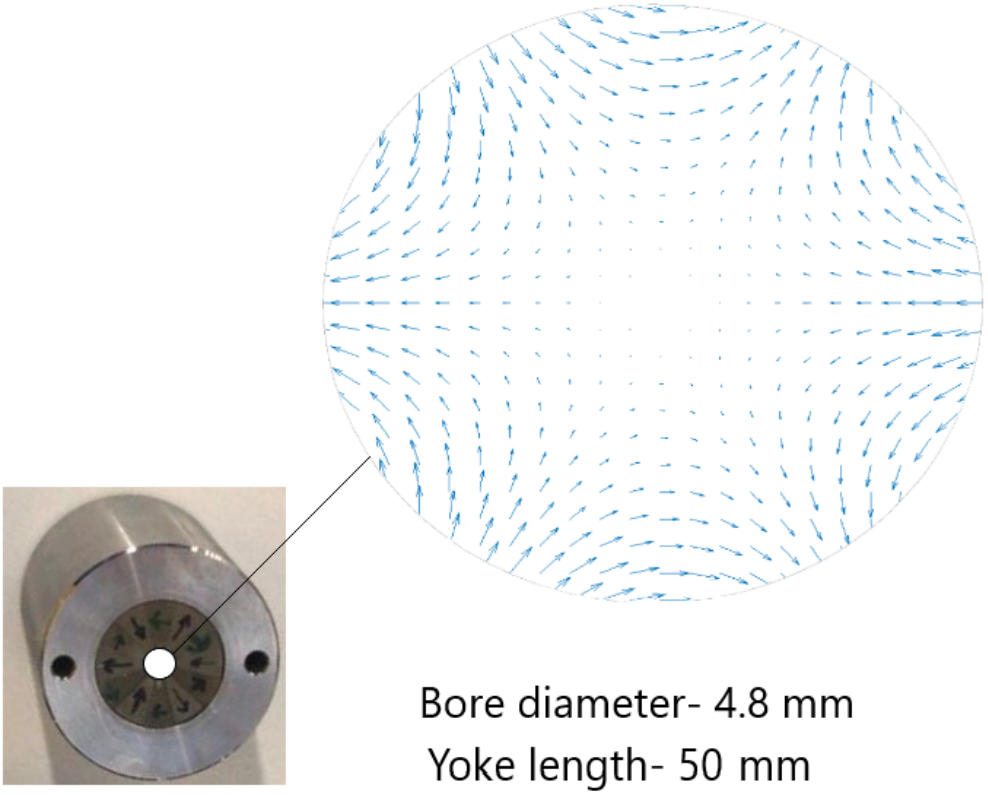

Figure 3.7: Picture of a single hexapole element - alongside the relevant dimensions and a visualisation of the field lines within an ideal hexapole field.

.

3.3.3 2-D scanners

The ability to physically scan an aperture within the beam cross section provides valuable insight into the spatial dependence of the beam flux, which in turn provides us with feedback for the action of the focusing elements. The scanners designed were made out of metallic rectangular piece attached to a linear motion feed-through with a motor. A 2-D profile with a square aperture of the beam flux intensity could be generated by scanning them along the relevant cross sectional area. A computer code was written in order to generate a profile scan. Having such profiles will allow for a comparison between the trajectories simulation and the measured profiles. By having the information resulting from the quantum state dependence in the trajectory simulation of the spatial dependence in the detection position we could choose either to perform magnetic manipulation measurement at different cross sectional positions and sizes or to focus on the most intense region in the profile.

3.3.4 Detector

The detector used in this setup is a mass spectrometer (HIDEN model HAL-201-RC) that measure the stagnation pressure of a chosen mass and allows a distinction between the residual background and the beam intensity. The major obstacle with detection of molecular hydrogen is its relative high background, due to its high natural abundance. In our measurements, the noise in the data will be limited to the shot noise, i.e. proportional to the square root of the background intensity. In some of the experiments we will perform with the direct beam setup, the expected pressure rise from the beam is on the order of 10^{-11} mbar. In a standard high-vacuum (HV) environment the partial pressure of a hydrogen molecule (mass 2) is on the order of 10^{-9} mbar. Taking into account random noise and unpredictable drifts in the background level, it will be difficult or impossible to make detailed measurements of the beam contribution to the intensity. For that reason, UHV conditions must be achieved in the detector chamber, this was obtained by baking the vacuum system to 120 °C for a couple of days, allowing the the total pressure within this section of the instrument to be lower than 5×10^{-11} mbar at room temperature. The mass spectrometer was connected to

the system computer and a script was written to initialise the parameters and to synchronize the pressure measurements to the magnetic solenoid of the machine.

3.3.5 Alignment

When assembling the extension beam line, a laser was used to align the apertures and the hexapole assembly. Initially, the laser beam was aligned using a 4 axis manipulator to go through the skimmer, all the apertures of the first arm and into the 2.5 mm aperture at the entrance to the scattering chamber. Then the rest of the extension elements were positioned to be centred with respect to this laser beam.

3.4 Results

The following section will present the results measured with the direct beam analysis setup. The experimental data, which is then compared with simulation results, is then used to verify that the focusing elements are working as we expect them to, identify and quantify a small residual field integral which was not picked up by the magnetic profile measurements and measure the velocity distribution in our beam.

3.4.1 ^4He beam

At first, we wanted to test the apparatus with a particle beam with no focusing properties so that the nominal shape of the beam reaching the detection part could be investigated. We used a ^4He beam emerging from a 100 K nozzle as this temperature resulted in a relatively high pressure rise in the detection region. Fig. 3.8 shows the 2-D profile measurement with a square aperture of 0.4 mm size. The 2-D profile resulted in the expected shape, in the sense that it is an almost uniform circular distribution. The circular distribution cut-off diameter is approximately 3.5 mm, which is little bit smaller than the aperture size before the scanner (4 mm d_3 in Fig. 3.1). This suggests that the beam passes through the machine with some minor interference, possibly from some small misalignment of

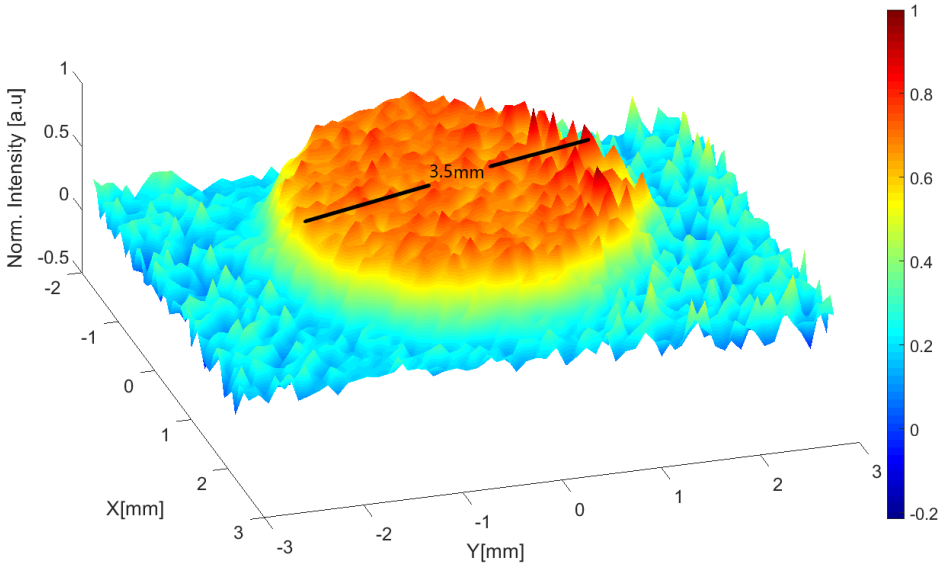

Figure 3.8: Intensity profile measurement of ^4He beam - measured with a 0.4 mm square aperture

the various apertures which cause the profile to be narrower than it should. As we will be mainly interested in focused molecular beam this should not limit us.

3.4.2 ^3He beam

In order to simulate magnetic scan measurements (measurements of the beam intensity as function of the magnetic field strength, B1) and profile scan experiments (measurements of the intensity as function of scanning aperture positions), we need to know both the magnetic field profile along the beam path and the transmission probabilities of the magnetic lenses. The magnetic field profile of the beam was measured as accurately as we could, however, there still remain uncertainties within regions where the field varies strongly as function of position (entrance to strong dipoles) making the results sensitive to small errors in the probe position, alignment of the probe and the finite sensor size. Furthermore, there are places that are impossible to measure with our probes, such as the field inside an aperture (as the probe can not pass through it) and within the hexapole magnets themselves.

Using a ^3He beam as a test beam provides valuable information. As the spin $\frac{1}{2}$ beam particle has only two different magnetic states (magnetic moments), the detected beam is composed of the focused state almost exclusively. This simplification makes the interpretation of profile measurements easier and also means that magnetic scan measurements are less sensitive to the transmission probabilities. This is different than the case of a hydrogen beam experiment, and makes it easier to assess the magnetic field profile within the rest of the beam line. Below we present experimental measurements of ^3He beams at 14 different nozzle temperatures varying from 20 K to 100 K (this is the actual span of temperature we could maintain without lost of stability). Two types of measurements were performed, 2-D beam profiles measured in a similar way to the ^4He profiles presented above and current measurement scans. The focusing capabilities of the magnetic lens are verified by comparing the measured and simulated 2-D beam profiles. We then extract the velocity distribution of the beam from current measurement scans and then use these empirical distributions to analyse the magnetic scan measurements. Using a set of data we identify a small but non-negligible missing residual field integral along the direct beam setup and using a complementary scattering measurement from Cu(111) we identify the residual field value needed when simulating the scattering setup.

3.4.2.1 Focusing

To get a grasp on the actual focusing power of the ^3He beam we measured a 2-D intensity profile, like we did with the ^4He beam. We measured the intensity of the beam passing through a 0.4 mm square which was scanned to create a 2-D profile. Fig 3.9 shows a scan of a 50 K nozzle temperature beam, this corresponds to a mean beam velocity of about 800 m/s. The two panels in Fig. 3.9 show the measurement results using two viewing angles, while the shape of the high intensity spot is not completely circular, we approximate the size of the ring of the half maximum as having a diameter of about 0.5 mm, in striking contrast to the ^4He unfocused beam. Fig. 3.10 shows a simulation of the intensity profile, trying to mimic the measured signal. The simulation parameters was of a ^3He beam travelling with a 800 m/s central velocity and a Gaussian velocity distribution

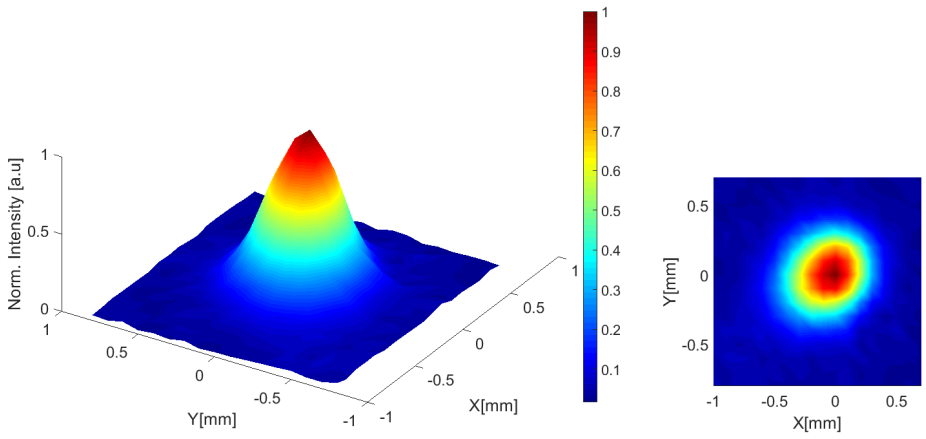

Figure 3.9: Intensity profile measurement of ^3He beam - measured with a 0.4 mm square aperture. The small asymmetry seen is the simulated data is due to restricted number of trajectories leading to incomplete convergence.

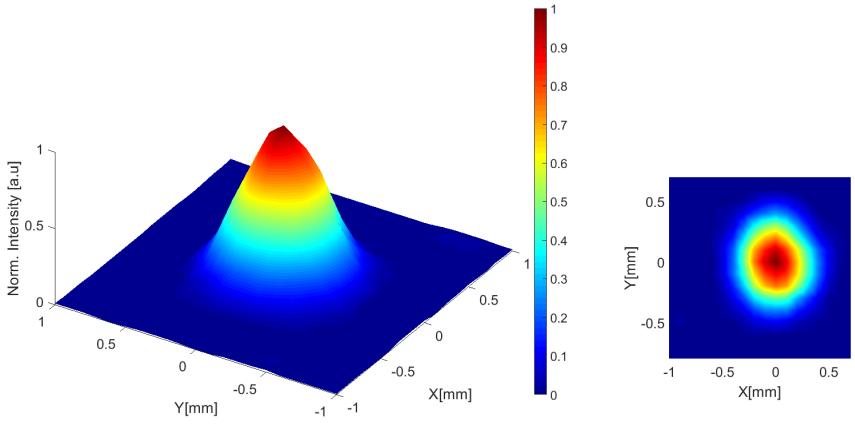

Figure 3.10: Intensity profile simulation of ^3He beam - simulated with a 0.4 mm square aperture and mean velocity of 800 m/s with a 10 % FWHM spread

with 10 % FWHM through the machine up to the detection position. The reason for the asymmetry in the simulated profile comes from lack of convergence, as in practice, each run in the simulation yields a small number of particles which were able to pass through the entire system. As we can see from the simulation, the expected shape in the top view (small figure) is of more circular shape than the measured signal which shows a stronger distortion, however the nominal sizes of the different intensity rings are quite comparable (FWHM of the measurement is 0.52±0.03 mm and the simulation FWHM is 0.55 mm) between the measurements and the simulations. One reason for the shape inconsistency could be that the polariser hexapole lens is not perfectly aligned while the simulation is treating the beam geometry as aligned with respect to the magnetic lens and the different apertures. Fig. 3.11 illustrates the resemblance and also shows that the actual

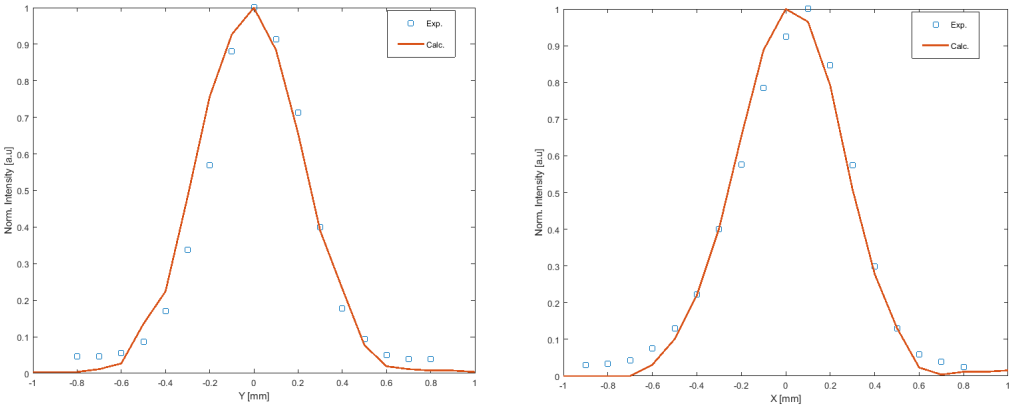

Figure 3.11: Horizontal and vertical comparison - comparison of the measured and calculated profile

shape of the beam is a bit deformed with respect to the calculation.

3.4.2.2 Velocity distribution

In order to perform realistic calculations and meaningful comparisons with the experiments we need to estimate the velocity distribution of the beam. For the case of a ^3He this can be performed relatively simply as we show below. We start with some preliminary definitions, following the approach presented in [44].
It is convenient to focus on the De Broglie wavelength, instead of the particle velocity,

$$\lambda = \frac{h}{mV}, \tag{3.9}$$

where m h V λ are the mass, Plank constant , particle's velocity and wavelength. Our scanning parameter is the current in the solenoid, we define a variable, κ which is proportional to the current vector and given by

$$\kappa = \frac{\gamma m B_{eff} I}{2\pi h}, \tag{3.10}$$

here γ is the gyromagnetic ratio and B_{eff} is the field integral of the solenoid per unit current.
The signal at the detector can be expressed as

$$P(\kappa) = \int_{\lambda_{min}}^{\lambda_{max}} \rho(\lambda) e^{2\pi i \kappa \lambda} d\lambda. \tag{3.11}$$

To extract the wavelength distribution, a discrete Fourier transform needs to be done on $P(\kappa)$-

$$\rho(\lambda) = FT\left[P(\kappa)\right]. \tag{3.12}$$

Applying the relation in Eq. 3.9 will results in

$$\rho(\lambda) = \rho\left(\frac{h}{m\lambda}\right)\left|\frac{d}{d\lambda}\left(\frac{h}{m\lambda}\right)\right|, \tag{3.13}$$

And the velocity distribution is given by,

$$\rho(V) = \rho\left(\frac{h}{m\lambda}\right) = \rho(\lambda)\left|\frac{d}{d\lambda}\left(\frac{h}{m\lambda}\right)\right|^{-1}. \tag{3.14}$$

Fig. 3.12 shows in the first panel (a) the detector signal as a function of the

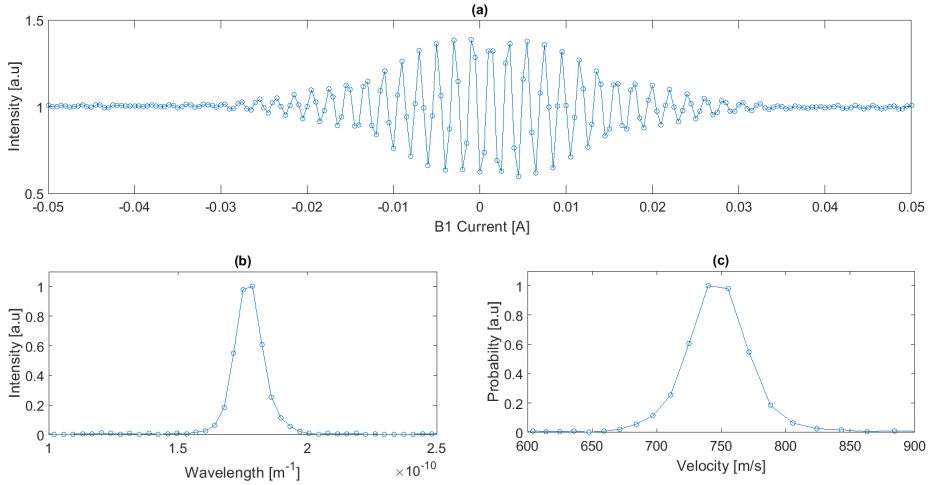

Figure 3.12: ^3He **measurement analysis** - (a) ^3He magnetic scan measurement measured using a nozzle temperature of 40K, normalised with respect to the mean value, (b) Reconstructed wavelength distribution and (c) Reconstructed velocity distribution

current in the first solenoid. In the second panel (b) we get the wavelength distribution by Fourier transforming the signal and plotting the magnitude. The third panel (c) illustrates the velocity distribution, transformed from the wavelength distribution by means of Eq. 3.14 and yield $v/\Delta v = 7.5$, where v is the peak velocity and Δv marks the half width at half maximum of the peak.

3.4.2.3 The magnetic field profile

Further information, that can be gathered using the direct analysis beam line, is the effective magnetic field integral the beam particles pass through. To study this, we performed magnetic scan measurements on a ^3He beam at different nozzle temperatures. As mentioned in section 2.4.1, the measured signal in the case of a spin half particle detector can be expressed as-

$$DS(I, v) = \sum_v P_v \cdot |\cos(\Phi)| \, , \Phi = 2\pi\gamma[B_{eff} I + B_r] \cdot \frac{1}{v} + \phi \tag{3.15}$$

Where v marks the velocity of the particle, P_v, the statistical weight of the velocity extracted from the Fourier transform of the measurents as explained above, γ is the ^3He gyromagnetic ratio, B_{eff} is the magnetic field integral per unit current in the solenoid, B_r is a residual field (current independent) which is assumed to be directed along the beam axis (in the coherent region of the propagation) and ϕ is an angle, which in the above expression represent a possible difference between the quantization axis of the first and second magnetic lens region. For the discussion below we will assume that ϕ is negligible, as small values which are consistent with assembly misalignment (1-2 °) would lead to changes which are too small for us to observe. For each nozzle temperature measurement, the velocity distribution is extracted, then the signal is simulated by propagating the beam through the experimental profile with the spin half Hamiltonian and imposing the extracted velocity distribution on the calculation, resulting in a set of 14 calculated signals which can be compared with their corresponding experimental signals. In order to extract B_r we simultaneously analyse all of the measurements in the following manner,

1. Fourier transform both the measured signal and the calculated signal
2. Transfer the scale into velocity
3. Extract a phase difference from $\Delta\Phi(v) = \tan^{-1}\left(\frac{Im[FT(s_m)]}{Re[FT(s_m)]}\right) - \tan^{-1}\left(\frac{Im[FT(s_c)]}{Re[FT(s_c)]}\right)$ here $_m$ stand for the measured signal and $_c$ for calculated signal
4. Repeat for all measurements and calculations

By plotting $\Delta\Phi$ vs. $\frac{1}{v}$ we can check for the linear behaviour expected from an additional residual field integral. By fitting the result to $\Delta\Phi{=}2\pi\gamma B_r \cdot \frac{1}{v}$ we can extract the residual field integral which will minimise the difference between our calculations and measurements. Fig. 3.13 illustrate the residual field integral fitting process which was done on the comparison between the signal calculation using the measured magnetic field profile and the measured signal (plot (a)) and the signal calculation after the addition of the residual field integral to the magnetic field profile (plot (b)). The red line in panel (a) shows a linear fit to the

points before the addition of the residual field integral. The reason the slope is not zero in panel (b) resulting from the relatively wide scattered of the points and reflects the error in the addition of the residual field from panel (a). A comparison

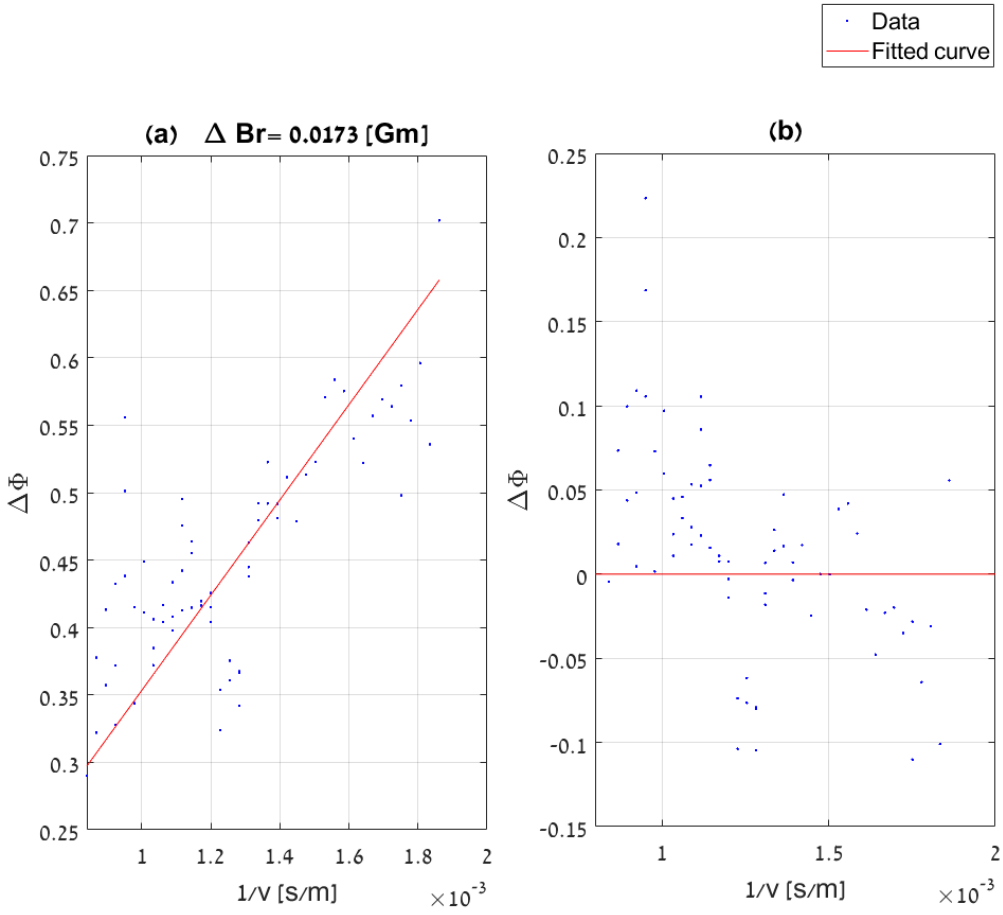

Figure 3.13: Phase analysis - (a) Extraction of the phases from the comparison of the measured signal and the signal calculated using the measured magnetic profile (b) analysis after addition of 0.017 Gm to the magnetic field profile calculation. The red line shows a linear fit to the scattered points

of the signal before and after the addition of the magnetic field can be seen in Figure 3.14 showing that when trying to analyse a direct analysis experiment, adding a small residual field integral of 0.017 Gm to our measured magnetic field profile significantly improves the fit of simulated and measured results. When looking at Fig. 3.13 we see that the phases extracted from the experimental

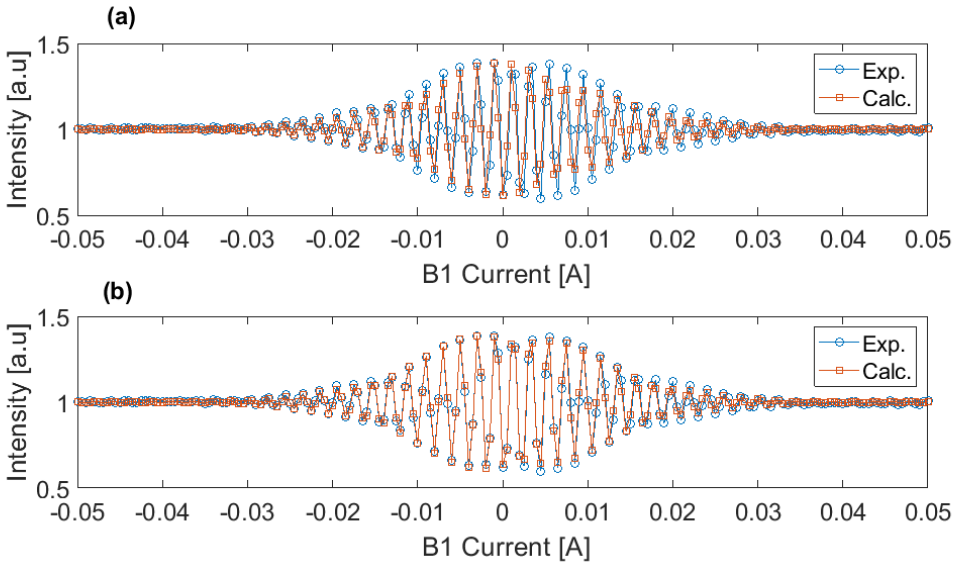

Figure 3.14: Calculation and measurement comparison - (a) 40 K measurement in blue and a calculation using the original magnetic field profile in red (b) a similar comparison after adding the residual magnetic field. The reason for the envelope clipping is the sample resolution in the current domain.

data are scattered (noisy) and there are systematic deviations from the model, especially at low values of 1/v, indicating that using a residual magnetic field along x to explain the results is an approximate approach which does not work very well at the limit of high velocities. Having said that, the absolute deviations in spin angle after applying the correction are rather small. In particular the agreement between the simulated and measured signals in Fig. 3.14 is quite good, suggesting that for many purposes the corrected magnetic field profile (adding a 0.0017 Gm residual field) is a good approximation.

3.4.2.4 Verifying the magnetic field profile in scattering mode

After establishing the magnetic field profile with the residual field correction for the direct analysis mode of the instrument, we want to check for the presence of a residual field integral in the scattering mode, using the same method as in the direct beam analysis. We choose to perform ^3He specular scattering from a Cu(111) surface as this surface is known to be quite reflective for scattering experiments and it is a non-magnetic material, so we are not expecting the helium

atoms to change their spin upon collision with the surface. In fact, we can treat the surface as a mirror, reflecting the incoming beam by 45 ° into the detector region. We kept the surface at 300 K and measured the scattered signal while scanning the current in the first solenoid and maintaining zero current in the second solenoid. We repeated these measurements for several nozzle temperatures and extracted the velocity distributions using the same process described above in 3.4.2.2. We then simulated the signal using the magnetic field profiles of the first arm (before scattering) and second arm (after scattering), applying an identity matrix as a scattering matrix to combine between the two and imposed the velocity distribution extracted from the experiment. Fig. 3.15 illustrates the residual field fitting process obtained from comparing the signal calculation, which uses the measured magnetic field profile, and the measured signal (plot (a)) and the signal calculation after the addition of the residual field to the magnetic field profile (plot (b)). A comparison of the signal before and after the addition of the magnetic field can be seen in Fig. 3.14, showing that for analysing a scattering experiment, a residual magnetic field of 0.012 Gm needs to be added to the magnetic field profile in the simulation to best match the measured results. The fact that two different values are obtained for analysing direct beam or scattered experiments can be expected, while the two types of measurements include a common beam path (source to scattering chamber) they have different beam paths later and the further residual fields can add up or cancel each other. Furthermore, the residual fields identified in the magnetic field profile measurement at the entrance and exit from the scattering chamber (the blue curve in Fig. 3.6 on both sides of the scattering chamber) are anti-aligned to the beam propagation direction and have a total field integral on the order of 0.25 Gm. If we have made an error of 5% when measuring these residual fields, it would explain why we need to add another small residual field to best simulate the data.

3.4.3 D_2 beam

By now we have carefully extracted the residual field integral values from the ^3He measurement to a degree where experiments and simulations of this system match

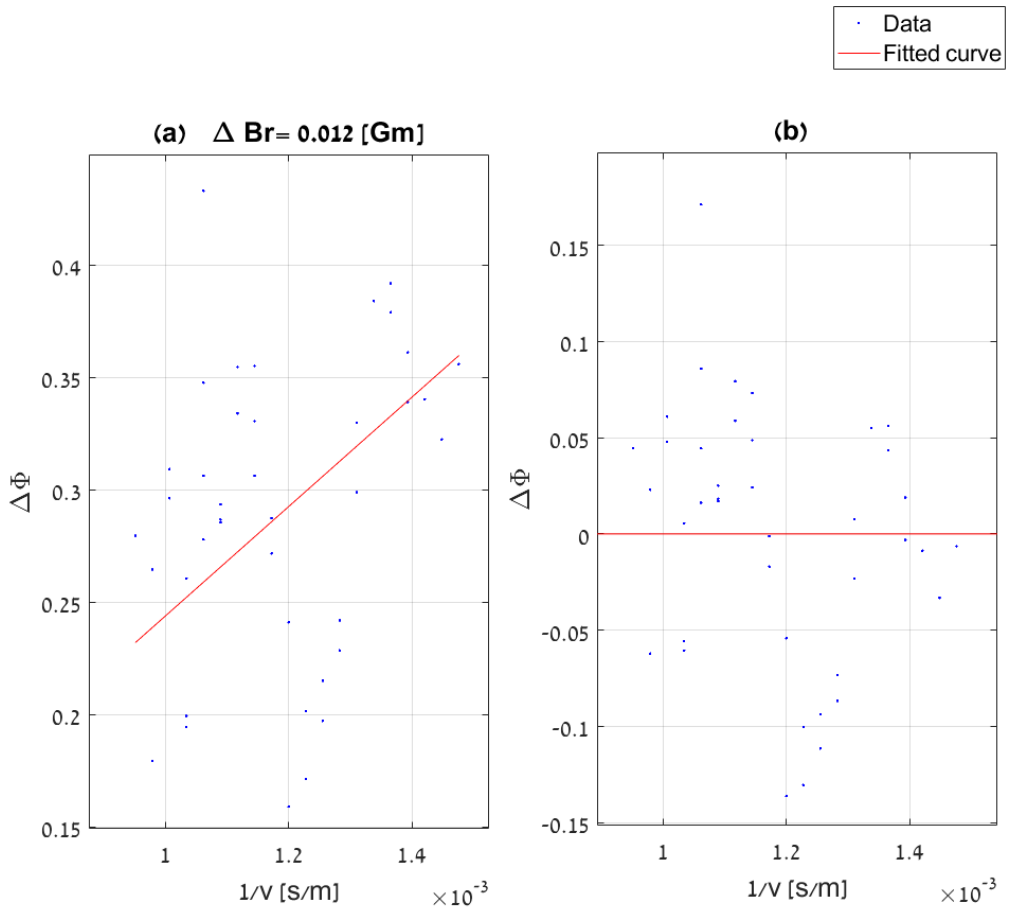

Figure 3.15: Phase analysis - (a) analysis of measured signal and signal calculated using the measured magnetic beam profile (b) analysis after addition of 0.012 Gm to the magnetic field profile calculation. The red lines show a linear fit to the scattered points

quite well. However, as ^3He magnetic scan measurement signals have only one frequency, they produce a simple pattern which is relatively easy to reproduce. Furthermore, since the magnetic scan measurement pattern for ^3He is insensitive to the hexapole probabilities, we want to test our measurement scheme on a more complicated system that we can still model. A molecular beam of deuterium is an example of a system that allows us to further test and verify the way we calculate the propagation through our setup.

3.4.3.1 Focusing

As D_2 molecules can be found in multiple total I and J states, we first need to discuss the relevant contribution of these states to the signal before we can simulate and compare to the measurements. Each D atom has a nuclear spin of 1, and correspondingly the D_2 molecule has 3 total nuclear spin states I=0,1 and 2. Deuterium atoms are Bosons, and the total wave function should be symmetric with respect to exchanging the nuclei. The even nuclear spin states (I=2 and I=0), termed the ortho-D_2 spin isomer, are symmetric with respect to an exchange of a nuclei and have 6 nuclear spin projection states (one from I=0 and 5 from I=2), and couple to even rotational states. The I=1 spin isomer, termed para-D_2, is anti-symmetric with respect to an exchange of a nuclei, it has 3 spin projection states, and couples to odd rotational states. When trying to compare calculated trajectories to the experiments we must take into account that we have twice as many ortho-D_2 molecules than para-D_2 molecules. We simulate separately the ortho and para trajectories and when summing their contributions to the simulated signal we give them the appropriate weight according to their state. When calculating the expected focusing of the beam. The I=1 group has 81 different quantum state projection combinations which need to be taken into account. This arises from the fact that the rotational ground state of I=1 molecules is J=1, giving rise to 9 m_I,m_J states, each having its own magnetic moment, and therefore a different focusing / defocusing behaviour within each lens. Taking into account the state mixing through the beam path between the lens, we are left with 81 different combination to consider. For example, a particle can start with a $(m_J, m_I) = (-1, -1)$ state in the first lens and to be a $(m_J, m_I) =$

$(-1, 0)$ in the second lens. The I=2 group will have just 25 states combinations as its rotational ground state is the non-rotating J=0 state, so just the nuclear spin projections are relevant. I=0 will have just one state to consider, as it's ground state is also J=0. In total, when simulating the trajectories propagation, 81, 25 and 1 runs will be needed for I=1, 2 and 0 (in practice some m_I, m_J projections, $(m_J, m_I) = (0, 0)$, $(m_J, m_I) = (1, 0)$ and $(m_J, m_I) = (-1, 0)$ are common to several I states so there is no need to re-run these again). It is however important to correct the weights before summing all of the signals to ensure that the spin statistic weight of 3/9, 5/9 and 1/9 for the I=1,2 and 0 states is maintained, as this is the relative population of the spin isomers when they emerge from the source. To address it, we will correct the total number of particles by 243, 45 and 9, i.e.

$$\begin{aligned} N'_{I=1} &= \tfrac{1}{243}N, \\ N'_{I=2} &= \tfrac{1}{45}N, \\ N'_{I=0} &= \tfrac{1}{9}N. \end{aligned} \tag{3.16}$$

Where N is the number of particles from the simulation and N' is the corrected number. After simulating the trajectories of the different groups and giving them the correct weights we should also take into account the quantum mixing state probabilities from the magnetic field profile along the machine (even though the magnetic solenoid is set to zero during the 2-D beam profile measurements, there are regions with non-zero magnetic field along the beam path, and some of the states (I=1, J=1) have mixing terms). A quantum propagation code has been used to extract the mixing matrix probabilities for the magnetic field profile of the machine. The code was written by Dr. Helen Chadwick, a member of the research group. Knowing the relevant mixing probabilities of each state, we are now in a position to compare between the measured and calculated profiles. The figures below present measurements and calculations of D_2 beam experiments using nozzle temperatures of 40 K and 60 K and comparison of the horizontal and vertical intensity cross sections. Note that the existence of multiple states with different magnetic moments and correspondingly different focusing properties, results in complex profiles composed of multiple peaks with different widths.

The 40 K data in Fig. 3.16 seems to have large broader contribution of unknown origin (discussed in 3.4.5), which leads to a significantly larger width up to about 50 percent of the maximum intensity when comparing with the simulation (Fig. 3.17). The 60 K data in Fig. 3.18 shows a better agreement with

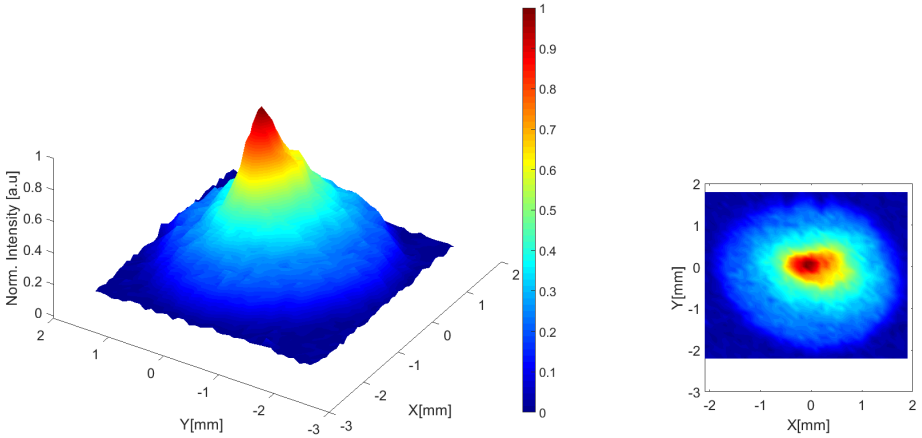

Figure 3.16: Intensity profile measurement of D_2 beam at 40 K - measured with a 0.4 mm square aperture

the calculation (Fig. 3.19) and suggest that the phenomena observed in the 40 K data has less effect on the measured intensity in this case. Fig. 3.20, 3.21 shows the horizontal and vertical profiles from the 2-D scan, the reasons for the discrepencies will be discussed later on 3.4.5. Also, due to very low transmission of particles in the simulation (especially on the 60 K data), the bumps in the simulation are result from convergence noise.

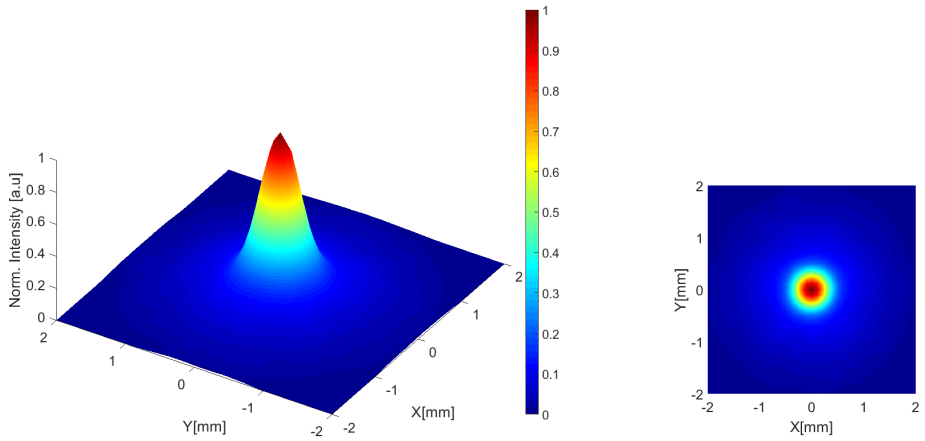

Figure 3.17: Intensity profile simulation of D_2 beam at 40 K -

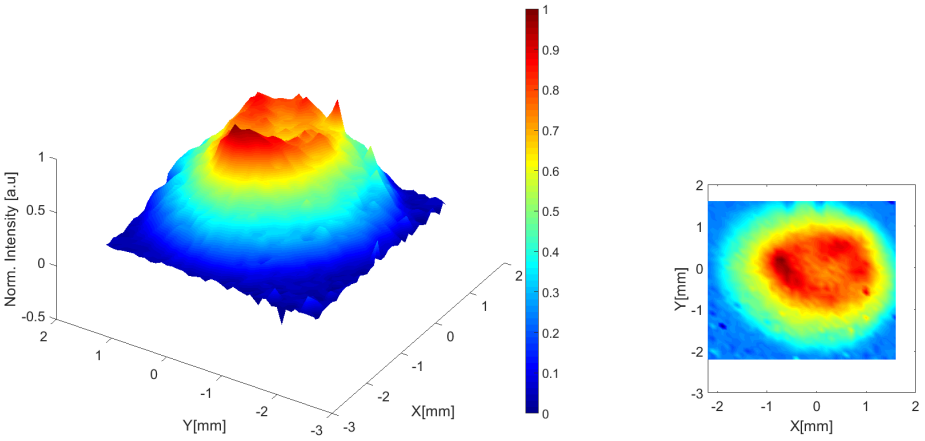

Figure 3.18: Intensity profile measurement of D_2 beam at 60 K - measured with a 0.4 mm square aperture

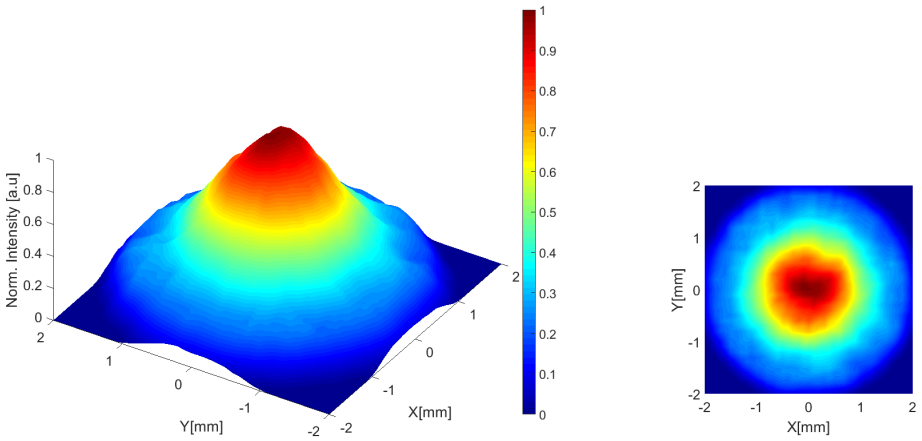

Figure 3.19: Intensity profile simulation of D_2 beam at 60 K -

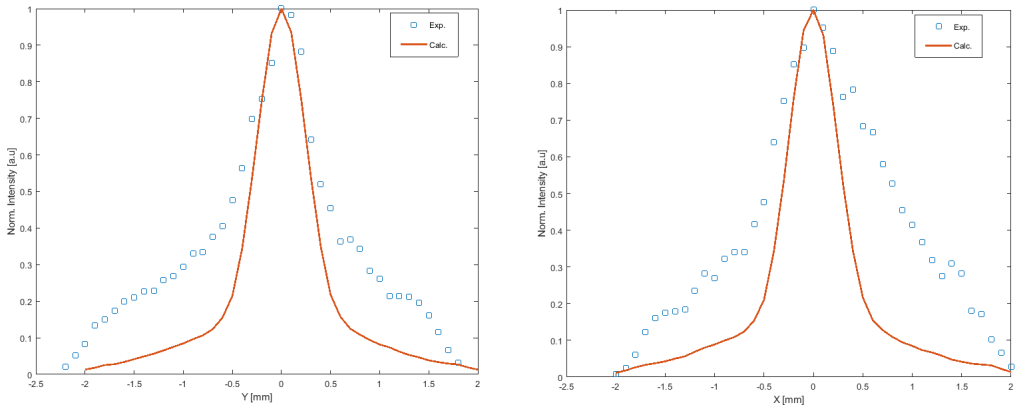

Figure 3.20: Horizontal and vertical comparison, 40 K - comparison of the measured and calculated profile

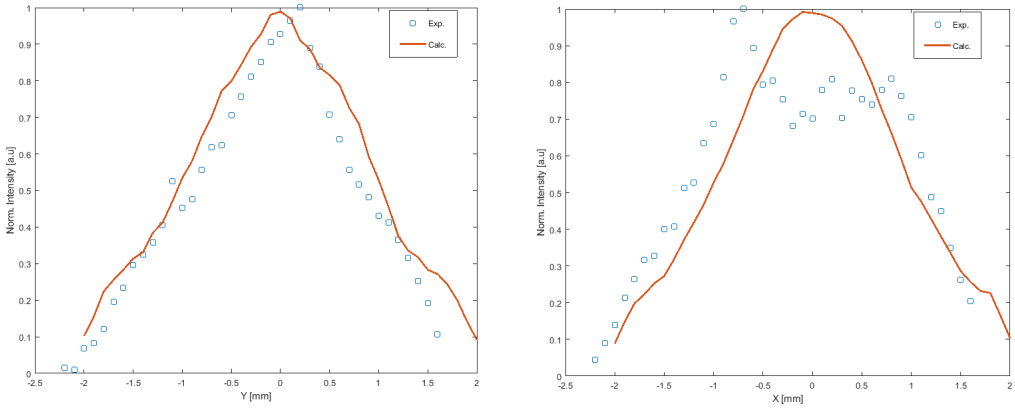

Figure 3.21: Horizontal and vertical comparison, 60 K - comparison of the measured and calculated profile

3.4.3.2 Magnetic scan measurements

Similarly to the case of ^{3}He, we also performed magnetic scan measurements, where we scanned the current in the first solenoid (B1), while measuring the intensity of the D_2 beam, using a 1 mm square aperture positioned at the centre of the beam profile. The measurements were performed for nozzle temperatures of 40 K and 60 K. From the measurements we can extract the velocity distribution of the molecular beam if we use the known gyromagnetic ratio of D_2 in the same manner as in the ^3He beam case but with some care, as the D_2 beam has more than just one signal frequency we used the I=2 J=0 state frequency to determine the velocity distribution as we can clearly see it is the dominate frequency. Fig. 3.22, 3.23 show the magnetic scans at nozzle temperatures of 60 K and 40 K with a comparison to quantum simulations of a D_2 beam performed for I=2 J=0 and I=1 J=1 states. These states were chosen as we did not observe peaks corresponding to any other states in the experimental spectra. The simulated particles travelled at 798 m/s with a FWHM of 9% for the 60 K data and 649 m/s and FWHM of 8% for the 40 K data.

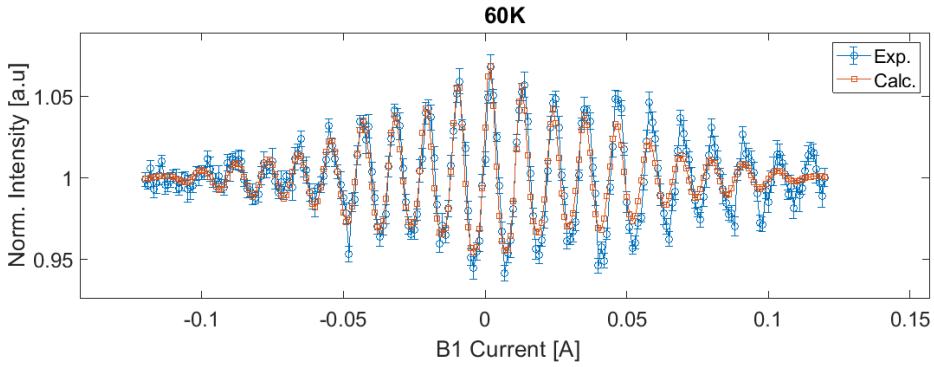

Figure 3.22: Calculation and measurement comparison of D_2 magnetic scans - nozzle temperature of 60 K, the blue points mark the measured data with the error bars mark the standard deviation from the point's mean. The red line is the calculation using the corrected magnetic profile of the machine

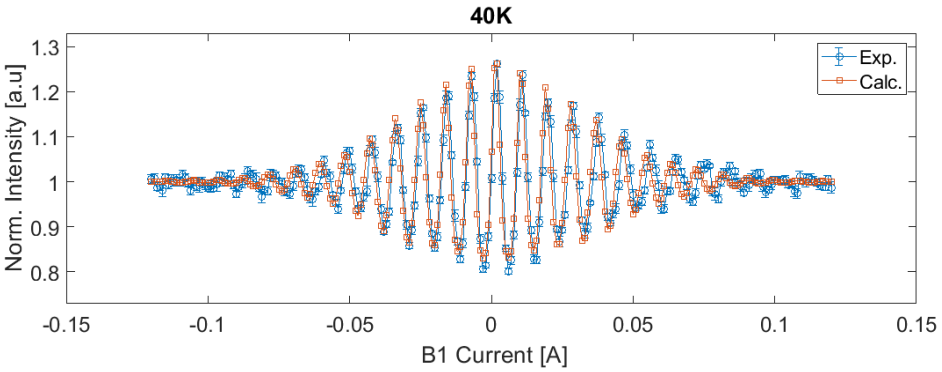

Figure 3.23: Calculation and measurement comparison of D_2 magnetic scans - nozzle temperature of 40 K, the blue points mark the measured data and their error bars mark the standard deviation from the point's mean. The red line is the calculation using the corrected magnetic profile of the machine

3.4.4 H_2 Beam

The measurements performed on ^{3}He are only sensitive to the overall value of the magnetic field integral and not to its position or specific shape. This is also mostly true for D_2, since the dominant contribution is from the non-rotating J=0 state, whereas J=1 and J=2 contribute less to the measured signal. When considering a H_2 beam the signal corresponds to I=1, J=1 molecules and rotations can not be ignored. As a result, the magnetic Hamiltonian for H_2 has field independent terms, and magnetic scan measurements are sensitive to the actual location and shape of the magnetic field profile. Below we present 2-D intensity profiles and magnetic scan measurements performed with a molecular hydrogen beam. These measurements allow us to to verify our ability to simulate the propagation of molecular hydrogen through our setup, which forms the basis for analysing surface scattering experiments (chapters 4 and 5).

3.4.4.1 Focusing

In Fig. 3.24, the measured profile of molecular hydrogen beam intensity is presented, measured with a square 0.4 mm aperture moving in 0.1 mm step resolution. The diameter of the beam at half maximum is about 0.7 mm which is

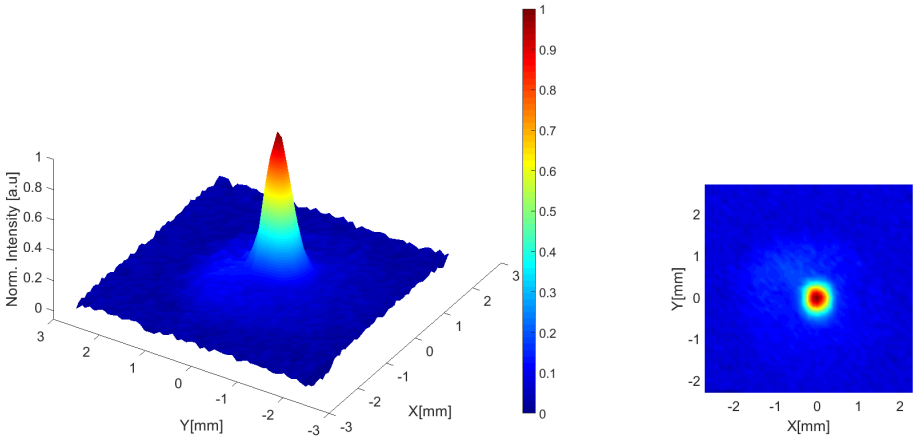

Figure 3.24: Intensity profile measurement of H_2 beam at 100 K - measured with a 400 micron square aperture

5 times narrower than a helium-4 beam expanded from the same nozzle at the same temperature. In order to simulate the profile shape, we need to take into account the zero field mixing of the different quantum states in the beam. As the Hamiltonian for the case of hydrogen has field independent terms, the states will evolve even without applying a magnetic field in the solenoid. To consider this phenomena, we calculate the propagation of the states through the setup with a zero current in the solenoid (similar to what was done in the the experiment) to obtain a mixing matrix, where the M,N element of the matrix is the probability that a M in the first hexapole will become a N state in the second hexapole. After calculating the mixing matrix, a trajectory simulation for each of the possible quantum state combinations has been made, resulting in a 2-D state-specific flux at the sliding aperture position. Each state was then multiplied by its mixing matrix element and summed in the same manner as the measurement scan (summing over a 0.4 mm square with 0.1 mm steps). The x and y 1-D profiles are shown in Fig. 3.25 together with the calculated ones. The results show an overall good agreement between the two (the reasons for the residual discrepancies will be discussed in 3.4.5), enhancing our confidence in the trajectories calculation.

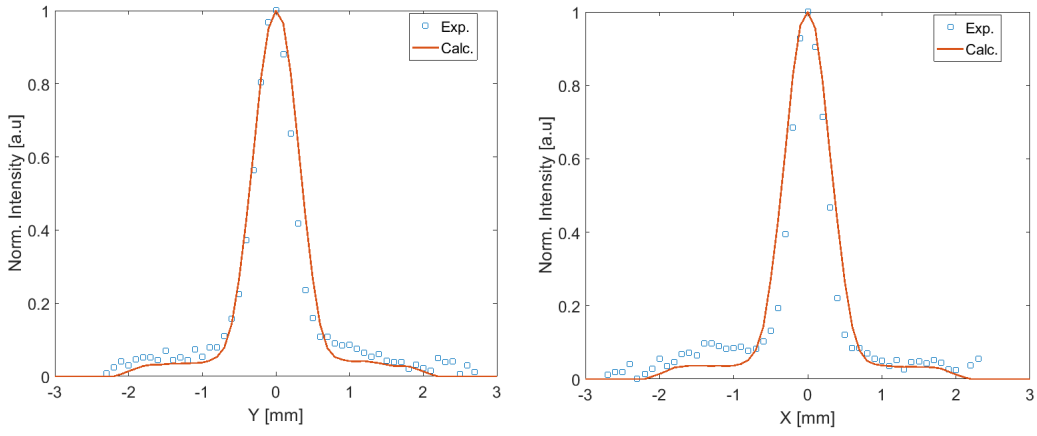

Figure 3.25: Horizontal and vertical comparison, 100K - comparison of the measured and calculated profile

3.4.4.2 Magnetic scan measurements

We scanned the magnetic field in the solenoid, B1, and measured the intensity of the H_2 beam as a function of the applied current in the solenoid. The measurements were done at a nozzle temperature of 100 K and the final aperture position and size was changed so we can measure at different regions of the 2-D profile of the beam. Different positions and different aperture sizes change the relative weights of the quantum states and should result in different signals. Three measurements were performed at the center of the beam profile using 0.2, 0.4 and 1 mm square apertures, another measurement was performed on a rectangular 0.2×4 mm aperture positioned 1.3 mm off centre (illustrated in red , Fig. 3.26).

Fig. 3.27 to 3.30 show the different magnetic scans measured for the differ-

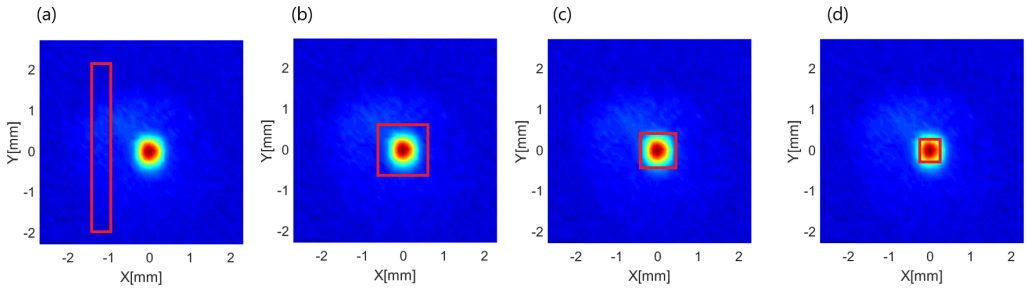

Figure 3.26: Different measurement conditions - (a) 0.2×4 mm rectangular positioned 1.3 mm off the centre. (b) -(d) 1, 0.4, 0.2 mm square apertures at the centre.

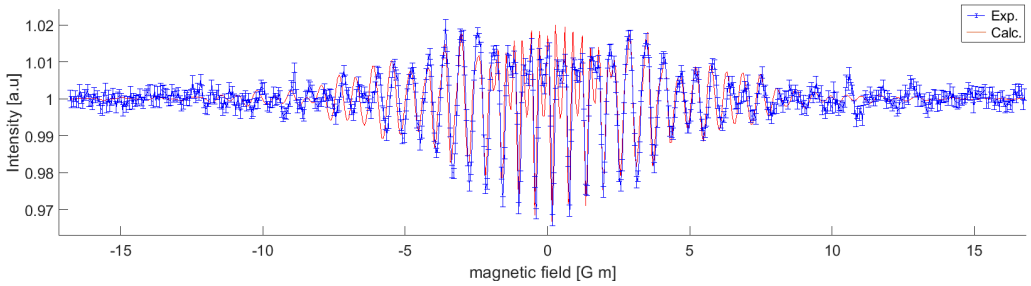

Figure 3.27: Magnetic scan - measured at condition (a)

ent aperture size and position conditions (blue – measurements, red – simulated scans).

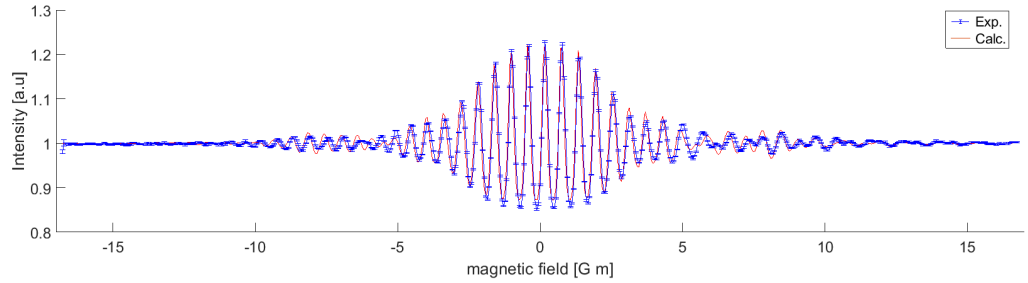

Figure 3.28: Magnetic scan - measured at condition (b)

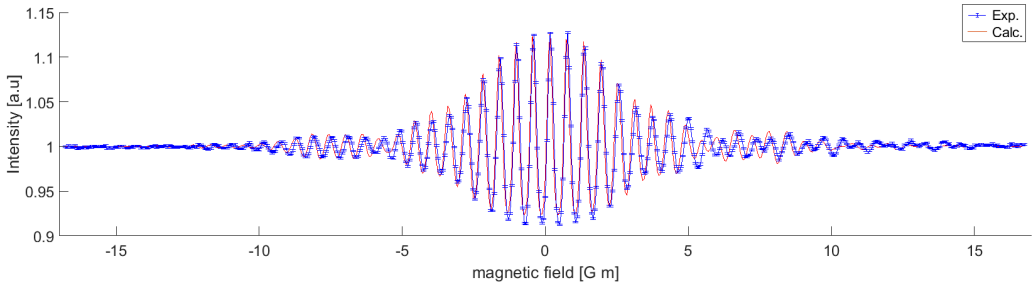

Figure 3.29: Magnetic scan - measured at condition (c)

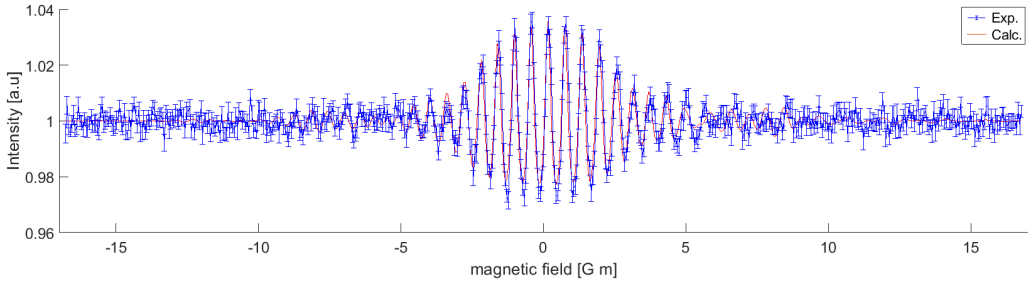

Figure 3.30: Magnetic scan - measured at condition (d)

3.4.4.3 Extracting Velocity from magnetic scans

As we mentioned in the D_2 case, due to the different frequencies involved, different states which correspond to different gyromagnetic ratio can interfere with each other, this results in a much more complex behaviour. To bypass this, we choose to fit the velocity distribution so that the Fourier transform of the signal and the simulation match. In order to do so, we first tried to understand how many parameters are needed in order to describe the velocity distribution. We tested a simple Gaussian with a mean velocity and velocity width as parameters, we tried a combination of 3 Gaussian distributions, a triangular and square distributions and 10 steps distribution function. The results were in favour for the simple Gaussian distribution with only 2 parameters, the mean velocity and the velocity width. By scanning the 2-D parameters we end up with a mean velocity of 1456 m/s (a 1% deviation from the expected nozzle temperature velocity) and a FWHM width of 5.7 % for the measurements presented.

3.4.5 Discussion

As we go over the results in this chapter, our first observation was that the ^4He beam profile (Fig. 3.8) is imaged as a homogenous intensity disc with a diameter of approximately 3.5 mm diameter. The fact that just before the detector's sliding apertures we have a 4 mm aperture suggests that somewhere along the beam line we have interference that causes the full beam to be smaller than we expected. When measuring beams with a magnetic moment, $^3He, D_2$ and H_2 (Fig. 3.9, 3.16, 3.18 and 3.24), the shape of the profile measurement is very different with respect to the ^4He profile. The focusing effects of the hexapoles are seen as distinct peaks in the intensity distribution instead of the homogenous disc-like intensity of helium-4.

The comparison between the profile measurement and the calculation in the case of the ^3He beam (as seen in Fig. 3.11) puts the FWHM of the calculation within the uncertainty of the measurement (we get those by considering the different width of the horizontal and vertical profiles of the measurement) and allows us to simulate the trajectories along the machine with confidence. Next, we used the ^3He magnetic scan experiments to detect small hidden magnetic fields,

which we have either missed when we measured the magnetic profile, or are related to the limited accuracy of our measurements in both the direct beam line setup and in the scattering setup. The results shown in the analysis (Fig. 3.13) illustrate the implementation of the residual magnetic field upon the simulation of the measured signal. As we can see in this figure, there is a systematic error at the high velocity points, indicating that our model for a simple residual field integral is limited to a particular velocity range. One possible explanation of this is that beams with larger velocities have larger diameters (they are less focused) and might be sensitive to residual fields which are further away from the beam centre. Nevertheless, in the region which are most likely to be measuring (the middle of the graph), the points are found to be scattered around 0 which is what we expect from implementing the residual magnetic field on the simulation. In the case of the magnetic scan (Fig. 3.14), the relatively high agreement between the calculation and the simulation after the addition of the residual magnetic field demonstrates that the additional residual magnetic fields we extracted from the measurements should be included in the magnetic beam profile for more accurate modelling of the data. In the case of the scattering experiments, the analysis gives similar conclusions but different residual magnetic field integral value, that is reasonable considering that the particles are travelling through different paths in the two different setups.

When we are look carefully at the D_2 data that we acquired, a strange behaviour can be seen in the comparison of the two different velocities (resulting from a 40 K and 60 K nozzle temperatures). The width of the 40 K profile (FWHM=0.6 mm) is narrower than the 60K profile (FWHM=2 mm). This was also predicted in the simulations (see Fig. 3.20 and 3.21 for the comparisons). However, the 40 K profile is much wider in the low intensity parts than the simulation. This discrepancy could be related to the alignment of the hexapole itself and the fact that in the 60 K profile measurement we can see a good agreement between the profile measurement and the simulation can be explained that when travelling faster (there is 149 m/s difference in velocity between the 60 K and 40 K nozzle temperatures) through the hexapole, we are less sensitive to the alignment of it because the particles travel less time inside the hexapole magnetic field and correspondingly are deflected less. If one needs to improve the alignment of the

hexapole, this should be done using experimental data measured at low velocities (40 K nozzle in the case of D_2 which correspond to 649 m/s). Furthermore, we presented a magnetic scan comparison at the two different nozzle temperatures. As can be seen in Fig. 3.22, the overall behaviour of the signal with respect to the calculation is quite similar with just the exception of a slight discrepancy in the right lobe of the signal envelope which could be related to the actual shape of the velocity distribution we choose to simulate the signal with (a Gaussian, as opposed to a more complicated asymmetric velocity distribution). The measurement at 40 K in Fig. 3.23 shows a better agreement in the envelope than the 60 K data but there is a noticeable phase shift at the lobes (further on from 0.05 A and the same in the other direction). One possible reason for this is if transmission probabilities through the second hexapole are not accurate for the 40 K measurement due to the slight misalignment of the hexapole we have discussed above.

In the case of a H_2 beam, we can see in Fig. 3.25 that our profile simulation slightly overestimates the measurement (FWHM of the measurement is 5.7±0.4 mm and the FWHM of the simulation is 7.2 mm) this again could be related to the alignment of the hexapole that can create a different width for the different H_2 states than a perfectly aligned hexapole would. After acquiring the intensity profile of the H_2 beam, we performed magnetic scan measurements for different aperture sizes, shapes and positions. The overall agreement between the simulation and the measurement is good, and the quite different signal shapes for the different aperture conditions are mimicked by the simulation. Nevertheless, we can find some discrepancies between the measurement and the simulation. At the centre of the off-center aperture measurement there is a fast frequency component which has a higher amplitude in the simulation than in the measurement. Also, there are some phase shifts between them on the lobes (up to about -5 Gm and further on from 5 Gm). These discrepancies could be related to differences between the real transmission probabilities and the calculated ones. Further in-vacuum optimization of the hexapole should be performed at first stage, this will require measuring the beam intensity profile after each movement of the hexapole until a better agreement between the calculated and measured profile is achieved. If discrepancies in the magnetic scans are still apparent when the profiles suggest

that the hexapoles are aligned, we should explore other possible reasons which could give rise to these discrepancies.

4

H_2/LiF(001)

In this chapter we present measurements of ground state H_2 molecules colliding with the (001) surface of a Lithium Fluoride (LiF) single crystal. This study, which is the first quantitative MMI study, demonstrates how MMI measurements, when combined with numerical modelling can be used to study changes in the molecular wave function during scattering as well as study how the rotational orientation of the molecule changes the scattering probabilities. From the analysis we see that collision of H_2 with LiF change the rotational orientation of the molecule (rotational flips), in accordance with a previous theoretical prediction [45]. Furthermore, the quantum state-to-state scattering probabilities depend on the initial and final rotational orientation of the molecule showing that a LiF surface can be used to rotationally polarise the outgoing H_2.

4.1 Sample preparation

The sample was prepared by cleaving (in air) a single crystal LiF sample (Crystran Ltd) and transferring it within minutes into an ultra-high vacuum (UHV) chamber (P = 10^{-10} mbar), where it was mounted on a home-built non-magnetic 6-axis sample manipulator with heating, cooling and sample transfer capabilities. To provide us with heating and cooling capabilities, we had to design a new sample holder that couples the sample to both a commercial UHV button heater (Heatwave Labs) and a liquid nitrogen cooled cryostat. The specific sample holder was needed as our regular sample holders were designed for metallic

samples, and use radiative heating from a filament. We have observed that the low energy electrons emitted from filaments damage the LiF surface, furthermore, the transparency of the sample makes radiation also rather ineffective. Fig. 4.1 shows a picture of the sample holder, under vacuum, connected to the sample manipulator.

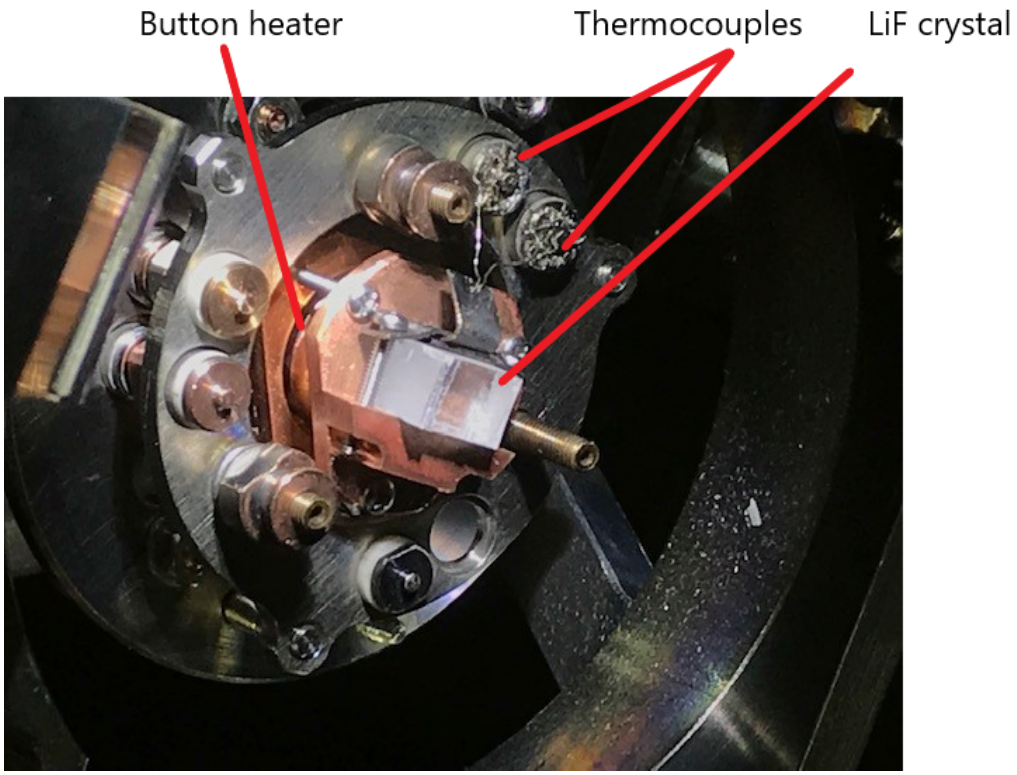

Figure 4.1: LiF sample holder - mounted inside the vacuum chamber

After inserting the crystal into the UHV chamber, it was flash annealed to 450 K and the quality of the surface was verified by obtaining a very narrow specular peak (FWHM 0.07 °) and the expected diffraction pattern. The crystallographic azimuths were determined, with an estimated uncertainty of less than 0.5 °, by performing diffraction scan measurements and aligning the azimuthal angle such that both the (-1,0) and (1,0) diffraction peaks from the LiF surface can be seen in one polar angle scan without adjusting the tilt or azimuthal angles. Fig. 4.2 illustrates the scattering process together with the different rotations of

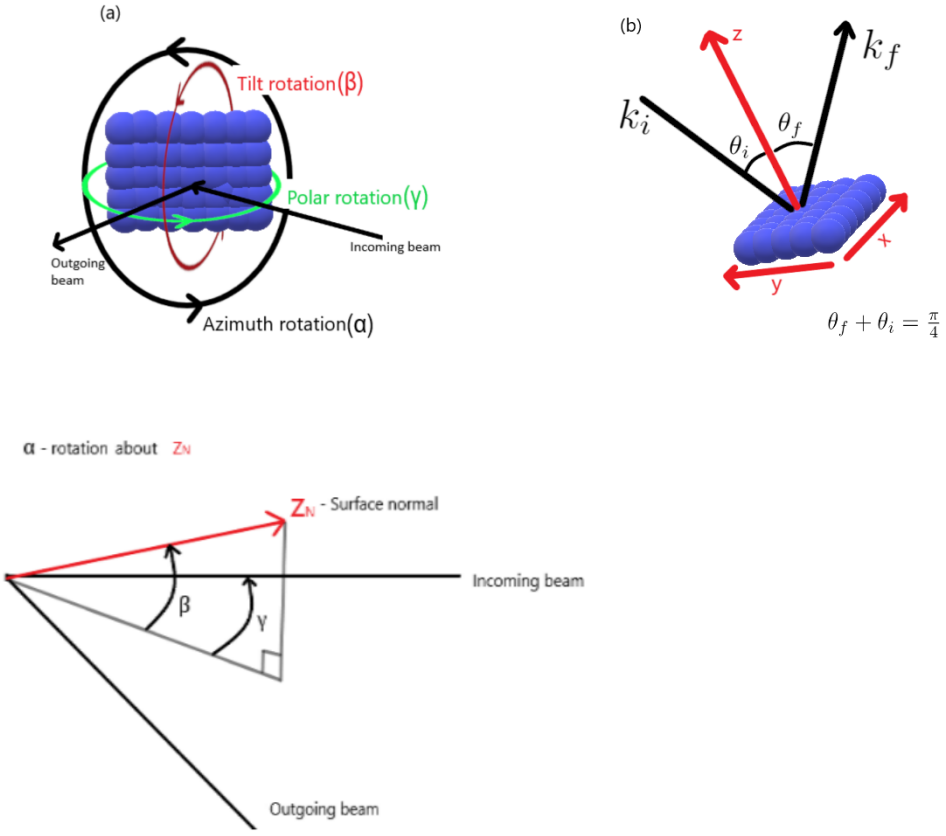

Figure 4.2: Surface and instrumental notations - (a) the different rotations of the surface (b) schematic of incoming and outgoing wavevectors

the surface- polar (γ), tilt (β) and azimuth (α). The tilt angle measures the relative angle between the surface normal and the scattering plane (the plane

which includes the incoming and outgoing beam). The polar angle measures the orientation of the surface normal with respect to the incoming beam and is set to zero where the surface normal and the incoming beam are on the same plane. The azimuth angle is used to denote the crystallographic axis within the surface plane which the wavevector of the incoming beam projects onto.

4.2 Alignment measurement

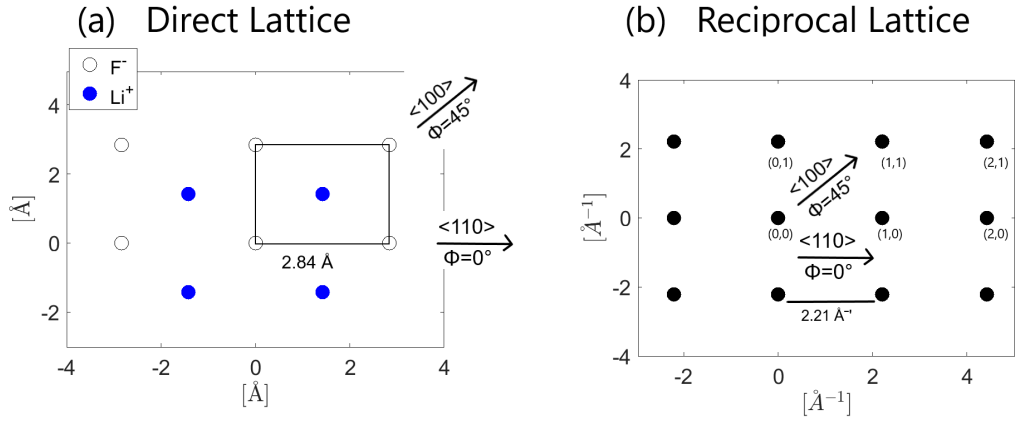

Figure 4.3: Real and reciprocal lattice of the LiF(001) surface - with marks of the crystallographic azimuths and distances

Fig. 4.3 illustrates the real and reciprocal lattices of the LiF(001) surface, with the unit cell marked as a square (dimensions are taken from [46]). To align the surface, we first need to calculate the position of the expected diffraction peak from the geometrical constrains of the machine and the beam energy.

Consider the kinetic energy of the beam to be

$$E_{Kinetic} = \frac{5}{2}k_B T = \frac{\left(\hbar\vec{k}\right)^2}{2m}. \tag{4.1}$$

Here T, m and $\vec{k}$ are the nozzle temperature, particle mass and wavevector re-

spectively. Solving for $\vec{k}$ in Eq.4.1 yield

$$\left|\vec{k_i}\right| = \frac{\sqrt{5k_BTm}}{\hbar}. \tag{4.2}$$

The well known Bragg condition for diffraction in a 2-D lattice is

$$\vec{K_G} - \vec{K} = \vec{G}, \tag{4.3}$$

where $\vec{K}$ and $\vec{K_G}$ are related to the incoming and outgoing wavevectors by $\vec{k_i} = (\vec{K}, k_{iz})$ and $\vec{k_f} = (\vec{K_G}, k_{Gz})$ and they represent the components of the wavevectors within the surface plane. k_{iz} and k_{Gz} are the components along the surface normal of the incoming and outgoing wavevectors respectively. $\vec{G} = h\vec{b_1} + k\vec{b_2}$ is the reciprocal lattice vector and $h, k \in Z$ are integers used to indicate the particular diffraction channel (see Fig. 4.3 (b)). In our measurements we positioned the surface so that $\vec{G}$, $\vec{K_G}$ and $\vec{K}$ are coplanar and the vector equation in the Bragg condition can be reduced into a one dimensional equation which for the case of elastic scattering ($|\vec{k_i}| = |\vec{k_f}|$) is

$$|\vec{k_i}|(sin(\theta_f) - sin(\theta_i)) = |\vec{G}|. \tag{4.4}$$

The total angle between the incoming arm and outgoing arm is fixed at a an angle of ca. 45 ° (we mark it by Δ), if we set the polar angle (γ) to $\Delta/2$ at specular condition ($\theta_i = \theta_f$) the above equation could be simplified to

$$\frac{\sqrt{5k_BTm}}{\hbar}(sin(\Delta - \gamma) - sin(\gamma)) = |\vec{G}|. \tag{4.5}$$

As each surface is characterised by its own reciprocal space vectors, the (h,k) diffraction peak can be detected at the outgoing arm detector for a specific γ value which satisfies the equation above. The reciprocal lattice vector of the LiF(001) can be expressed as $\vec{G} = 2.21\,\mathring{A}^{-1}(h\hat{x} + k\hat{y})$. The calculation of the position of the polar angle can be made as follows-

- Calculate the initial wavevector from Eq. 4.2 using the particle mass and nozzle temperature

- Choose a specific channel with the reciprocal lattice vector $\vec{G}$ and align the surface azimuthal angle accordingly
- Solve for γ in Eq. 4.5
- For conveinnce, we can change again the reference point and set $\gamma = 0$ at $\Delta/2$ so we can have a relative value of the diffraction peak position with respect to specular position.

For example, in the case of a molecular hydrogen beam , a source temperature of 100 K and the (h,k)=(1,0) diffraction channel we get $|\vec{k}_i| = 4.54\mathring{A}^{-1}$ and $|\vec{G}| = 2.21\mathring{A}^{-1}$, inserting these values into Eq. 4.5 yields

$$sin(\Delta - \gamma) - sin(\gamma) = 0.48, \tag{4.6}$$

and solving for γ gives $\gamma = 7.3\,^\circ$, or a rotation of $15.2\,^\circ$ from the specular peak position ($\frac{\Delta}{2} - \gamma = 22.5 - 7.3 = 15.2\,^\circ$). Due to the symmetry of the lattice, we expect that the diffraction peak corresponding to the (h,k)=($\overline{1}$,0) (where the bar above the number means it is a negative number), to be at a rotation of $15.2\,^\circ$ from specular in the other direction. For (h,k)=($\overline{1}$,$\overline{1}$) and (1,1) the reciprocal vector is $|\vec{G}| = 3.12\mathring{A}^{-1}$ and we get $\gamma = 0.2\,^\circ$ which means a rotation of $22.3\,^\circ$ from specular in both directions. Fig. 4.4 shows the measured angular scans of H_2 scattered from LiF(001) in the $< 110 >$ ($\alpha = 0$) and the $< 100 >$ ($\alpha = \pi/4$) crystal azimuths. The position of the diffraction peaks are in agreement with the calculation presented presented above. above. This alignment procedure is important for several reasons. First of all we want to be sure that the surface has the structure we expect it to, and that any contaminations or defects which are present are not contributing significantly to the scattered signal. A second reason, is that eventually, experiments of the type we will present can be compared with theoretical calculations. For this comparison to be meaningful we need to supply the theoreticians with the exact conditions and scattering geometry of the experiment. Finally, the ability to get reproducible diffraction patterns from the surface suggest that the cleaning procedure and preparation of the sample are sufficient and reproducible. The width of the diffraction peaks, in terms of the polar angle, gamma, is the outcome of the velocity spread of the beam, since

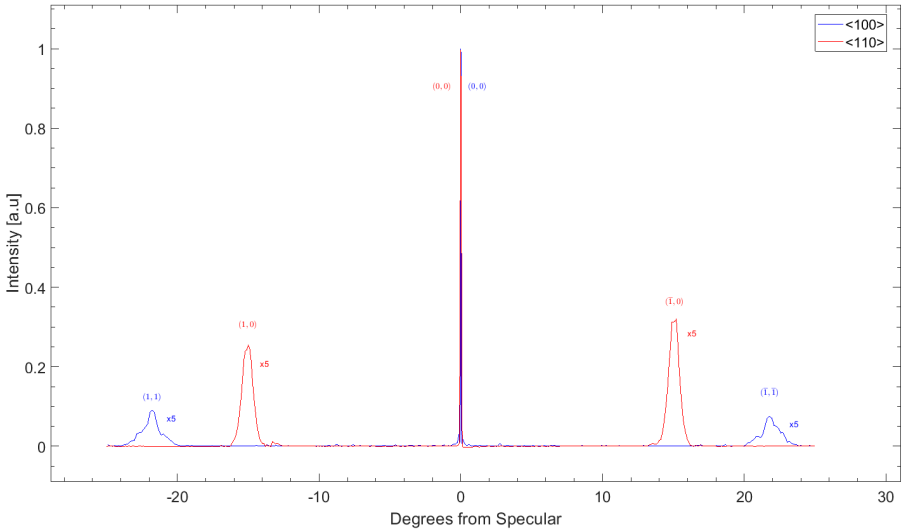

Figure 4.4: Angular scan of H_2 from LiF(001) - in the $< 100 >$(blue) and $< 110 >$(red) directions. Measurements were performed for a surface temperature of 165K and a nozzle temperature of 100K

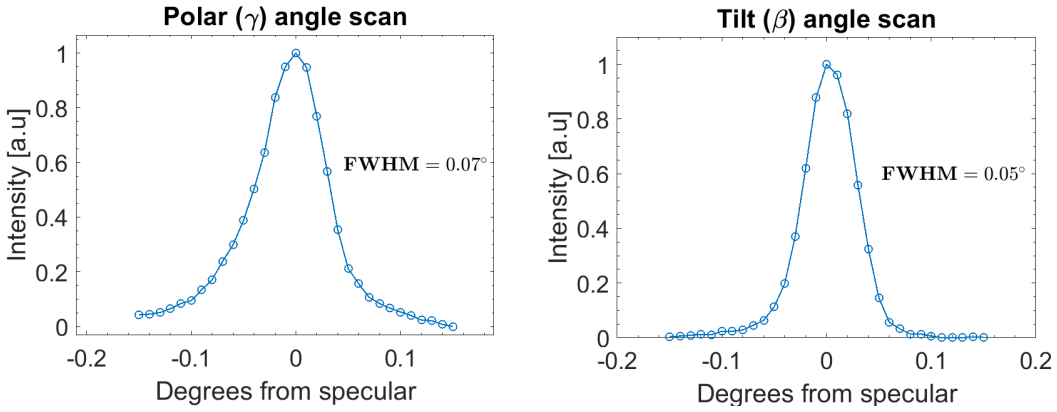

Figure 4.5: Scans of the specular peak - Polar and tilt angular scans

for each velocity (energy) component within our beam, the diffraction condition is met at a different angle. In the case of our measurements, the data for the diffraction peaks was acquired by positioning the polar angle at a particular polar angle (nominally chosen as the maximal peak intensity). Since our instrument is characterised by a high angular resolution (approximately 0.04 °), measuring the scattered beam at a particular polar angle effectively filters out a large portion of the velocity distribution for the measured signal, leaving a velocity distribution with a FWHM of 0.5% in the case of diffraction peak measurements. An exception to this phenomena, which can be seen in Fig. 4.5, is the specular peak $(h, k = 0)$. In this case the diffraction condition is met for all velocities at the same angle $(\theta_i = \theta_f)$ and the width of the diffraction peak is not broadened by the velocity distribution of the beam. For a perfect crystal (infinite and defect free domains) the finite width of this peak will be related to the angular resolution of the instrument, which we estimate as 0.04 °. Correspondingly if the measured width is of that order this means that the effect of surface defects is negligible. All this information is crucial for comparing our results to theoretical calculations and / or results obtained with different experimental techniques. A better understanding of the experimental conditions and of the surface we studied, makes our results more valuable as accurate benchmarks for theoretical calculations.

4.3 Current scan measurements

The experiment uses a magnetic field manipulation technique for both particle deflection and coherent wavefunction control. Here, we will discuss the key aspects of the experimental method, in the context of the particular H_2 experiment described in this chapter.

A molecular beam is formed by a supersonic expansion of a pure H_2 beam through a cold (100 K) nozzle. The beam velocity at this nozzle temperature results in optimal focusing of H_2 within the hexapole lens and results in a maximal molecular beam flux at the scattering chamber. The cold beam is a mixture of the two lowest rotational states, the J = 0 singlet of para-hydrogen, and the J = 1 triplet of ortho-hydrogen. The former is not affected by magnetic fields and provides a constant background in our experiments while the latter splits within

a magnetic field into nine different quantum states that can be represented by the nine combinations of the nuclear spin projection m_I and the rotational projection, m_J quantum states (see Fig. 4.6). The expanded beam, exits the source chamber, passes through a couple of differential pumping stages and then enters into the first magnetic lens (first hexapole). Passing through the magnetic lens results in different trajectory deflection for the different H_2 quantum states, corresponding to their magnetic moments. To understand the principle behind the magnetic

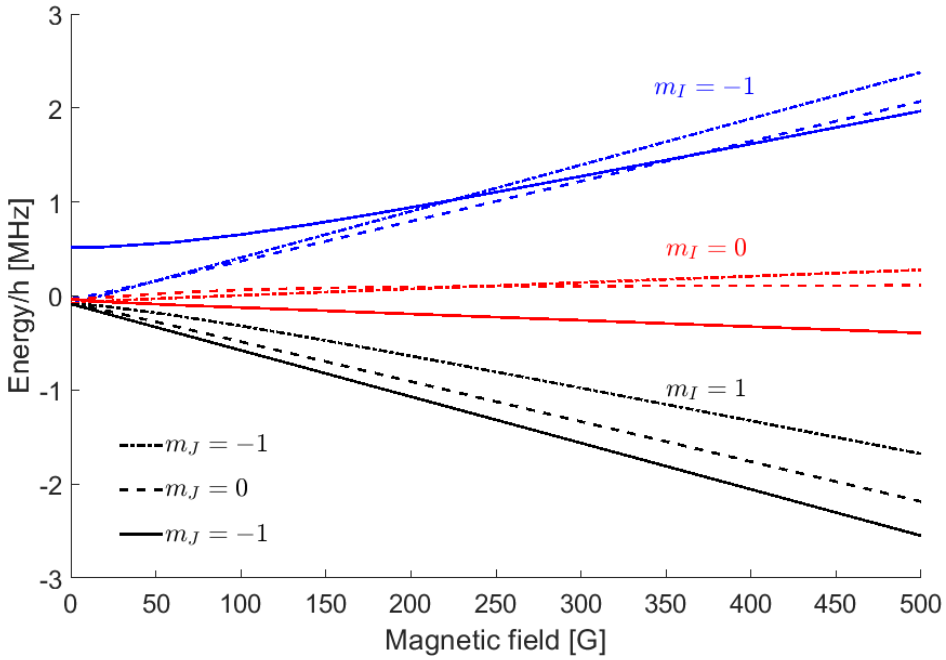

Figure 4.6: Field dependence of the H_2 Ramsey eigenenergies [3] - the different states energy as a function of the applied magnetic field

lens (explained in section 2.3.1), Fig. 4.6 shows the energy of the different m_I, m_J states of H_2 as function of the applied magnetic field. The states split into three main groups which corresponds to the nuclear spin projection and a much subtler secondary split based on their rotation projection. While the relatively large nuclear spin state splitting at large field values offers a way of separating these states, the limited splitting of the rotational states make it extremely difficult and even impossible to separate a specific (m_I, m_J) state. Furthermore, the non-linear behaviour of the energy results in the lines crossing each other and reflects the

non-negligible coupling between the nuclear and rotational magnetic moments. This means that even a pure (m_I, m_J) state would mix into a superposition state within tens of micro-seconds unless a sufficiently strong magnetic field is maintained [15]. The strength of the magnetic field gradients within the hexapole lens (>T mm^{-1}) results in initially pure m_I, m_J states in the Z frame of reference [30]. At the point of exit from the first hexapole, the beam is no longer equally populated in all nine states and a dipole field is introduced adiabatically, which forces the quantization axis to point along a well defined direction in the lab frame of reference (Z axis). In between the dipole region and the first solenoid, which generates an electromagnetic field, B1, oriented along the -X axis, a non-adiabatic transition occurs. This transition transforms the initially pure (m_I, m_J) states in the Z frame of reference into a superposition along the quantization axis of the solenoid. Within the B1 field, the coherent evolution of the superposition states is given by the Ramsey Hamiltonian [3]. Fig. 4.7 shows the calculated populations of the different states as they approach the surface and demonstrates our ability to control the relative population as we control the applied magnetic field in the first solenoid.

Once the beam approaches the surface it can scatter into one of the diffraction channels and the quantum state changes again, this time due to the interaction potential with the surface. This change, which reflects the physics and chemistry of the collision, can be described using the scattering matrix, (S-matrix), which relates the molecular wave function before and after scattering. After the scattering event, the scattered beam travels through the second solenoid with a magnetic field strength of B2 directed along the -X' axis. In this region, the states are again evolving coherently, and can be controlled by changing the field strength, B2. The next step is the transition from the second solenoid to a dipole field (-Z' direction) which sets the quantization axis of the particles that are being measured. After establishing the required quantisation axis, the beam enters the second heaxapole which then transmits them towards a particle detector with a transmission probability that depends on the magnetic moments of the states. The magnetic scans were done by aligning the sample to a particular diffraction condition and then measuring the detected signal while altering the current in the first solenoid. The current was scanned from 0 A to 0.15 A, which changes the

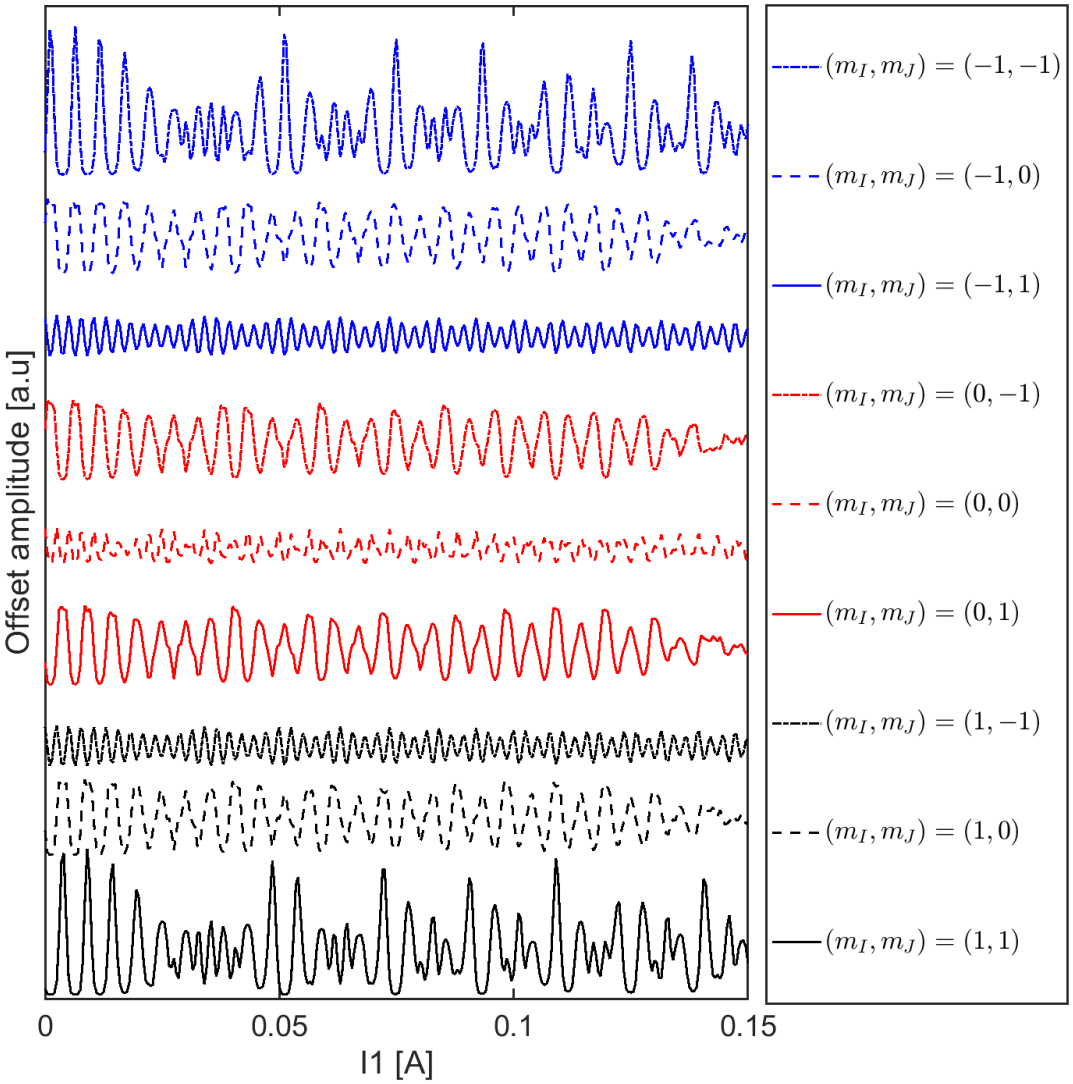

Figure 4.7: Ortho-hydrogen states behaviour in a magnetic field - Calculated populations of the nine different states which reach the surface as a function of the applied current in the first solenoid. The initial population (B1=0) is determined by the hexapole transfer probabilities and the state mixing due to the field independent terms of the Hamiltonian.

overall magnetic field the beam is passed through in the first arm, while keeping the second solenoid (B2) current constant at either 0 A or 5 A. The importance of performing the measurements for two different values of B2 will be explained later. The surface temperature during the scans was kept at 165K. The reason for keeping the surface cold and not at room temperature is to improve the reflectivity of the surface, which is higher when the surface is cold and results in a faster measurement time. We discovered that keeping the surface at a temperature of 165 K allows us to keep the surface clean with no evidence of degradation within the duration of the measurement time. In contrast, we noticed a decrease in the surface signal when the surface was below that temperature (135 K) which can probably be related to the adsorption of water molecules from the background pressure, hence we decided to perform all of the magnetic scans at 165 K.

We measured the (-1,0) and (1,0) diffraction channels along the $< 110 >$ direction and the (-1,-1) and (1,1) along the $< 100 >$ direction. The measured signals are plotted in Fig. 4.8 and Fig. 4.9. The significant oscillations we observe shows that the scattered intensity changes (by up to $\pm$ 20%) as we change the quantum state of the molecules arriving at the surface, i.e. the scattering event is very sensitive to the quantum state of the molecules (the rotational projection). This can be in part related to the change in the population of the different states arriving at the surface, but not necessarily. This is because the scattered intensity at the detector is an interference phenomena and changes in the phase of the state arriving at the surface can be just as important as the population differences.

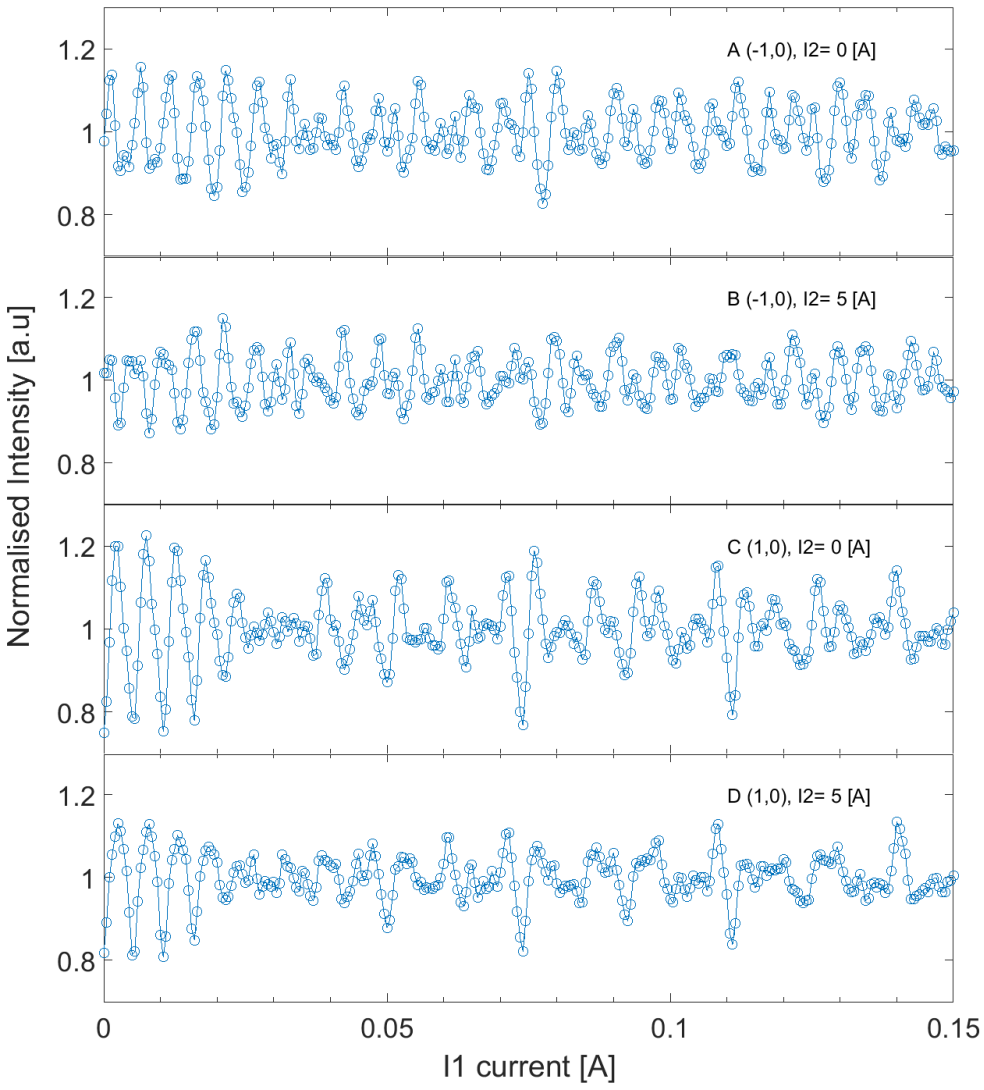

Figure 4.8: Magnetic scans in the $< 110 >$ direction - the panels show results obtained for different currents in the second solenoid and different diffractions channels

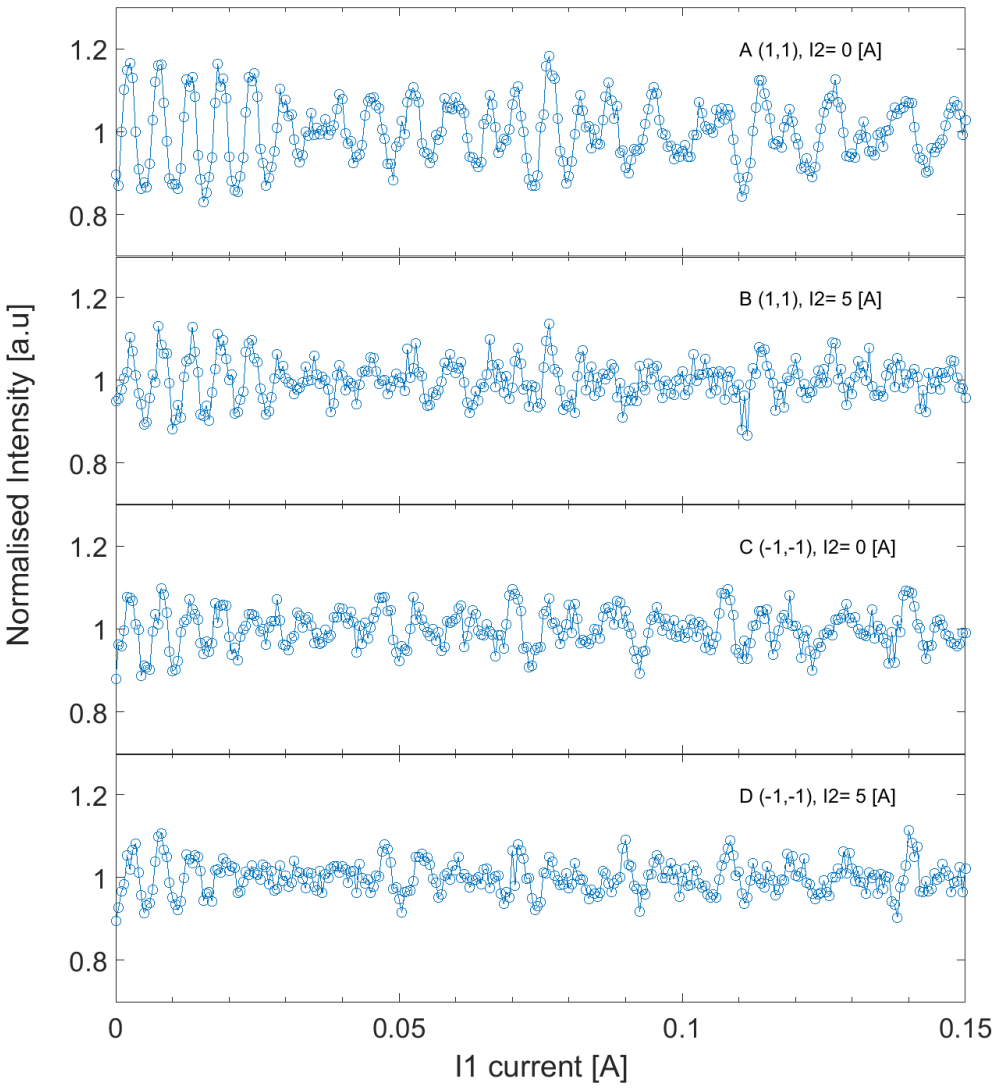

Figure 4.9: Magnetic scans in the $< 100 >$ direction - the panels show results obtained for different currents in the second solenoid and different diffractions channels

4.4 Analysis

As we mentioned earlier in Sec.2.4.2, the well-known properties of the machine (magnetic lens, transmission probabilities and full magnetic profile) allow us to propagate the wavefunction quantum mechanically. The only unknown element required to simulate the measured signal is the state to state scattering matrix, as can be seen in Eq. 2.26. One way of exploiting the experiment to improve our theoretical understanding is to use a theoretically calculated scattering matrix, simulate the signal and compare to the experiment. Unfortunately, we are not aware of a reliable calculation for such a comparison. An alternative approach for analysing the data which we present below is to compare the data to simulations performed with a large number of scattering matrices, and numerically extract the scattering matrix which produces the best fit.

We start by noting that even for the simplest case of $o-H_2$ scattering, without energy exchange with the surface and without changing the overall rotational and nuclear states, the scattering matrix for this case is a 9×9 matrix composed of 81 complex elements, where the square of the magnitude of each element corresponds to the state to state scattering probability. When considering the experiment we are simulating, the mixing of the rotational and nuclear projection (m_I and m_J) which is on the order of micro-seconds (results from the field independent terms in the Hamiltonian, see [3]) is negligible within the very short time (pico-seconds) of the scattering event. Combining this with the fact that the surface (LiF) is a non-magnetic surface and we expect a non-magnetic interaction with the molecule, we can assume that the nuclear spin has no contribution to the scattering event. This results in the ability to use the m_J subspace scattering matrix (a 3×3 matrix) to determine the interaction in the scattering process. The scattering matrix in this case can be written as-

$$\hat{S} = \begin{pmatrix} s_{11}e^{ik_{11}} & s_{10}e^{ik_{10}} & s_{1-1}e^{ik_{1-1}} \\ s_{01}e^{ik_{01}} & s_{00}e^{ik_{00}} & s_{0-1}e^{ik_{0-1}} \\ s_{11}e^{ik_{-11}} & s_{-10}e^{ik_{-10}} & s_{-1-1}e^{ik_{-1-1}} \end{pmatrix} \otimes \mathbb{1}_{3\times 3}, \tag{4.7}$$

where the s_{fn} are the amplitudes for a transition from an initial state n to a final state f and k_{fn} are the associated phases (the scattering matrix elements are complex numbers). The 3x3 matrix written above is then expanded, using a

Kronecker product, into a 9x9 matrix so we can relate it to the wave functions before and after the scattering event.

As the LiF(001) has reflection symmetry along the $< 110 >$ and $< 100 >$ directions, a further simplification can be made and reduce the number of necessary amplitudes in the scattering matrix. The reflection symmetry of the lattice forces the surface potential to not distinguish between molecules rotating clockwise to anti-clockwise meaning that the relative populations of those states should be the same. The reflection symmetry means that the sum of the square amplitudes in the first and third columns should be the same, and as a result the relative populations of the clockwise and anti-clockwise which scatter into the diffraction channel are the same. Also, the sum of square amplitudes in the first and third rows should be the same, meaning that the relative populations in the clockwise and anti-clockwise helicopter states are the same after scattering. Rewriting the simplified scattering matrix gives,

$$\hat{S} = \begin{pmatrix} s_{11}e^{ik_{11}} & s_{10}e^{ik_{10}} & s_{1-1}e^{ik_{1-1}} \\ s_{01}e^{ik_{01}} & s_{00}e^{ik_{00}} & s_{01}e^{ik_{0-1}} \\ s_{11}e^{ik_{1-1}} & s_{10}e^{ik_{-10}} & s_{11}e^{ik_{-1-1}} \end{pmatrix} \otimes \mathbb{1}_{3\times 3}. \tag{4.8}$$

This constrained version of the scattering matrix was used in the fitting procedure. In order to fit the data, we must calculate all of the elements in Eq. 2.26, we rewrite it here,

$$|\Psi_3(f, B_2, B_1, n)\rangle = \sqrt{p_f}\hat{U}(B_2)R(\theta_2)\hat{S}R(\theta_1)\hat{U}(B_1)\sqrt{p_n}\,|n\rangle\,, \tag{4.9}$$

$$DS = \sum_v p_v \sum_f \sum_n \langle\Psi_3(f, v, B_2, B_1, n)|\Psi_3(f, v, B_2, B_1, n)\rangle\,. \tag{4.10}$$

As discussed above, the only element we can not calculate is the scattering matrix, the evolution operators $\hat{U}(B_1)$ and $\hat{U}(B_2)$ are calculated for the magnetic fields used in the experiment and for a range of the velocities in the molecular beam that contribute to the signal. Together with the transmission probabilities through the first and second hexapoles and the proper rotations which correspond to the surface position we can calculate a signal for a given scattering matrix. When analysing our signal, there is an unknown component of constant background to the measured signal, i.e. intensity which is related to

the molecular beam but does not oscillate when we change the B1 values. The physical processes leading to this constant background are described later in this chapter. Unfortunately we have no way of quantitatively calculating this constant background, and setting it as a free parameter leads to a loss of uniqueness of the scattering matrix we can fit the experimental result. To overcome the background component in the experimental signal, we perform magnetic scans of the first arm with two different values of current in the second arm (0 A and 5 A), where we expect the background to be the same in both measurements. The experimental signals are fitted simultaneously so that a single scattering matrix can describe them both. The difference between the signals and the calculations is minimised using the downhill simplex method of Nedler and Mead[33] with the addition of simulated annealing so that the algorithm is able to reach what seems to be a global minimum.

4.4.1 Fitting results

Tables 4.1 and 4.2 show the average values of the scattering matrix gathered from the best 30 fits to the experimental data for the $< 110 >$ and $< 100 >$ diffraction peaks respectively.

< 110 >					
Parameter	(1,0) peak	(-1,0) peak	Parameter	(1,0) peak	(-1,0) peak
s_{11}/s_{1-1}	0.4	0.2	$k_{11} - k_{1-1}$	0	1.4
s_{10}/s_{1-1}	0.8	0.7	$k_{10} - k_{1-1}$	0.8	1.9
s_{1-1}/s_{1-1}	1	1	$k_{1-1} - k_{1-1}$	0	0
s_{01}/s_{1-1}	0.3	0.6	$k_{01} - k_{1-1}$	5.6	4.2
s_{00}/s_{1-1}	0.5	0.2	$k_{00} - k_{1-1}$	6	0.9
s_{0-1}/s_{1-1}	0.3	0.6	$k_{0-1} - k_{1-1}$	3.3	0.9
s_{-11}/s_{1-1}	1	1	$k_{-11} - k_{1-1}$	1.7	5.1
s_{-10}/s_{1-1}	0.8	0.7	$k_{-10} - k_{1-1}$	0	0.1
s_{-1-1}/s_{1-1}	0.4	0.2	$k_{-1-1} - k_{1-1}$	2.2	5.6

Table 4.1: The relative values of the amplitudes (s_{fn}) and phases (k_{fn}) of the S matrix elements from the best fits for H_2 scattering from LiF into the (1,0) and (-1,0) diffraction peaks. These values are averaged over the 30 fits which give the lowest fitting error. The estimated uncertainty in these values is estimated as 10%.

< 100 >					
Parameter	(1,1) peak	(-1,-1) peak	Parameter	(1,1) peak	(-1,-1) peak
s_{11}/s_{1-1}	0.2	0.5	$k_{11} - k_{1-1}$	2	1.3
s_{10}/s_{1-1}	0.8	0.6	$k_{10} - k_{1-1}$	2.7	0.6
s_{1-1}/s_{1-1}	1	1	$k_{1-1} - k_{1-1}$	0	0
s_{01}/s_{1-1}	0.5	0.5	$k_{01} - k_{1-1}$	3.7	3.4
s_{00}/s_{1-1}	0.6	0.2	$k_{00} - k_{1-1}$	2.5	3.3
s_{0-1}/s_{1-1}	0.5	0.5	$k_{0-1} - k_{1-1}$	1.6	1.9
s_{-11}/s_{1-1}	1	1	$k_{-11} - k_{1-1}$	2.3	5
s_{-10}/s_{1-1}	0.8	0.6	$k_{-10} - k_{1-1}$	4.4	4.9
s_{-1-1}/s_{1-1}	0.2	0.5	$k_{-1-1} - k_{1-1}$	3.3	2.2

Table 4.2: The relative values of the amplitudes (s_{fn}) and phases (k_{fn}) of the S matrix elements from the best fits for H_2 scattering from LiF into the (1,1) and (-1,-1) diffraction peaks. These values are averaged over the 30 fits which give the lowest fitting error. The estimated uncertainty in these values is estimated as 10%.

The reason we average (over the scattering matrix values from the best 30 fits) is because all of the 30 fits we average produce very similar errors, the differences between them are not considered as significant and are attributed to the noise in the measured signal. The values extracted from simultaneous fits of both sets of data (0 A and 5 A in the second coil) for each diffraction peak. Fig. 4.10 shows the simulated signal (dashed line) together with the measured signal (solid line) for the case of (-1,0) diffraction (panels A and B) and for (1,0) diffraction peak (panels C and D). Fig. 4.11 shows the simulated signal (dashed line) together with the measured signal (solid line) for the case of (-1,-1) diffraction peak (panels A and B) and for (1,1) diffraction peak (panels C and D).

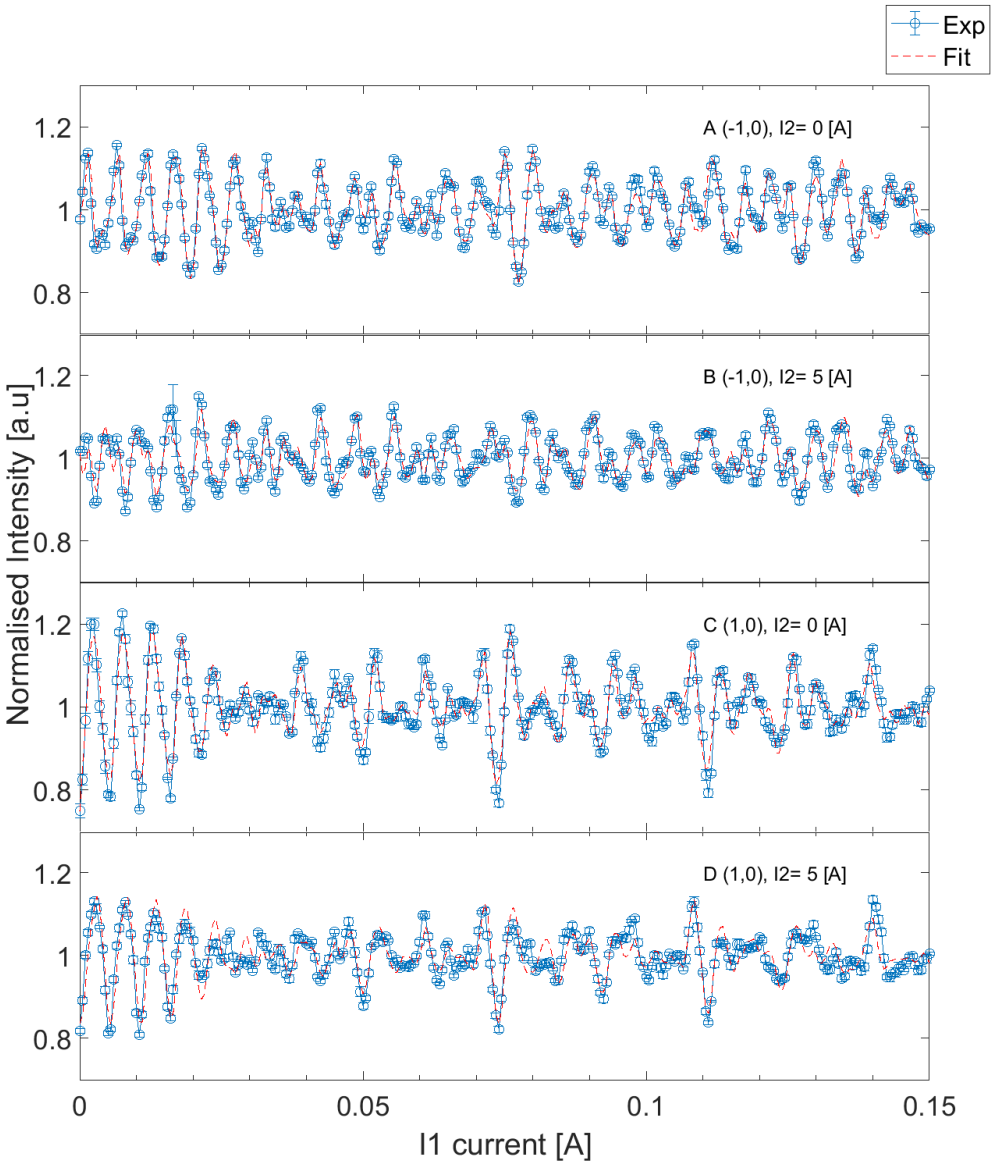

Figure 4.10: Fit results $< 110 >$ - comparison of the simulated signal, resulting from the best fit to the measured signals

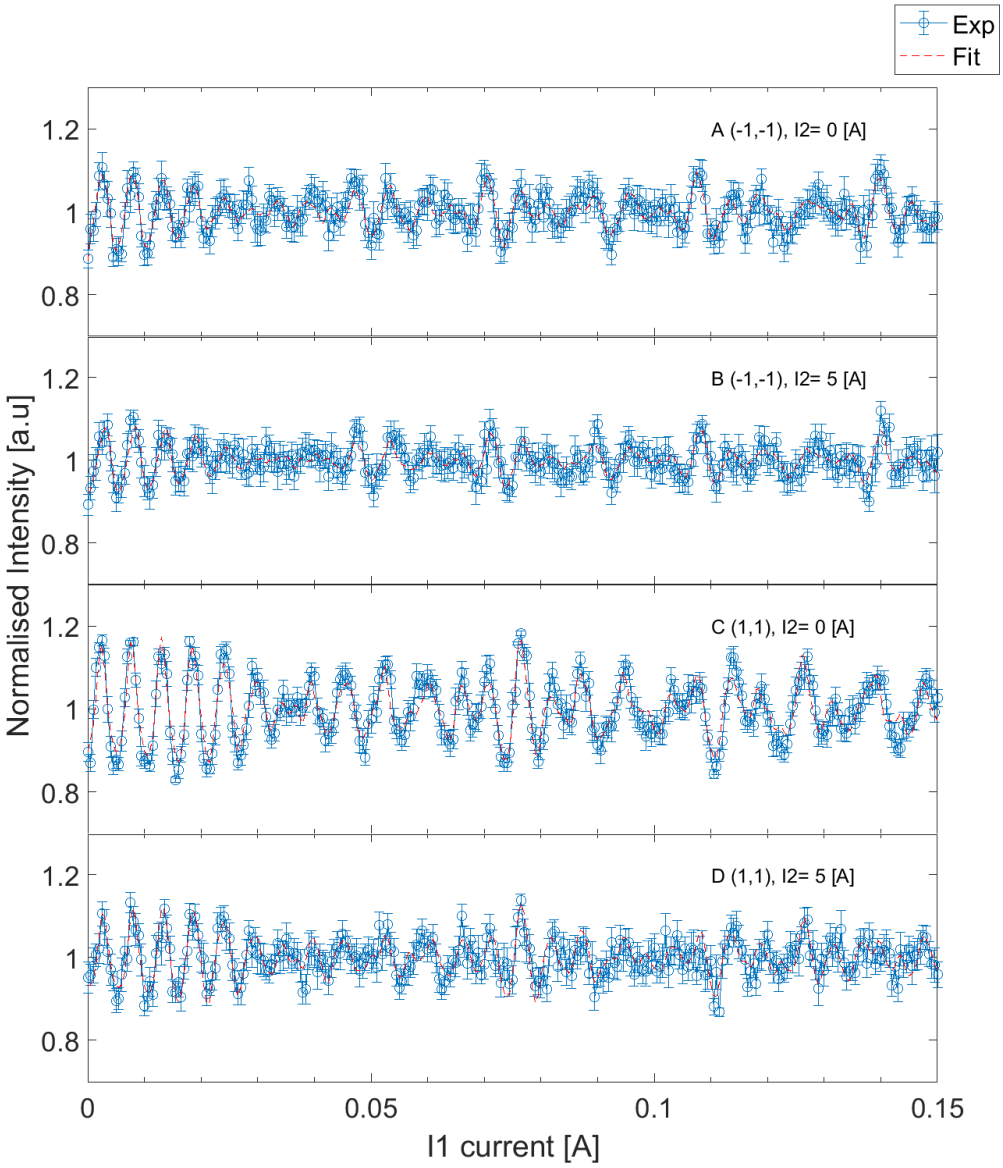

Figure 4.11: Fit results $< 100 >$ - comparison of the simulated signal, resulting from the best fit to the measured signals

4.4.2 Convergence and reproducibility

As can be seen in Fig. 4.10 and 4.11, the fitting procedure we used is capable of fitting the two sets of data (I2=0 A and 5 A) very well using one scattering matrix for each diffraction channel. However, given the large number of free parameters question arise about the significance of the extracted best fitted values. In particular how converged is the result and does it indicate a local minimum or a global minimum; i.e., is the extracted matrix unique?

To ensure convergence of the diffraction peaks empirically determined S-matrix, 150 signal fits were run for each diffraction peak set of measurements, using randomly sampled initial values of all the amplitudes s_{fn}, and phases k_{fn}. The fits were then reduced to the best 30 ones, which give the smallest error when comparing it to the measured signal. The best 30 fits fall within an approximately 10% wide interval of the scattering matrices elements, indicating that the algorithm converges into a group of very similar scattering matrices. Note the fact that the experimental setup is not capable of measuring the absolute flux that scattered into a diffraction channel, nor is the incoming flux known in absolute terms. As a result, the scattering matrices we compare with the signal provide the relative values of the amplitudes and phases of the scattering matrix elements, rather than their absolute values. In practice both the measured signal and the simulated signal are divided by their mean value, making the comparison meaningful. Fig. 4.12 to 4.15 shows histogram bins of the scattering matrix amplitudes and phases.

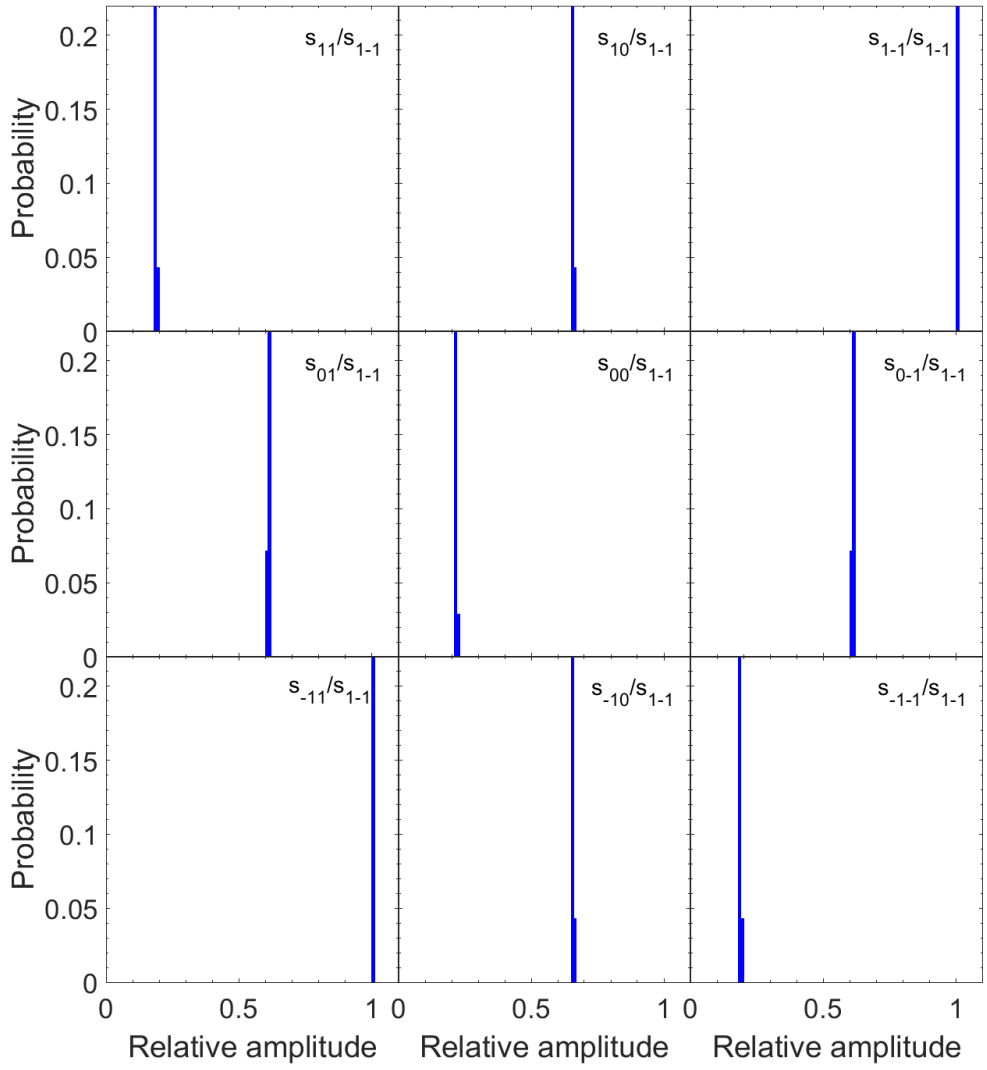

Figure 4.12: Convergence of the empirical S-matrix amplitudes - The values of the S-matrix amplitudes (normalised to s_{1-1}) obtained from the best 30 of 150 fits of the (-1,0) diffraction peak. The distributions are narrow, demonstrating the convergence of the 15 parameter fits, and a relatively small uncertainty in the extracted value.

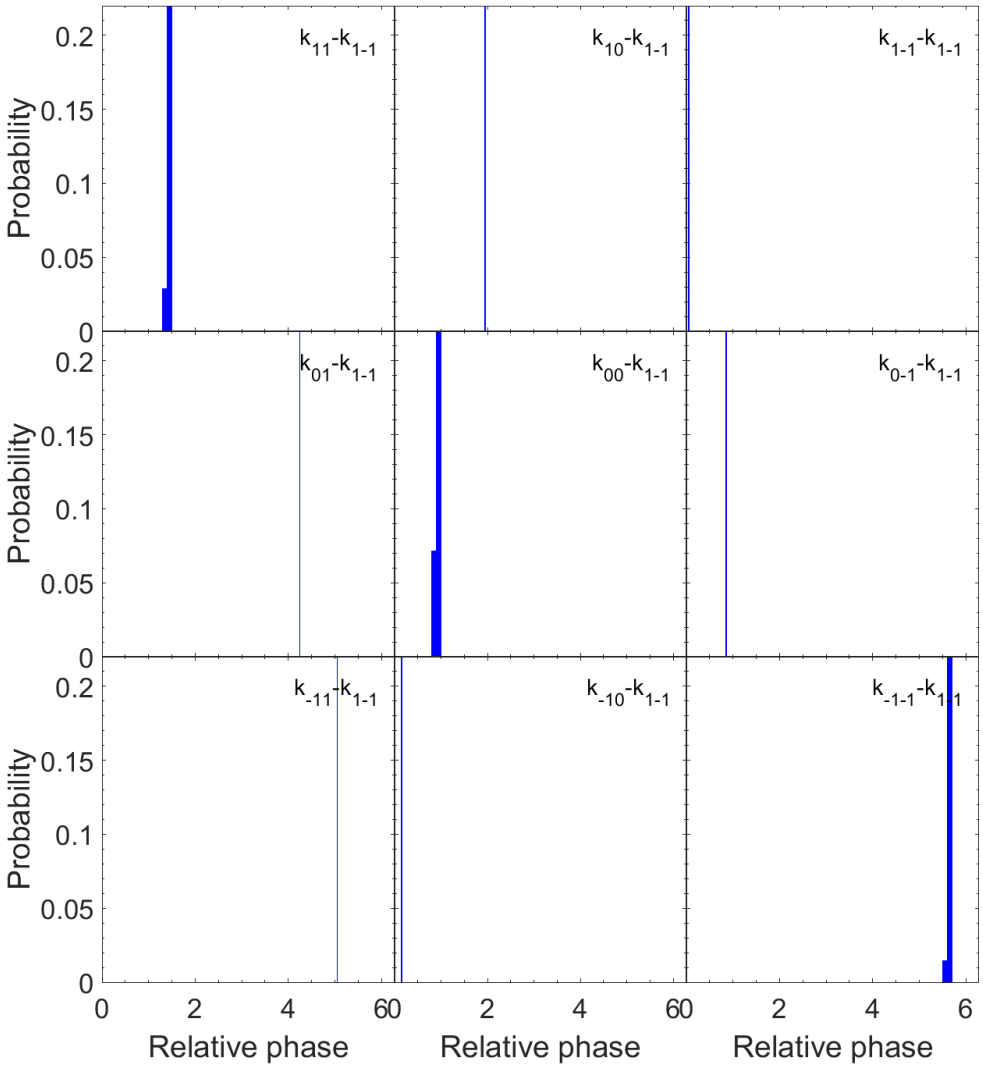

Figure 4.13: Convergence of the empirical S-matrix phases - The values of the S-matrix phases (relative to s_{1-1}) obtained from the best 30 of 150 fits of the (-1,0) diffraction peak. The distributions are narrow, demonstrating the convergence of the 15 parameter fits, and a relatively small uncertainty in the extracted value.

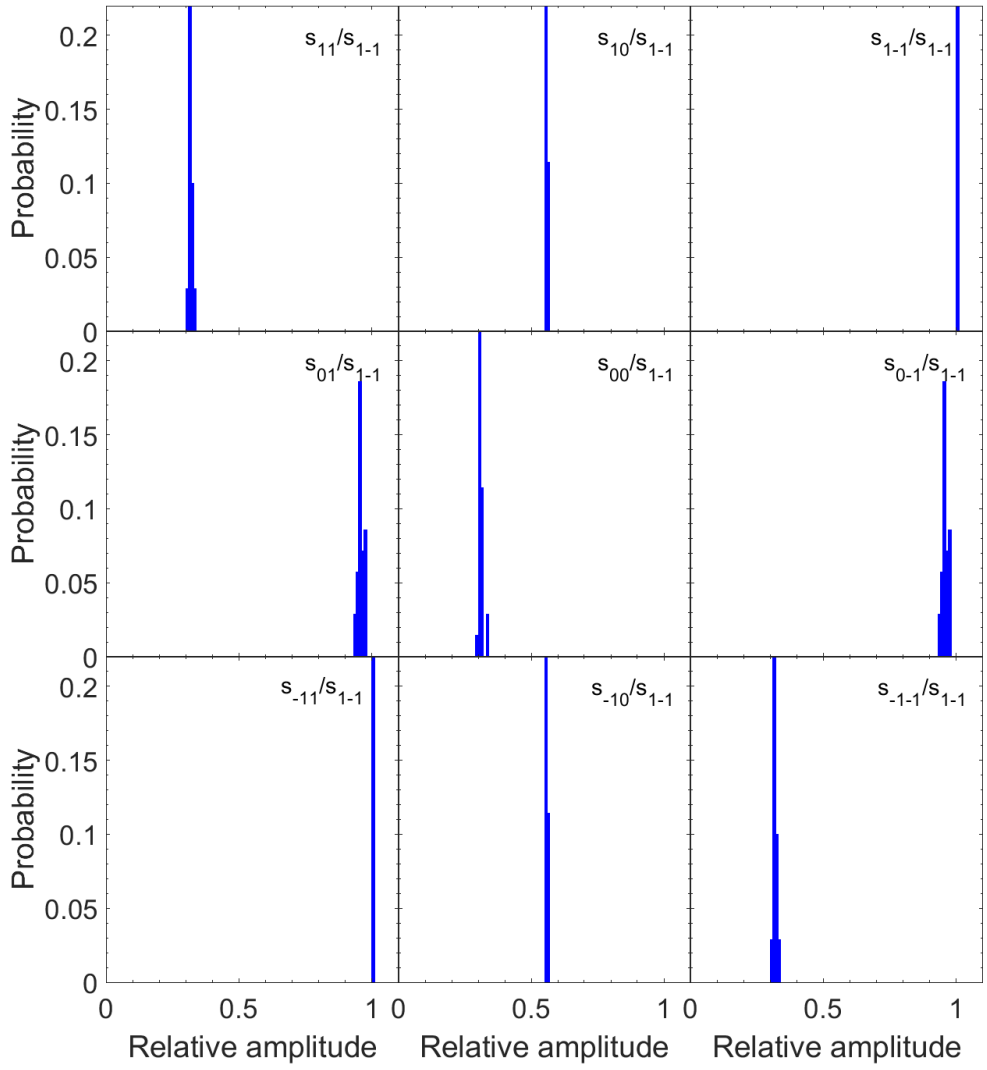

Figure 4.14: Convergence of the empirical S-matrix amplitudes - The values of the S-matrix amplitudes (normalised to s_{1-1}) obtained from the best 30 of 150 fits of the (-1,-1) diffraction peak. The distributions are narrow, demonstrating the convergence of the 15 parameter fits, and a relatively small uncertainty in the extracted value.

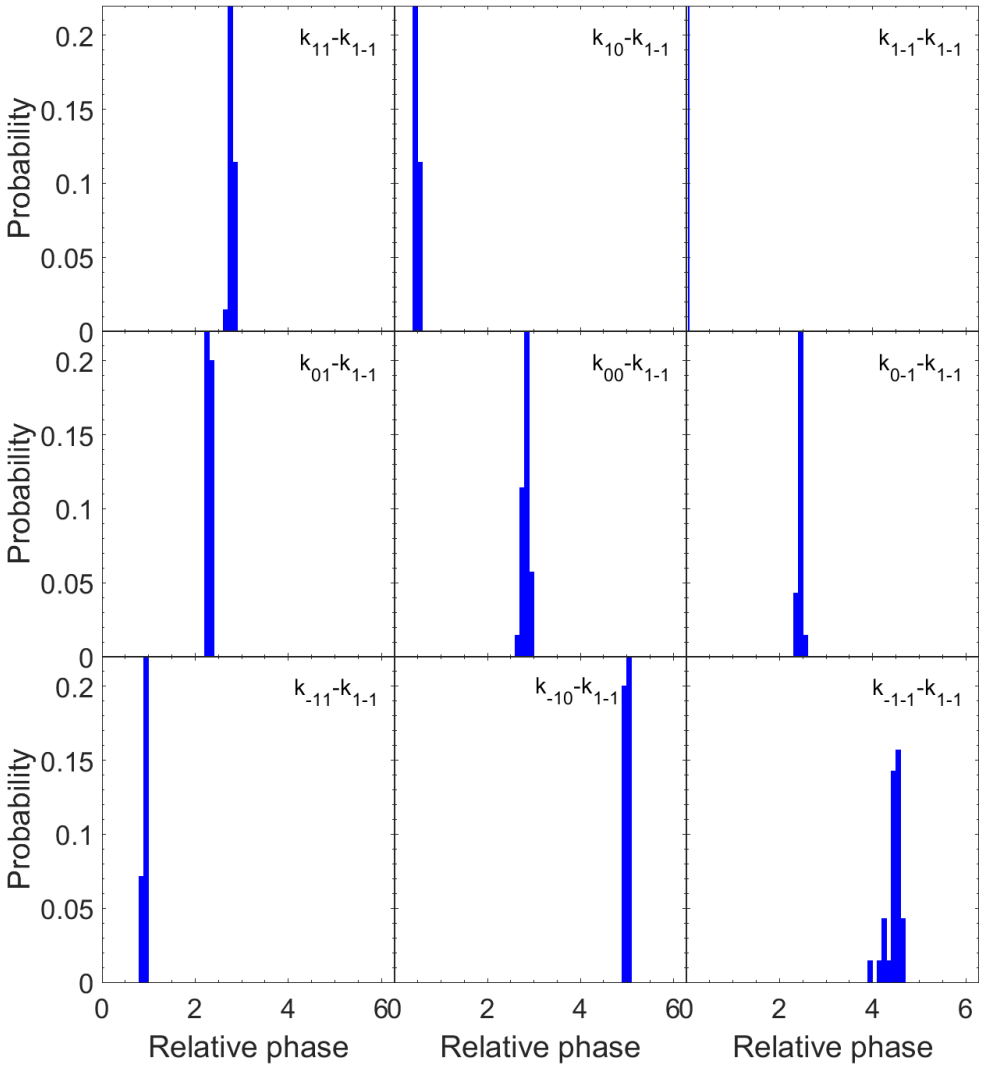

Figure 4.15: Convergence of the empirical S-matrix phases - The values of the S-matrix phases (relative to s_{1-1}) obtained from the best 30 of 150 fits of the (-1,-1) diffraction peak. The distributions are narrow, demonstrating the convergence of the 15 parameter fits, and a relatively small uncertainty in the extracted value.

While the results for the empirical scattering matrices show that the analysis is capable of converging on a single scattering matrix, this does not necessarily mean it is the real scattering matrix, describing the interaction of the molecule and the surface. To enhance our confidence in the significance of the fitting values we can can test the fitting procedure further by means of simulated signal that is generated by an arbitrary scattering matrix. The simulated data are analysed in the same manner as the experimental data, and the results can tell us if the fitting procedure is able to extract the values of the arbitrary scattering matrix we generated the signal with. We added noise to the simulated data to be consistent with the noise in the experimental signals. The S-matrix amplitudes from the best fits are presented in Fig. 4.16 and the phases in Fig. 4.17 with the black dashed lines in each panel showing the value of the parameter used to simulate the data. The simulated data and the best fits for the simulated data are presented in Fig. 4.18 for the cases of 0 A (A) and 5 A (B) amps in the second solenoid.

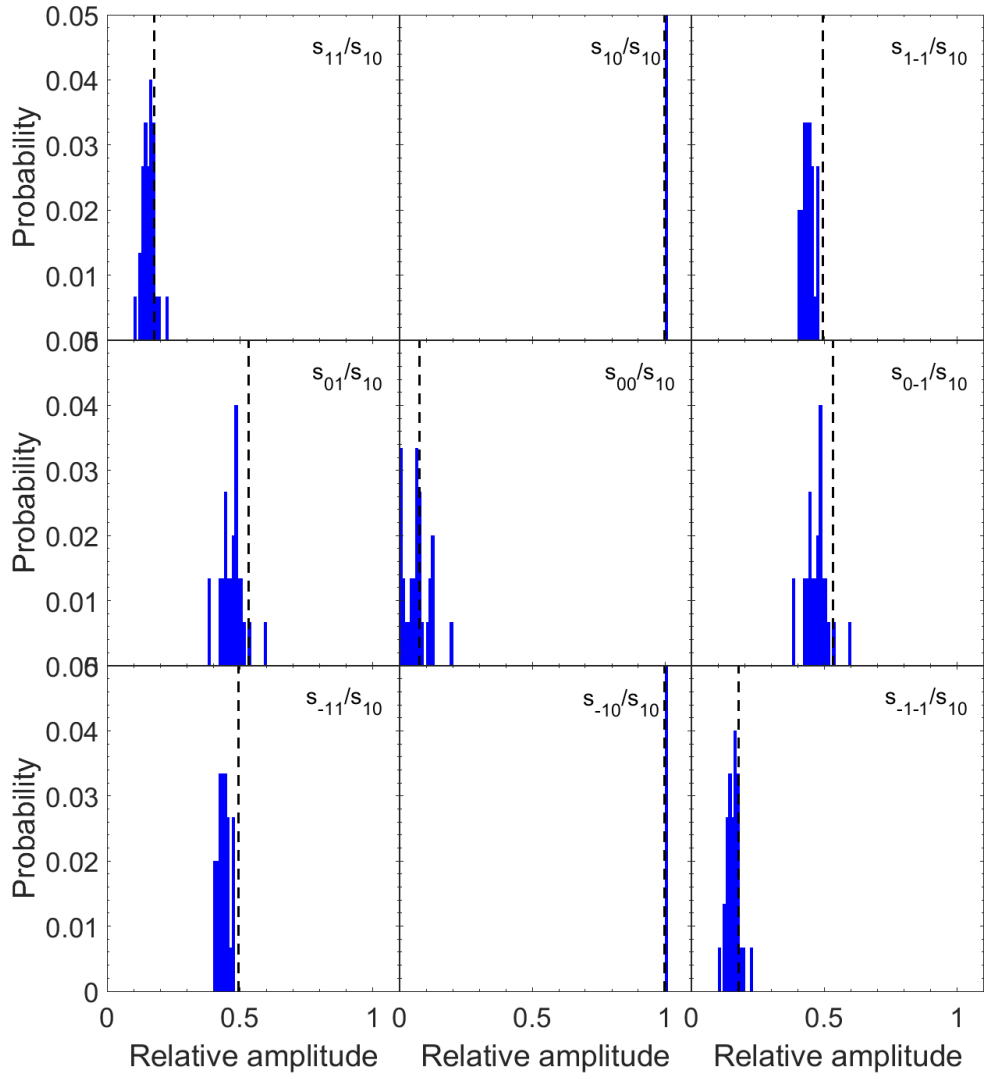

Figure 4.16: Convergence of the S-matrix amplitudes - The values of the S-matrix amplitudes (normalised to s_{10}) obtained from the best 30 of 150 fits of the simulated data. The black dashed line in each panel shows the value of the parameter that was used to produce the simulated data

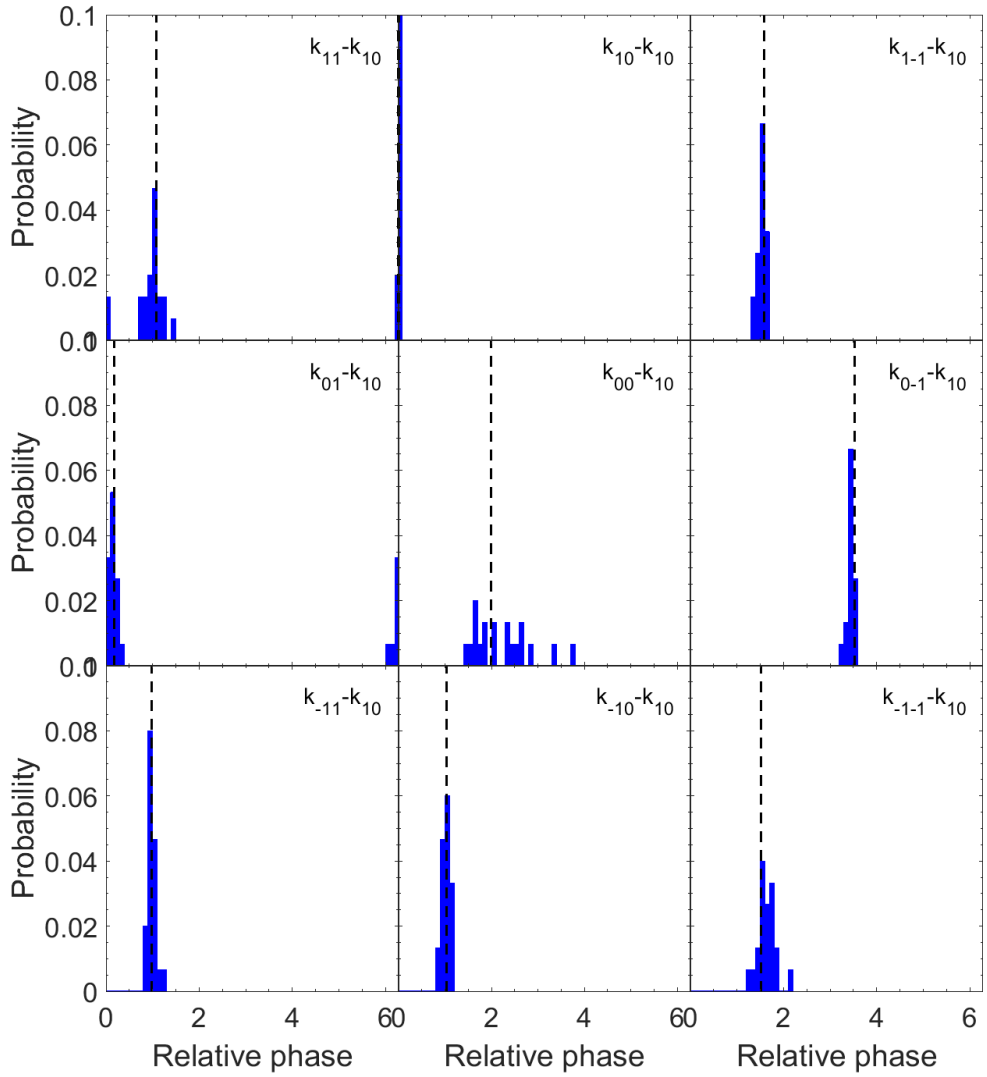

Figure 4.17: Convergence of the S-matrix phases - The values of the S-matrix phases (relative to k_{10}) obtained from the best 30 of 150 fits of the simulated data.the black dashed line in each panel shows the value of the parameter that was used to produce the simulated data. Note that the relatively wide distribution of relative phases obtained for $k_{00} - k_{10}$ coincided with a relatively small amplitude which reduces the sensitivity of the fit to the phase of this element

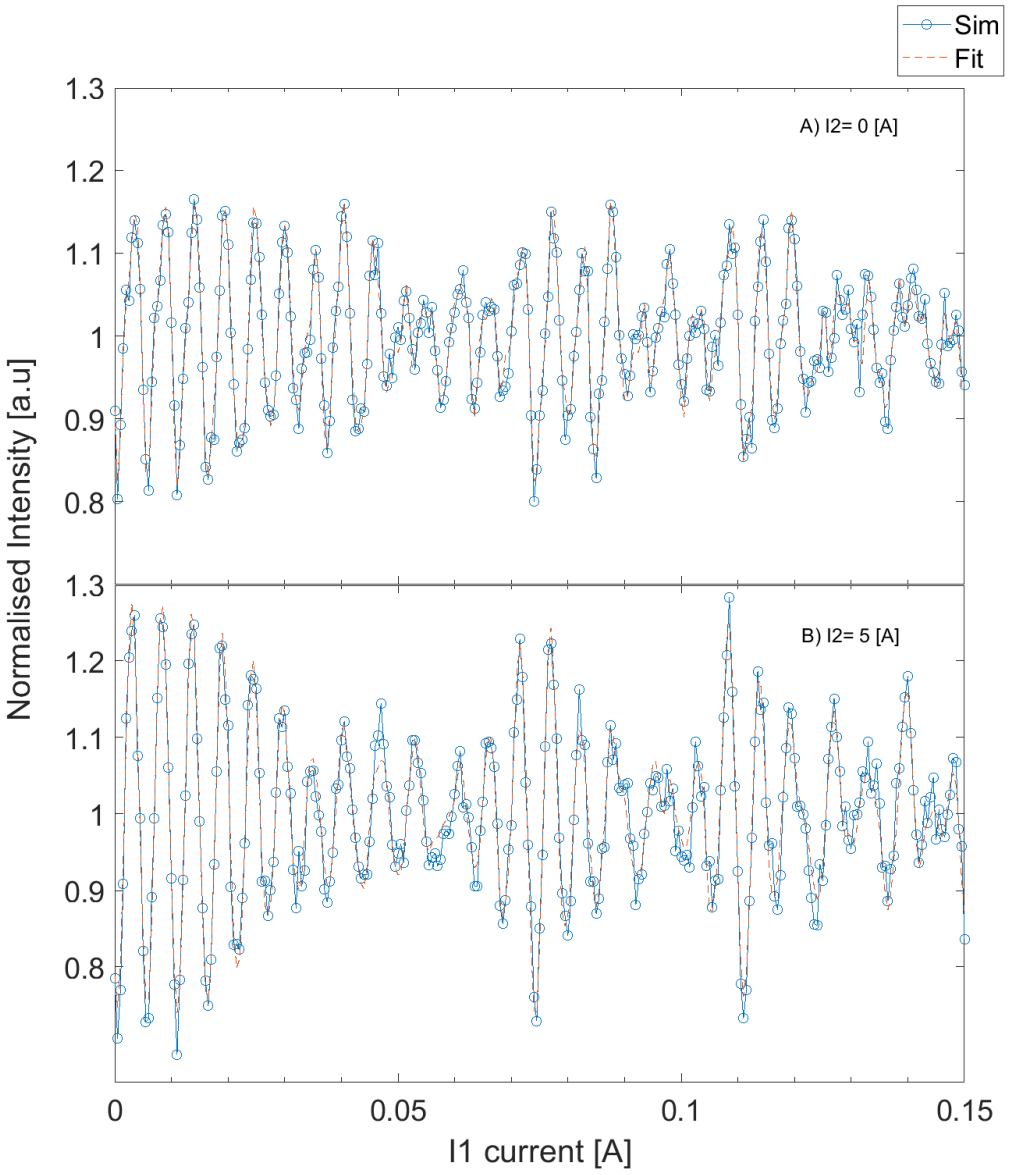

Figure 4.18: Fits to simulated data - the best fits (red dashed line) to simulated data (blue line) for values of I2=0 Amp (A) and I2=5 Amp (B)

As can be seen from the histogram plots, the fitting procedure converges at the initial parameters used to simulate the data. The average values of the parameters obtained from the best 30 fits with the lowest error gives values that are within 10% of the initial values suggested that the noise in the experimental data is small enough and allows an extraction of an empirical scattering matrix from the data.

There are several sources of systematic error in the analysis procedure which can affect the accuracy of the empirical extracted scattering matrix. The first is the accuracy of the measured magnetic field profile in the first and second arms of the machine. The profiles have been measured by a high precision Gaussmeter (Alphalab inc. VGM model) that is accurate to $\pm 0.02\,\mathrm{G}$ and a 2% of the reading. The fitting procedure was repeated by using magnetic profiles which include the maximum error and uncertainties to check how they affect the analysis. The fits which used the slightly different magnetic profiles, that are consistent with our uncertainty in their measurement, change the empirical scattering matrix values by a few percent, but do not affect the overall conclusions. An additional uncertainty related to the magnetic field profiles is the conversion from the current passed through the first and second solenoid and their corresponding magnetic fields. This has been determined by applying a known current in the solenoids and measuring the magnetic field profiles inside them. The resulting magnetic field profiles were integrated so that a conversion between the applied current and the magnetic field can be extracted by dividing the integral by the applied field. This results in an effective conversion factor, from current to magnetic field, in any of the solenoids. These conversion factors were applied to each of the current values used in the experiment. The accuracy of this calibration is demonstrated by the fact that both the calculated and simulated signal have the same oscillation frequencies. During the measurement process we use a beam flag to measure the detector H_2 background and then subtract it from the measured signal, but still there is another unknown background component in the beam. This is due to both para-hydrogen molecules which are not subject to our magnetic manipulation and a fraction of the ortho-hydrogen molecules that are not coherently controlled by the magnetic fields of the solenoids (for example molecules which

do not perfectly follow the adiabatic / non-adiabatic transitions mentioned earlier). As we briefly mentioned above, to assess and separate the background from the signal, we fit two signals simultaneously for different current in the second solenoid. As any mechanism that produces the background should be independent of the current in the second solenoid, we expect the background to be the same in those measurements as they were conducted under the same conditions. The fitting procedure looks for a single background component that could match the signal to the calculation in the case of both measurements. Without determining the background, it is not possible to extract a unique scattering matrix as different values of the scattering matrix can be found with different backgrounds that give equally good fits to the data.

Another source of error in our analysis can be related to the fact that we are not performing a measurement at single beam energy. The scattered beam is composed out of a range of velocities with the mean velocity corresponding to the location of the maximum of the diffraction peak. In theory, each velocity (energy) should be given a scattering matrix of its own, but then extracting multiple matrices from the data would not be possible. To minimise the effect of the velocity spread, we performed our current scans on non-specular diffraction peaks. This leads to a very narrow velocity distribution contributing to the signal. In the presented measurements, the velocity distribution FWHM is estimated as 0.5% and the good agreement between the calculations and measurements suggested that using a single scattering matrix for this kind of velocity spread is reasonable.

4.5 Discussion and Conclusions

The sum of the square amplitudes of the rows of the scattering matrix corresponds to the state-to-state scattering probabilities of the rotational states after scattering, regardless of their initial states. Similarly, the sum of the square amplitudes of the columns of the scattering matrix correspond to the state-to-state scattering probabilities of the rotational states before scattering regardless of the final states of the molecules. We can gain information about the stereodynamic

effects by calculating the ratio between the cartwheel and helicopter rotational states before and after scattering,

$$\left(\frac{m_J=0}{m_J=1}\right)_{before} = \frac{s_{10}^2 + s_{00}^2 + s_{-10}^2}{s_{11}^2 + s_{01}^2 + s_{-11}^2}, \tag{4.11}$$

$$\left(\frac{m_J=0}{m_J=1}\right)_{after} = \frac{s_{01}^2 + s_{00}^2 + s_{0-1}^2}{s_{11}^2 + s_{10}^2 + s_{1-1}^2}. \tag{4.12}$$

Table 4.3 shows the stereodynamic parameters resulting from the scattering matrices fitting procedure. These parameters can be used to get a better understanding on how the LiF surface rotationally polarises the scattered H_2 beam. By looking at the relative population after scattering we can say that in all mea-

	(1,0)	(-1,0)	(1,1)	(-1,-1)
$\left(\frac{m_J=0}{m_J=1}\right)_{before}$	1.2	0.5	0.8	1.4
$\left(\frac{m_J=0}{m_J=1}\right)_{after}$	0.2	0.6	0.8	0.3

Table 4.3: Streodynamic effects of the different diffraction channels before and after scattering

sured diffraction channels, the amount of helicopter state molecules are higher than cartwheel state molecules. A consequence of this finding is that scattering from a LiF surface can be used as a polarizing mirror, i.e. it can enhance the population of cartwheel molecules in a general molecular beam setup which does not have any magnetic manipulation capabilities. Some of the diffraction peaks ((1,0) and (-1,-1)) will do a better job than others in polarizing the beam. As currently the only way of controlling the rotational projection states of ground state hydrogen molecules is using the complex MMI setup we developed, the idea of a cheap simple polarizing element which can be added to other molecular beam setups can be attractive for other fields. For example, experimental setups which are used to study reactive sticking of hydrogen on various surfaces could measure the sticking probabilities for beams with different rotational orientation by first scattering the beam from a LiF crystal. Note, that if the molecular beam velocity / scattering conditions are changed, MMI measurements of the type presented in this chapter will have to be performed to determine the relevant S matrix.

Another conclusion from our analysis regards rotation projection flips (Δm_J). Previous work on H_2 scattering from LiF, suggested a $\Delta m_J = 0$ propensity rule [47, 48] which means that a collision with LiF surface cannot change the rotational projection of a H_2 molecule. The extracted scattering matrices off-diagonal elements (which corresponds to $\Delta m_J \neq 0$) are not zero, in fact they are of the same order of magnitude as the diagonal elements (which correspond to $\Delta m_J = 0$), illustrating the breaking of this propensity rule. Our finding supports a previous theoretical prediction for the same system (H_2/LiF) using a simplistic model which takes the quadrupole interaction of the hydrogen molecules and the surface ions into account [45]. Furthermore, the interpretation of Knudsen flow experiments for H_2 on LiF used the $\Delta m_J \neq 0$ collisions in order to explain their results [49, 50]. Recent calculation have shown that the rotational projection transitions like the ones we can extract directly from experiments, are closely linked to reactive adsorption events and also relevant for the atomistic understanding of heterogeneous catalysis [51].

The collisions of gas phase molecules with surfaces have also previously been demonstrated to create rotational polarisation in scattered molecules, with an Ag(111) surface shown to create rotational alignment in scattered NO [52], and both rotational alignment and orientation in scattered N_2[53, 54]. In both cases, strong negative alignments were measured in rotationally inelastic scattering. This corresponds to collisions that change the rotational angular momentum, J, but tend to conserve m_J. In contrast, in our current study the rotational alignments of the H_2 molecules scattering from the surface are for rotationally elastic scattered molecules, which means that the total rotational angular momentum remains the same ($\Delta J = 0$) and the polarisation is due to the changes in the m_J projection from the scattering event. The observation of differences in the scattering probabilities of different rotational orientations of the H_2 molecules, could perhaps be related to the different potential energy surfaces seen by the different m_J state molecules, with molecules rotated as helicopter states ($m_J = \pm 1$) experiencing a more corrugated potential than the molecules rotated as cartwheel state ($m_J = 0$) [45]. The initial rotational orientation of molecules has also been shown to change how molecules interact with a surface in previous studies which have used collision induced rotational polarisation in molecular beam expansions

[55], paramagnetic molecule deflection [56] and vibration excitation [20] molecules to prepare molecules with an anisotropic distribution of m_J states before the gas-surface collision. The fact that the experimental method we used does not alter the molecular ground state, allows us to study how the initial quantum population of rotational orientation states in the beam can change the probability of scattering into a particular diffraction channel regardless of the final state. In the case of the the $< 110 >$ direction, the relative scattering probabilities of molecules that are in $m_J = \pm 1$ states is less than those that are in the $m_J = 0$ state, when the scattering is from the (1,0) channels. This means that molecules that are rotating like helicopters are less likely to scatter into the (1,0) diffraction channel than molecules rotating like cartwheels. The opposite situation occurs when scattering from the (-1,0) diffraction peak, where molecules in the $m_J = \pm 1$ states are more likely to scatter into that diffraction channel than molecules in the $m_J = 0$ state. Along the $< 100 >$ direction, the (-1,-1) channel is more likely to scatter cartwheel molecules and the (1,1) is more likely to scatter helicopter molecules. The fact that the different diffraction channels are sensitive to the initial orientation of the impinging molecules suggest that LiF surface can potentially also be used as a rotational orientation analyser, i.e. the relative intensity of the diffraction peaks can be used to deduce the rotational populations in a molecular beam. Finally, the scattering matrices we were able to extract in this chapter can be used as sensitive benchmarks for theoretical development. If a calculation will manage to reproduce the scattering matrices we extracted from our measurements, it is likely that its description of the molecule-surface potential can be trusted and used to calculate other properties of the surface (for example, reaction probabilities).

5

H_2/Graphene

In this chapter we use the same interferometry technique described in Chapter 4 to investigate the dependence of specular scattering of H_2 from a graphene covered surface on the rotational projection state of the scattered molecules. The rotational projection states are coherently controlled before and after scattering, and the results are compared to calculations and to similar measurements performed on other surfaces.

The motivation for performing rotationally controlled scattering experiments of H_2 from graphene, is to support the development of an accurate theoretical description of the interaction of H_2 with graphene. One example for the importance of this interaction is the development of graphene electrodes in hydrogen fuel cell technology [57]. Providing a benchmark for the H_2/graphene surface potential in terms of a measured scattering matrix could be a crucial mile stone in the process of describing the interaction between H_2 and graphene surfaces. Furthermore, as we already had results from a bare Cu(111) surface, we thought it will be interesting to compare between the two. We tried to measure diffraction peaks scattering on graphene grown on Cu(111). While we could notice diffraction peaks with ^4He beam, we were not able to detect any of them with H_2 beam. As a consequence, we decided to investigate the specular scattering of this system.

5.1 Experimental technique

5.1.1 Sample preparation

The samples were grown by the group of Prof. Daniel Farias in Madrid and shipped to us in a sealed container. The graphene layer was grown on a thin (500 nm) Cu(111) film, which was deposited on a C-plane sapphire crystal. Helium atom scattering (HAS) characterization, performed by Dr. Amjad Al Taleb (Madrid) on samples grown using the same methods, showed a diffraction peak pattern that suggests the sample is dominated by two orientation domains (illustrated in Fig. 5.1), rotated by 30 ° from each other (see [58] for more details). The

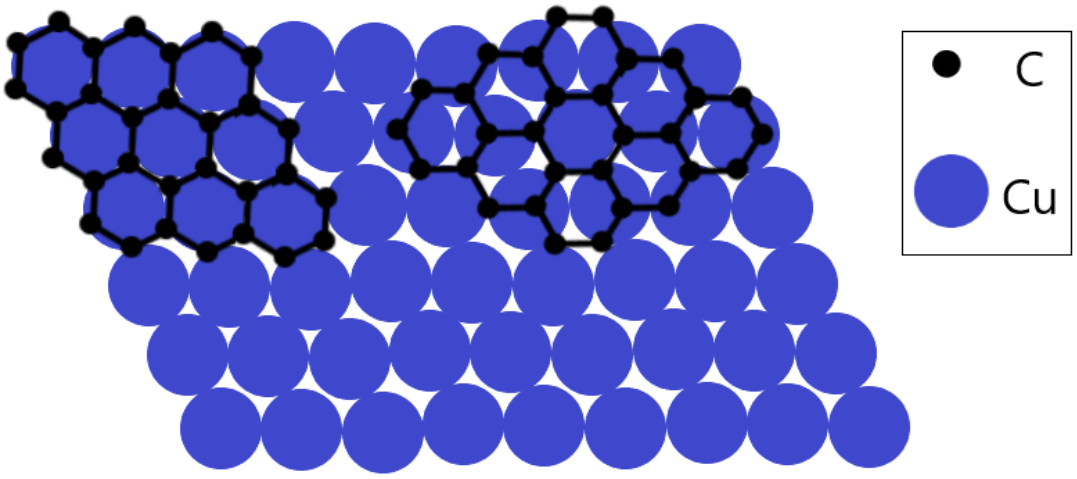

Figure 5.1: Graphene on a Cu(111) surface - with the two dominated domains rotated by 30 ° from each other

sample was mounted on a tantalum base that is connected to the sample holder, with T type thermocouple for temperature reading and temperature control capabilities from 40 K to 900 K. The surface was cooled using a compressed helium cryostat (Stinger, ColdEdge Technologies) and for heating we used a tungsten filament combined with high voltage electron bombardment.

5.1.2 Experimental setup

Measurements were performed using the magnetic molecular interferometer (MMI) described in detail in section 2.1. The system contains a source for expanding a supersonic molecular beam from a nozzle followed by a skimmer, a magnetic lens to focus the beam into a parallel configuration, a magnetic solenoid which creates a homogenous magnetic field up to 1000 G, a scattering chamber with a base pressure in the 10^{-11} mbar range and a 6-axis sample manipulator allowing the surface to be positioned in the centre of the chamber and control the tilt, azimuth and the polar angles of the surface. The chamber also includes a LEED and AES instrument (OCI Vacuum Microengineering). Upon exiting the scattering chamber, we have another magnetic solenoid, followed by a magnetic lens to focus the beam to a spot in the detector region. The experimental apparatus is the same as the one described in detail in the previous chapter with the addition of the LEED and the Helium cryostat.

5.2 Result and discussion

We received two samples to study (referred to as sample A and B), the samples were mounted and inserted into the vacuum chamber after being exposed to ambient conditions. Heating the samples to 500 K, made the LEED pattern of the Cu(111) visible, as the electrons are also sensitive to the bottom layer (the Cu foil). Further annealing to 900 K in the presence of C_2H_4 , a treatment suggested by the Madrid group, was used to further clean the surface from adsorbate (possibly by removing oxygen from the copper surface without damaging the graphene layer). Fig. 5.2 shows the evolution of the LEED images for the case of of sample A. The image shown in 1 is after the 500 K flash, and 2,3,4 were measured after consecutive treatments at 900 K. The diffraction spots become more resolved in comparison with the background intensity, further treatment cycles did not improve the LEED pattern. A comparison of LEED images from the two samples after using the cleaning methods described above are presented in Fig. 5.3. The LEED patterns of the two samples were measured using a beam energy of 128 eV. As can be noticed in the pattern shown on the right measured from sample B,

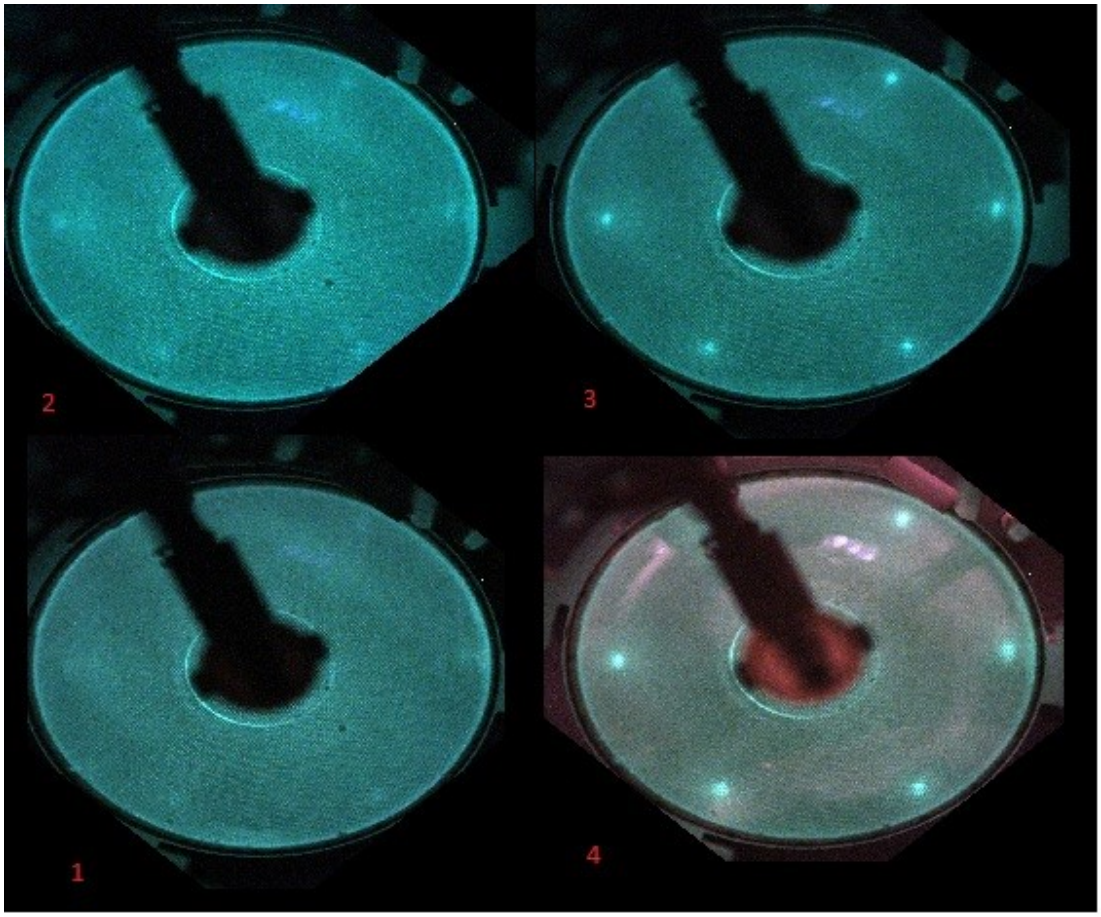

Figure 5.2: Evolution of the LEED pattern during sample cleaning - 1) flashing sample A to 500 K, 2-4) consecutive heating to 900 K in the presence of C_2H_4. The energy of the electrons is 128 eV and surface temperature at 120 K.

instead of a simple six-fold spot pattern, we see what looks like splitting into two less resolved spots connected by a short arc, which might suggest more than one Cu domain. Further cleaning treatment of sample B did not improve the LEED pattern. As the spots match the 6-fold pattern we expect from Cu(111) we relate this result to the variable quality of the thin copper film. The fact that the pattern is of the Cu(111) layer rather than the graphene surface layer can be expected as electron penetration is expected at this electron energy (128 eV). In

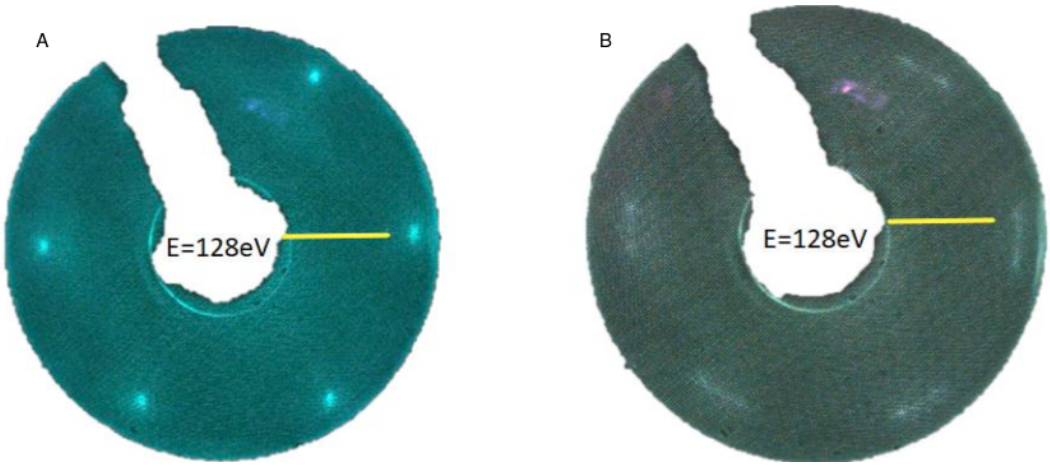

Figure 5.3: LEED pattern of the two samples at 128 eV - The spots measured at this energy are attributed to scattering from the Cu(111) film underlying the graphene layer, yellow line marks the scattering plane of the MMI

order to notice the graphene spots with the LEED, we needed to use low enough energy (about 70 eV), but as a consequence of the instrument geometry the spots were outside the LEED screen. As a solution to this problem we pointed the surface normal away from the LEED. This makes the specular (00 spot) visible and allows us to fit a few of the graphene spots within the screen field of view. Fig. 5.4 demonstrates the difference between the two samples with a (00) notation for the specular peak. In sample A we can notice a weak but still resolvable spot along the same azimuth of the copper spots (the yellow line added to the figure marks the scattering plane of the MMI setup). This spot lies along a weak ring feature with two (barely resolvable) additional weak spots 30 ° above and below it, in agreement with the observation of Al Talab et al. [58]. In contrast the LEED pattern of sample B is different, and we can only notice the higher

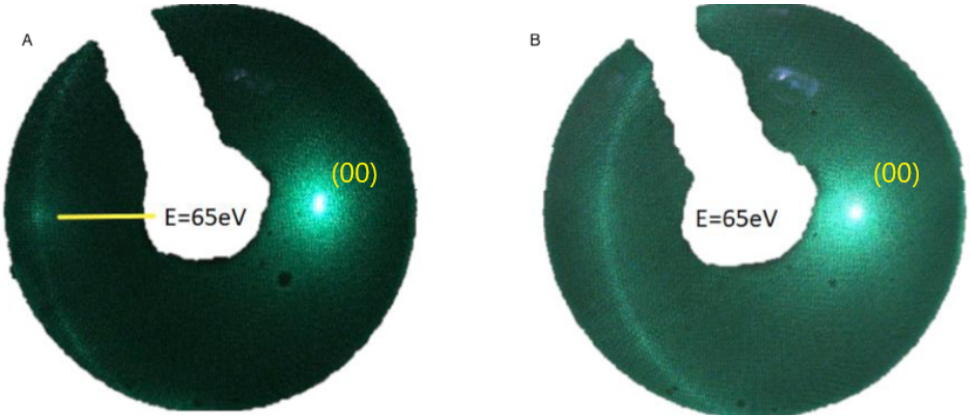

Figure 5.4: LEED pattern of the two samples - Measurements were taken at a surface temperature of 120 K and an electron energy of 70 eV. The arcs seem to correspond to scattering from the graphene surface, the yellow line marks the scattering plane of the MMI

intensity ring. This result is consistent with our previous measurement of this sample, i.e. that the Cu(111) film of sample B did not produce the simple single crystal pattern sample A produced. If indeed this indicates azimuthal disorder of the copper film, it is expected that the graphene layer grown on top of this film will also have reduced azimuthal order. After orienting the sample parallel to the $[1\bar{1}0]$ direction of the Cu(111) lattice, helium atom (^4He) scattering was performed on the sample, the position of the diffraction peaks in an angular scan allows us to quantitatively study the periodicity of the surface and compare with the periodicity we expect for a graphene layer. The nozzle temperature of the helium beam was 100 K. Angular scans of both samples were performed at a surface temperature of 100 K and are shown in Fig. 5.5. The measurement of sample A shows, in addition to the main specular reflection peak, two additional diffraction features which rise above the noise level. A hint for these peaks can also be seen in the scan from sample B, although it is less apparent. Fig. 5.6 shows the real and reciprocal lattice of graphene. The honeycomb structure of graphene can be described using a Bravais lattice with a two atom basis. The two different colours in red and blue, represent the different atoms (differing from each other by the position of their nearest neighbours). The direct and reciprocal lattice vector can

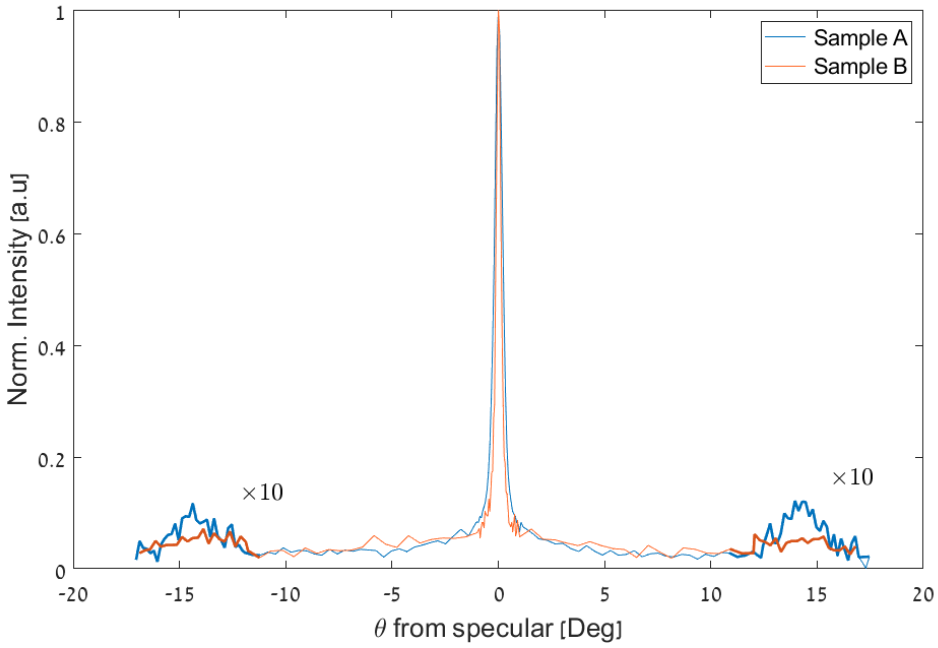

Figure 5.5: Helium angular scans for samples A and B - measured at 21 meV incident energy and 100 K surface temperature. The signals were normalised to the specular intensity and the region of the diffraction peaks (marked with thick lines,up to –11 ° and from 11 °) is multiplied by 10 so they can be noticed

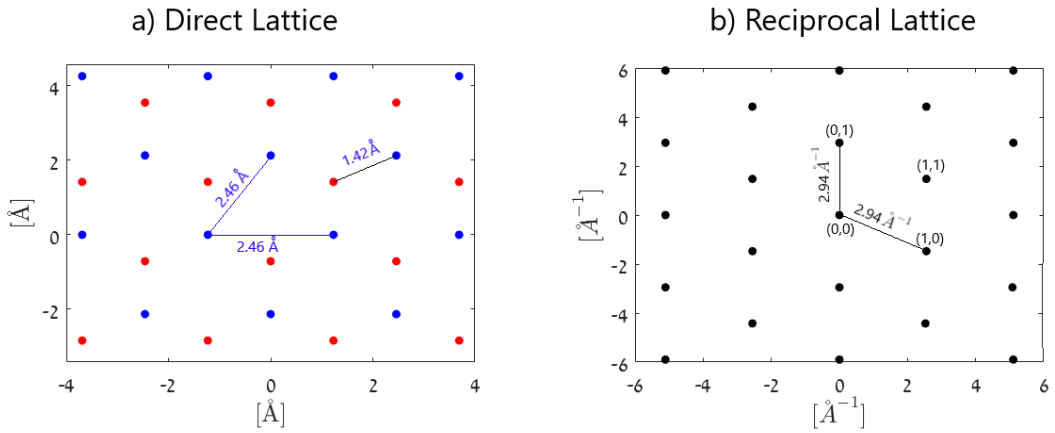

Figure 5.6: Real and reciprocal lattice of the graphene surface - with marks of the (h,k) indices and distances. The blue lines of 2.64 $\AA$ distance are the unit vectors of the direct lattice, the black lines in (b) are the reciprocal vectors. Dimensions are taken from [59]

be written as

$$\vec{a_1} = 2.46\hat{x}\,\mathring{A} \quad \vec{a_2} = 2.46(cos(\pi/3)\hat{x} + sin(\pi/3)\hat{y})\,\mathring{A} \tag{5.1}$$

$$\vec{b_1} = 2\pi\frac{\hat{a_2}\times\vec{z}}{|\vec{a_1}\times\vec{a_2}|} = 2.55(\hat{x} - \frac{1}{\sqrt{3}}\,\hat{y})\,\mathring{A}^{-1} \tag{5.2}$$

$$\vec{b_2} = 2\pi\frac{\hat{z}\times\vec{a_1}}{|\vec{a_1}\times\vec{a_2}|} = \frac{5.1}{\sqrt{3}}\,\hat{y}\,\mathring{A}^{-1} \tag{5.3}$$

where $\vec{a_1}$, $\vec{a_2}$ are the direct lattice vector and $\vec{b_1}$, $\vec{b_2}$ are the reciprocal lattice vectors. We now can write down $\vec{G} = h\vec{b_1} + k\vec{b_2}$ as

$$\vec{G} = 2.55(k\hat{x} + \frac{1}{\sqrt{3}}(2h-k)\hat{y})\,\mathring{A}^{-1}. \tag{5.4}$$

To find out the expected position of the diffraction peak in the case of the graphene surface, we equate the length of the G vector, which in the case of (h,k)=(1,0) is $|\vec{G}| = 2.95\,\mathring{A}^{-1}$ and the change in the wave vector. The magnitude of the wave vector for a beam of neutral helium beam created by a 100 K of nozzle is $|\vec{k_i}| = 6.42\,\mathring{A}^{-1}$ (according to Eq. 4.2). Using these values in Eq. 4.5, we need to solve

$$(sin(\Delta-\gamma) - sin(\gamma)) = \frac{|\vec{G}|}{|\vec{k_i}|} = 0.46, \tag{5.5}$$

where Δ is the angle between the two arms of the machine and γ is the polar angle. Solving for γ gives a diffraction peak at -14.4 ° from specular and due to the lattice symmetry we shall expect another diffraction peak correspond to +14.4 ° from specular. The position of the diffraction peaks in the angular scan of sample A, shown in Fig. 5.5 are consistent with this calculation, indicating that indeed the diffraction peaks are from the graphene layer. A detailed explanation on how to derive the position of the diffraction peaks from a known unit cell has been presented in the previous chapter in section 4.2. Fig. 5.5 also shows that the specular width (FWHM) of the samples differs by almost factor of two, FWHM(A)=0.5 ° FWHM(B)=0.3 °. As both of these values are much larger than the angular resolution of the setup, they can be associated with the density of defects and the size of the flat domains, where a narrower specular indicates larger flat domains in between defects. The fact that sample

B produced an azimuthally disordered LEED pattern of the Cu(111) film, and a graphene diffraction peak which is much weaker than that of sample A, has a narrower specular which suggest larger domains seems surprising. We will address this apparent contradiction later. After establishing the alignment of the surface (sample A) and verifying that we are scattering from a graphene surface by neutral helium atom scattering, we switched to a H_2 beam, using a nozzle temperature of 100 K and performed scattering experiments. We discovered that the scattered intensity with H_2 is the limiting factor, and our specular intensities were barely detected above the background level. The reason for the low specular signal, in comparison with LiF(001) surface is probably related to the high density of defect in the graphene surfaces we studied. Fig. 5.7 shows the H_2 specular intensity of the samples and as can be seen, the specular width of sample B is wider than sample A which follows the trend seen for ^4He scattering. As no diffraction peaks were found when using a H_2 beam, we have used

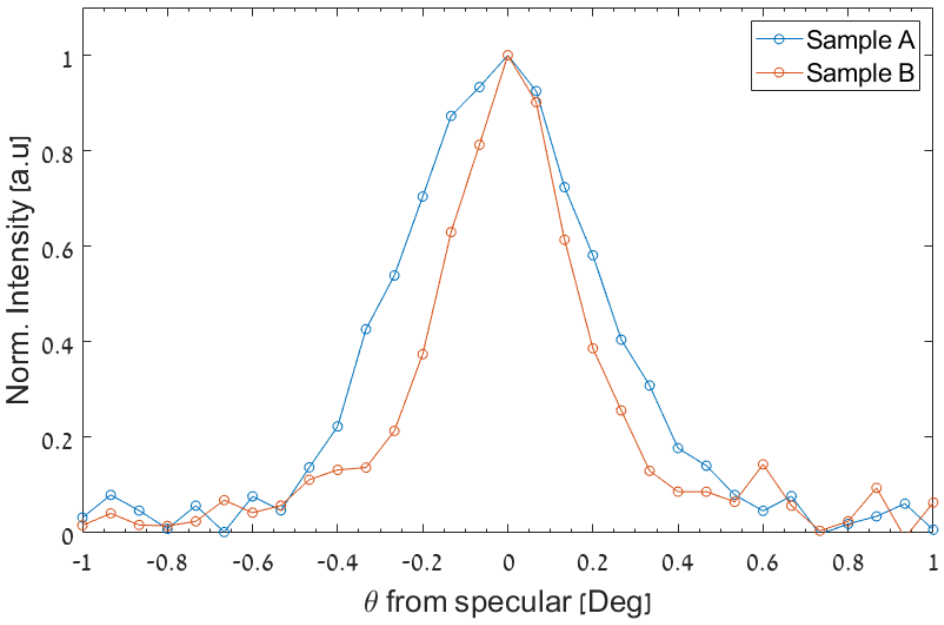

Figure 5.7: Comparison of H_2 specular peaks of samples A and B (normalised intensity) - the angular polar scan of the surfaces were performed for sample and nozzle temperatures of 100 K. The comparison demonstrates the difference in specular peak width between the two samples.

the specular peak to perform the rotational control experiments presented below, measurements which were performed by fixing the second magnetic field at B2=0 or 0.05 A and scanning B1. The comparison of these scans for both samples is presented in Fig. 5.8. In Fig. 5.8 we can clearly notice that the signal decays

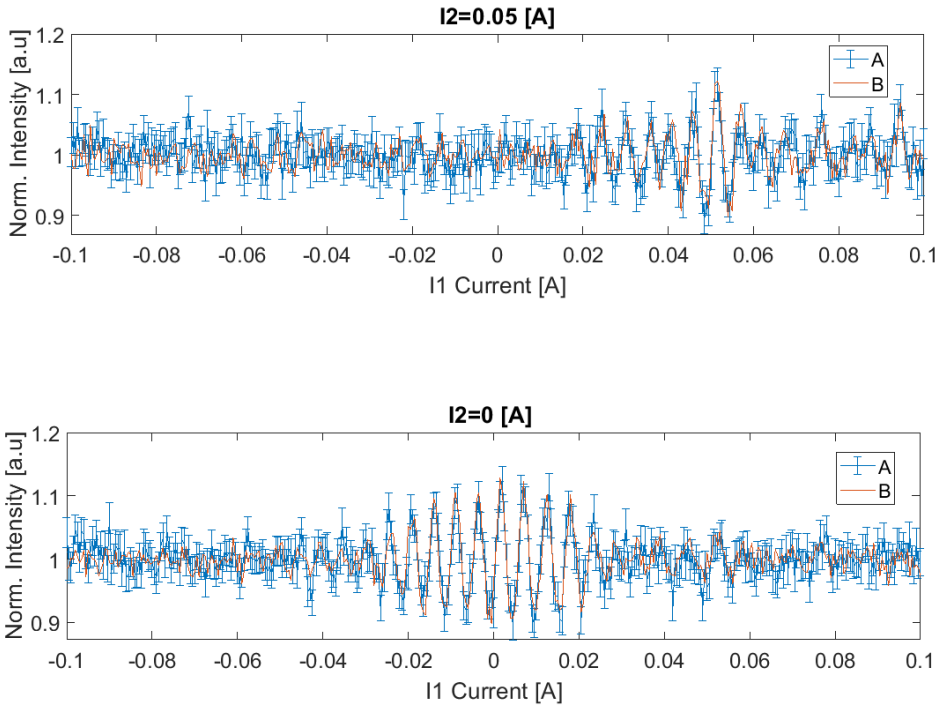

Figure 5.8: H_2 **Current scans** - comparison of sample A and B at two different values of the second solenoid (0.05 A in the upper figure and 0 A in the lower one), the error bars on the sample A data mark the standard deviation of each data point average.

much faster (lower B1 fields) in comparison with the measurements presented in the previous chapter for H_2/LiF. This is expected and is simply related to the fact that on LiF we performed the measurements on diffraction peaks which essentially act as monochromators. For graphene they were performed on specular, hence the full velocity distribution of the beam contributes to the signal, leading to a quicker dephasing of the magnetisation (dephasing of the coherency of the signal). A second point to notice is that there is no obvious difference between the two samples to within the experimental noise.

Due to technical issues, the measurements of sample A and sample B, shown in Fig. 5.8 were performed at two different temperatures, 180 K for sample A and 120 K for sample B. However, sample A has been also measured at a much lower temperature, 60 K, and the comparison shown in Fig. 5.9 indicates that the oscillation curves do not depend significantly on the surface temperature. In addition to making the comparison between the samples more meaningful, the results shown in Fig. 5.9 also suggests that the oscillation pattern is dominated by static effects, i.e. the structure of the surface and the molecule-surface potential rather than dynamic effects due to phonons and energy exchange at the surface. As our main interest is to extract information about the scattering pro-

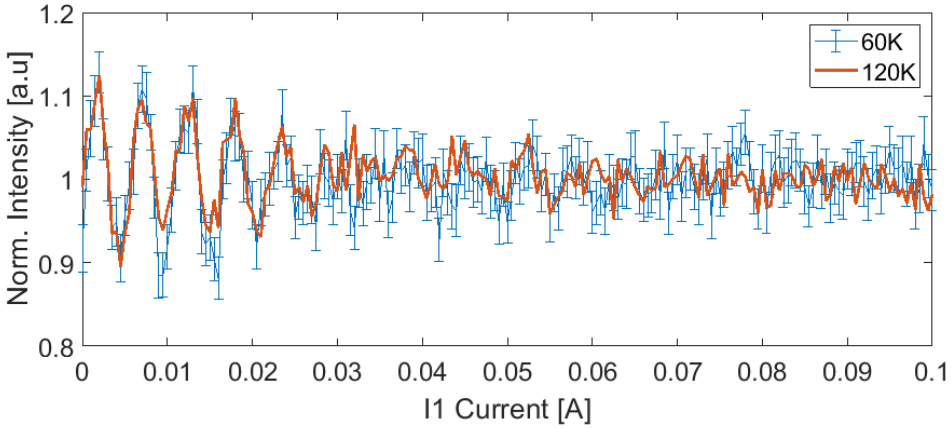

Figure 5.9: H_2 **Current scans comparison** - at surface temperatures of 60 and 120 Kelvin, the error bars on the 60 K data mark the standard deviation of each data point average.

cess from the measurements, we want to find a suitable scattering matrix so that our calculation will agree with the measured signals. In Chapter 4, we showed an example of how the scattering matrix elements can be extracted from fitting the measured oscillation curves. There are several challenges stopping us from doing the same with the H_2/Graphene data, which are related to the fact that measuring at specular condition means that a wide range of velocities is contributing to the experimental data, as opposed to diffraction condition which selects a very narrow range of velocities. To simulate the data we have to assume a velocity independent scattering matrix within the range of velocities in

the experiment, and average the signal from all the velocity contributions. The velocity independent scattering matrix approximation becomes less valid as the velocity width increases, this means that while the approximation might work well for diffraction peaks it won't necessarily be a good approximation for specular measurements. Furthermore, the fact that the signal decays quicker (at lower values of B1), reduces the amount of useful data used in the fit process reducing the chance of getting unique matrix values. Finally, averaging over a wider range of velocities is expensive in terms of computational time.

An alternative to fitting, is to compare the data to simulations of a scattering matrix which is either calculated from a molecule-surface interaction model [14], if they exist for the system we measured (which is not the case for H_2/Graphene), or chose the matrix using some other considerations. In Figure 5.10 we compare the results with an identity matrix, i.e. a matrix which treats the scattering event as a mirror. We would expect this matrix to produce a good fit if the surface potential cannot distinguish between the different rotational projection states of the H_2 molecules in the beam, in terms of the elastic, specular-scattering event. To produce the simulated signal we used a hydrogen beam with a mean velocity of 1445 m/s and 8% FWHM and propagated the m_I, m_J, states along our apparatus up to the surface position, we then applied the rotations and scattering matrix similarly to what we did for H_2/LiF (Chapter 4) and from the surface onwards we again propagated the wave functions using our known magnetic field profile up to hexapole analyser and calculated the signal. The measurements and calculations shown in Fig. 5.10 were performed for two different values of current in the second solenoid and demonstrate good agreement between the calculation and the measured signal. We chose sample B in the comparison due to its relatively low noise. We now compare the experimental magnetic scans results to a similar experiment performed when scattering H_2 from Cu(111) surface. The top panel in Fig. 5.11, shows a direct comparison of the measurements, they seem similar but shifted with respect to each other. The lower panel demonstrates that shifting the copper by 0.0007 A , makes the measurements practically identical within the experimental noise. The Cu(111) measurement was performed approximately six month before the graphene measurements, and we believe the mismatch is related to a change of calibration of the current power supply driving the second

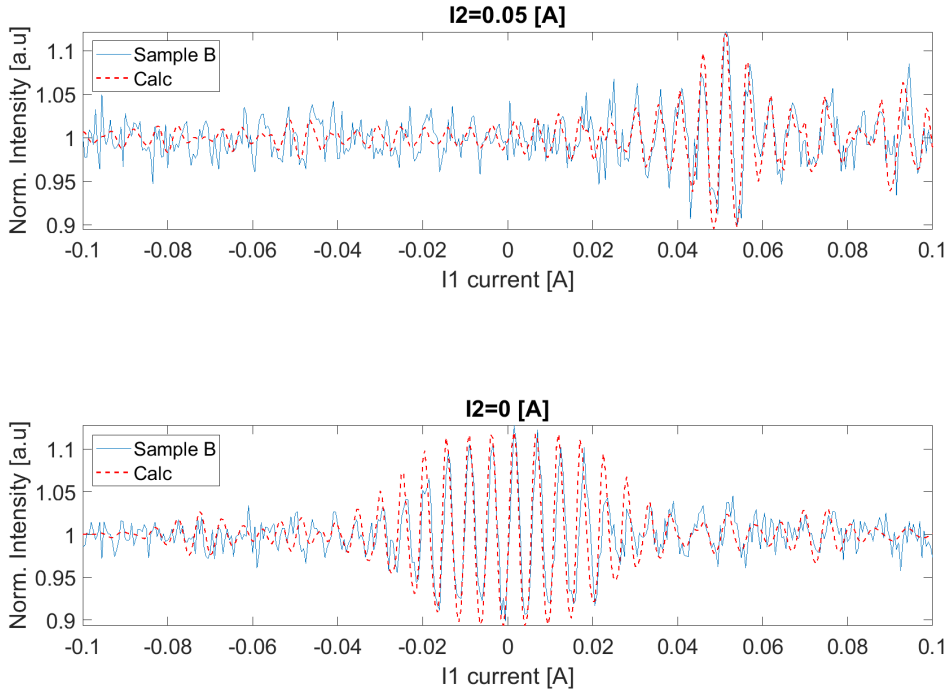

Figure 5.10: Comparison of calculations and measurements for graphene - measurements of sample B alongside a scattering calculation performed using an identity scattering matrix

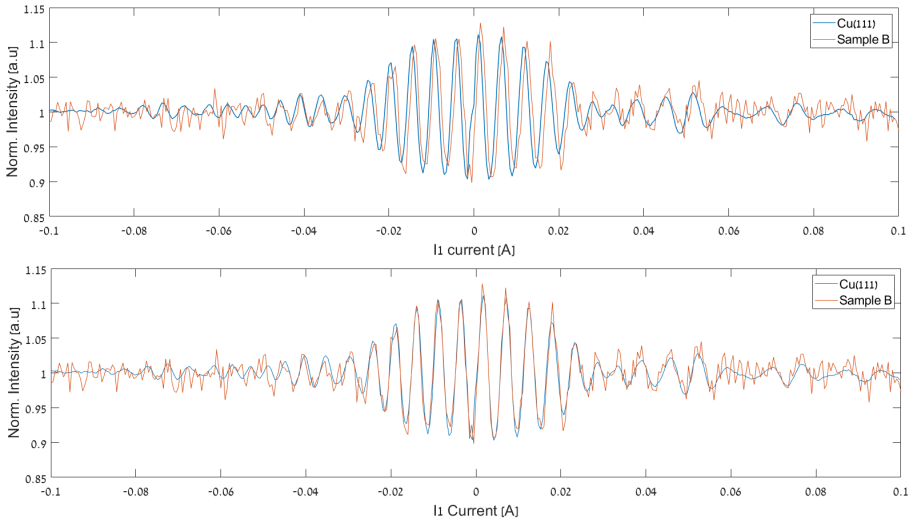

Figure 5.11: Comparison between graphene and Cu(111) magnetic scans - The top panel shows both measurements as they were taken. The second panel shows the Cu(111) measurement shifted by 0.0007 A to compensate for the different calibration the second solenoid was set to in the different measurements, see text for further details

coil which led to a residual current of 0.0007 A. While further measurements will be required to test this assumption, if it is the case, the mirror like scattering of graphene is very similar to what is observed on Cu(111).

To check whether the resemblance of the measured oscillation curves of H_2/Graphene and the signal calculated using a unity (mirror like) scattering matrix is a general phenomena related to specular measurements, perhaps related to the averaging over a wide range of energies, we compare them with measurements of H_2 scattering from LiF(001), also measured in specular conditions. Fig. 5.12 compares the two experimental data sets alongside the calculation for a unity scattering matrix. As can be seen, the H_2/LiF data is really quite different, showing that the mirror like scattering is related to the structure of the graphene surface and the way it interacts with the H_2 molecules.

To interpret our findings, we look at the various results presented in this chapter. The LEED and HAS results suggest that the two samples we studied differ in terms of the azimuthal order of the Cu(111) layer (A more ordered than B), both of them produce features related to the unit cell of graphene, but again

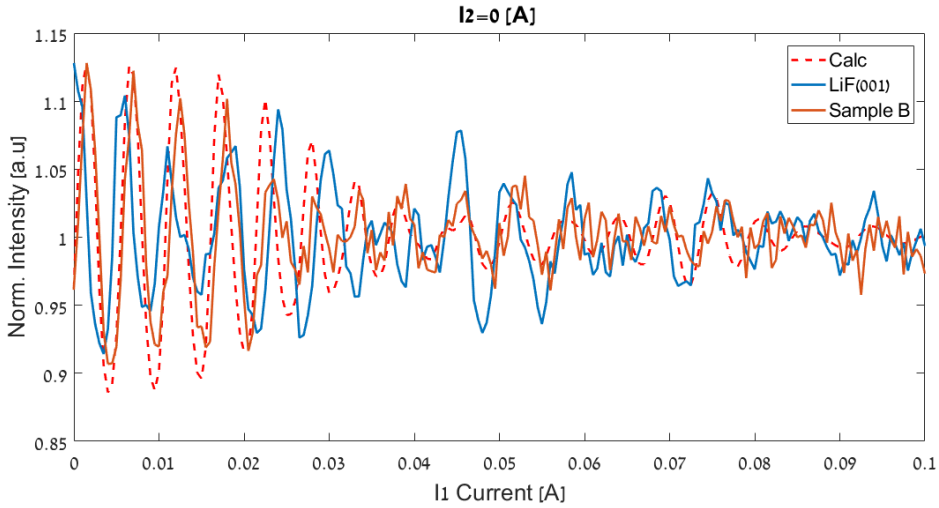

Figure 5.12: Comparison of graphene(sample B) and LiF(001) measurements to a mirror scattering calculation - Both measurements were performed for specular scattering.

these seem to have some azimuthal order in sample A and not in B. In contrast the specular peak of sample B (helium and hydrogen scattering) is narrower, indicating that the flat regions contributing to the specular signal are actually larger than those in sample A.

One possible explanation which allows for these two apparently conflicting results to be consistent, is if there are exposed Cu(111) regions which contribute significantly to the specular intensity. If such regions are actually larger in sample B this would make the specular signal stronger and narrower. Unlike the specular, the (much smaller) diffraction peaks are necessarily linked to the graphene structure. Since larger exposed Cu(111) regions could be linked to smaller graphene covered regions, we would expect a reduction in the diffraction peak intensity and perhaps also the azimuthal order of the graphene layer.

The possible explanation given above, means that from the measurements we performed we cannot distinguish between two different scenarios. One is that the scattering from a graphene layer produces a signal which is very similar to mirror scattering (unity scattering matrix), which means that the dependence of the interaction potential of H_2/graphene on the rotational projection state is very weak. Another scenario which cannot be excluded is that the specular

intensity we are following as function of B1, is actually attributed to exposed Cu(111) regions, and the lack of rotational projection dependence is related to the H_2/Cu(111) interaction.

To fully understand the interaction between the H_2 quantum rotational states and a graphene surface one should try and investigate more metal surfaces with a graphene layer, ideally systems where the layer is grown in-situ, to see whether the specular scattering is the same with or without the graphene overlayer. Furthermore, growing a graphene layer that allows a magnetic scan of the diffraction peaks will give a much better understanding of the scattering process as we will be sure that the scattering itself comes from the carbon atoms, and also allow us to work with a much narrower range of energies making it possible to determine the scattering matrix more reliably.

Finally, further measurements of H_2/Cu(111) are needed to verify that the phase shift between the two data sets arises from a current calibration issue rather than a real difference in the scattering properties of the two surfaces

6

Outlook and summary

6.1 Direct beam analysis

In this thesis I have described the design and implementation of a unique extension to the magnetic molecular interferometry scattering machine. This extension allows us to measure the molecular beam directly (without scattering), after manipulating the quantum states of the ground state molecules using the homogenous magnetic field of the first arm of the scattering machine. The improved setup can be used to test and verify the properties of the magnetic hexapoles which are used to separate the different quantum states in space and create a bias in the quantum state populations within the beam, as well as perform state selective particle detection. The setup can also be used to verify the profile of the magnetic fields along the beam line. The ability to coherently control the rotational states of a ground state hydrogen molecular beam has been demonstrated together with the ability to calculate signals which are in good agreement with the measured signals. The spatial intensity distribution of $^3He, D_2$ and H_2 beams at the detector shows that the beam trajectory calculations through the machine are valid and reproduce the various trends seen in the measured intensity profiles. The ^3He experiments, which use a simple atomic beam with relatively simple spin 1/2 dynamics, allowed us to identify a small residual magnetic field which the full magnetic field measurements were unable to detect and the method for that was described in detail. Correcting the magnetic field profile of the machine accordingly, shows an unquestionable improvement and agreement between the

calculation and the measurements. Some disagreement can still be seen between the measurements and the calculations, possibly due to imperfect alignment of the beam line and the hexapole lenses. In the future, it would be useful to fine tune the magnetic lenses alignment, using 2-D profile intensity scans as feedback. Hopefully this will further improve the similarity of the calculations and the measurements.

Further applications of the direct beam extension:

One use of the setup is to determine the magnetic Hamiltonian constants for molecules where these are still unknown or require experimental benchmarking, for example, the various isotopologues of H_2O. Another future application is using the direct beam extension to both determine and optimize the beam conditions for scattering experiments. For example, seeded beams, combined with higher nozzle temperatures, could be used to increase the populations of excited rotational states of H_2 and D_2, while maintaining low enough beam velocities for the magnetic lens to be capable of focusing the beam. The ability to control the rotational projection states of excited rotational states, opens up the possibility of studying stereodynamic effects in rotationally inelastic molecule-surface scattering experiments. The direct beam system presented in this thesis has only one magnetic solenoid to control the magnetic field on the beam's path. Introducing a secondary magnetic solenoid further away from the first and separated by a zero magnetic field region will allow for multiple echos [60] at magnetic field higher than zero to be measured. This will also make the system capable of investigating gas collisions, with several modifications of the scattering chamber.

6.2 Surface scattering experiments

A new technique, capable of extracting the scattering matrix from a diffraction scattering magnetic scans was introduced. The measurements of H_2 molecules scattering from a LiF(001) surface have been used to determine the scattering matrices of the different diffraction channels. The results from these measurements

show that the different quantum rotational projection states are scattered differently, which means that this particular surface can be used as a beam polariser. It would be interesting to check the polarization properties of other surface. Good candidates for this would be surfaces with high intensity H_2 scattering diffraction peaks. Preliminary unpublished work in our group of H_2 scattered from a NaCl surface showed high intensity diffraction peaks and clear bound state resonance features at some nozzle temperatures. Performing magnetic scans and extracting the scattering matrix from the diffraction peaks for energies which exhibit bound state resonances could be a fruitful path of study, allowing us to study the stereodynamics of the bound state resonance phenomena. Furthermore, our previous study of H_2/(Cu115) [61] showed that specular scattering strongly depends on the rotational projection states of the molecules. This system is also characterized by high intensity diffraction peaks, however magnetic scans were not measured for diffraction scattering and no attempt have been made for extracting the corresponding scattering matrix elements. Performing such measurements and extracting these values would provide insight into the interaction of H_2 molecules with the different sites of this stepped copper surface.

The magnetic scan measurements of H_2 scattering from a graphene covered Cu(111) surface lead to a surprising result, where the oscillation curve can be explained by simulating the experiment with an identity matrix as a scattering matrix, i.e. mirror scattering. This type of scattering matrix represents the case where the scattering probability does not depend on the rotational projection states of the incident beam. The same phenomena also occurs for the case of H_2 specular scattering from the bare Cu(111) surface. In both cases there was not enough scattered intensity in the diffraction peak and the measurements had to be performed on the specular scattering peak. One possibility is that there is a relation between the two properties, i.e. surfaces which have very low diffraction peak intensities in comparison with specular scattering (which is consistent with a very weak corrugation of the molecule-surface potential), tend to not be sensitive to the rotational orientation of molecules. Another option is that when measuring at the specular condition, our signal might be coming from the exposed substrate rather than the graphene layer, this would explain the similarity of the magnetic scan curves. Unfortunately, we are unable to distinguish the two scenarios.

Nickel and Ruthenium surfaces can be suitable systems for growing graphene layers on, where both Ni(111) and Ru(0001) surfaces demonstrated high ^4He reflectivity[58, 62, 63]. While this higher reflectivity corresponds to the specular peak rather than the diffraction peak intensity, it does suggest that the defect density might be smaller than the density in the samples we studied. If indeed the defect density is smaller, and the size of the perfect graphene domains is larger, this might make current scan measurements on diffraction peaks possible. The separation distance between the graphene layer on Ni(111) and Ru(0001) and the substrate was measured to be 0.21 nm, in comparison with a distance of 0.33 nm for Cu(111)[64], indicating a stronger interaction between the graphene and Ni and Ru surfaces. As Ru and Ni are reactive to hydrogen, the surface temperature will need to be above the sticking temperature [65] (ca. 500 K) while measuring the surfaces without a graphene layer. This is not the case for the Cu(111) surface as it is not reactive to hydrogen. It will be interesting to perform magnetic scans on the specular diffraction of H_2 from a graphene layer on top of those surfaces, and compare the results with those presented in this thesis. Comparing different graphene surfaces, which potentially have different levels of diffraction intensities and potential corrugation, will allow us to see if there are any obvious trends relating the diffraction intensity and the sensitivity to the rotational projection states. Furthermore, the suggested systems might have enough H_2 intensity in diffraction peaks other than specular to perform magnetic scans. Magnetic scans of the diffraction intensity signal can be unambiguously related to the graphene layer rather than to any exposed substrate regions. They are also characterized by a much narrower velocity spread of the scattered beam, allowing a much more detailed investigation, similarly to the H_2/LiF study presented in this thesis. Obtaining such data will provide a benchmark for modeling the interaction of H_2 with a graphene layer.

References

[1] Herbst, E., Chang, Q. & Cuppen, H. (2005). Chemistry on interstellar grains. In *Journal of Physics: Conference Series*, vol. 6, 002, IOP Publishing. ii, 1

[2] Logadóttir, Á. & Nørskov, J.K. (2003). Ammonia synthesis over a Ru(0001) surface studied by density functional calculations. *Journal of Catalysis*, **220**, 273–279. ii, 1

[3] Ramsey, N.F. (1952). Theory of molecular hydrogen and deuterium in magnetic fields. *Physical Review*, **85**. x, 19, 23, 89, 90, 95

[4] Schleder, G.R., Padilha, A.C., Acosta, C.M., Costa, M. & Fazzio, A. (2019). From dft to machine learning: recent approaches to materials science–a review. *Journal of Physics: Materials*, **2**, 032001. 1

[5] Smith Jr, J.N. (1973). Molecular beam scattering from solid surfaces: A critical review. *Surface Science*, **34**, 613–637. 1

[6] Sitz, G.O. (2002). Gas surface interactions studied with state-prepared molecules. *Reports on Progress in Physics*, **65**, 1165. 1, 14

[7] Farias, D. & Rieder, K.H. (1998). Atomic beam diffraction from solid surfaces. *Reports on Progress in Physics*, **61**, 1575. 2

[8] Brusdeylins, G., Doak, R.B. & Toennies, J.P. (1981). Measurement of the Dispersion Relation for Rayleigh Surface Phonons of LiF(001) by Inelastic Scattering of He Atoms. *Physical Review Letters*, **46**, 437. 2

[9] Van De Meerakker, S.Y., Bethlem, H.L. & Meijer, G. (2008). Taming molecular beams. *Nature Physics*, **4**, 595–602. 2

[10] Alexandrowicz, G. & Jardine, A.P. (2007). Helium spin-echo spectroscopy: studying surface dynamics with ultra-high-energy resolution. *Journal of Physics: Condensed Matter*, **19**, 305001. 2

[11] Jardine, A., Hedgeland, H., Alexandrowicz, G., Allison, W. & Ellis, J. (2009). Helium-3 spin-echo: Principles and application to dynamics at surfaces. *Progress in Surface Science*, **84**, 323–379. 2

[12] Jardine, A., Alexandrowicz, G., Hedgeland, H., Allison, W. & Ellis, J. (2009). Studying the microscopic nature of diffusion with helium-3 spin-echo. *Physical Chemistry Chemical Physics*, **11**, 3355–3374. 2

[13] Saalfrank, P. & Miller, W.H. (1993). Time-independent quantum dynamics for diatom–surface scattering. *The Journal of Chemical Physics*, **98**. 4

[14] Mowrey, R. & Kroes, G. (1995). Application of an efficient asymptotic analysis method to molecule–surface scattering. *The Journal of Chemical Physics*, **103**, 1216–1225. 4, 128

[15] Bartlett, N.C.M., Miller, D.J., Zare, R.N., Alexander, A.J., Sofikitis, D. & Rakitzis, T.P. (2009). Time-dependent depolarization of aligned HD molecules. *Physical Chemistry Chemical Physics*, **11**, 142–147. 7, 90

[16] Kurahashi, M. & Yamauchi, Y. (2015). Spin Correlation in O_2 Chemisorption on Ni(111). *Physical Review Letters*, **114**, 016101. 7

[17] Kurahashi, M. & Kondo, T. (2019). Alignment-resolved O_2 scattering from highly oriented pyrolytic graphite and LiF(001) surfaces. *Physical Review B*, **99**, 045439. 8

[18] Kurahashi, M. (2021). Use of hexapole magnet and spin flipper combined with time-of-flight analysis to characterize state-selected paramagnetic atomic/molecular beams. *Review of Scientific Instruments*, **92**, 013201. 8

[19] Hou, H., Gulding, S., Rettner, C., Wodtke, A. & Auerbach, D. (1997). The Stereodynamics of a Gas-Surface Reaction. *Science*, **277**, 80–82. 8

[20] Yoder, B.L., Bisson, R. & Beck, R.D. (2010). Steric Effects in the Chemisorption of Vibrationally Excited Methane on Ni(100). *Science*, **329**, 553–556. 8, 115

[21] Bartels, N., Golibrzuch, K., Bartels, C., Chen, L., Auerbach, D.J., Wodtke, A.M. & Schäfer, T. (2013). Observation of orientation-dependent electron transfer in molecule–surface collisions. *Proceedings of the National Academy of Sciences*, **110**, 17738–17743. 9

[22] Hodgson, A. (2000). State resolved desorption measurements as a probe of surface reactions. *Progress in Surface Science*, **63**. 14

[23] Cole, M.W. & Frankl, D.R. (1978). Atomic and molecular beam scattering from crystal surfaces in the quantum regime. *Surface Science*, **70**, 585–616. 14

[24] Park, G.B., Krüger, B.C., Borodin, D., Kitsopoulos, T.N. & Wodtke, A.M. (2019). Fundamental mechanisms for molecular energy conversion and chemical reactions at surfaces. *Reports on Progress in Physics*, **82**, 096401. 14

[25] Rendulic, K. & Winkler, A. (1994). Adsorption and desorption dynamics as seen through molecular beam techniques. *Surface science*, **299**, 261–276. 14

[26] Scoles, G. (1988). *Atomic and Molecular Beam Methods / Vol.1.*. Oxford University Press, New York. 14, 15

[27] Schmidt-Böcking, H., Schmidt, L., Lüdde, H.J., Trageser, W., Templeton, A. & Sauer, T. (2016). The Stern-Gerlach experiment revisited. *The European Physical Journal H*, **41**, 327–364. 17

[28] van de Meerakker, S.Y., Bethlem, H.L., Vanhaecke, N. & Meijer, G. (2012). Manipulation and Control of Molecular Beams. *Chemical Reviews*, **112**, 4828–4878. 17

[29] Jardine, A., Fouquet, P., Ellis, J. & Allison, W. (2001). Hexapole magnet system for thermal energy ^{3}He atom manipulation. *Review of Scientific Instruments*, **72**, 3834–3841. 17, 42

[30] Utz, M., Levitt, M.H., Cooper, N. & Ulbricht, H. (2015). Visualisation of quantum evolution in the Stern-Gerlach and Rabi experiments. *Physical Chemistry Chemical Physics*, **17**. 18, 90

[31] Litvin, I., Alkoby, Y., Godsi, O., Alexandrowicz, G. & Maniv, T. (2019). Parallel and anti-parallel echoes in beam spin echo experiments. *Results in Physics*, **12**. 21

[32] Cantin, J.T., Alexandrowicz, G. & Krems, R.V. (2020). Transfer-matrix theory of surface spin-echo experiments with molecules. *Physical Review A*, **101**, 062703. 23

[33] Nelder, J.A. & Mead, R. (1965). A simplex method for function minimization. *The Computer Journal*, **7**. 24, 97

[34] Ramsey, N.F. & Trischka, J. (1957). Molecular Beams. *American Journal of Physics*, **25**. 25

[35] Alderwick, A.R., Jardine, A.P., Hedgeland, H., MacLaren, D.A., Allison, W. & Ellis, J. (2008). Simulation and analysis of solenoidal ion sources. *Review of Scientific Instruments*, **79**. 35

[36] Bergin, M., Ward, D.J., Lambrick, S.M., von Jeinsen, N.A., Holst, B., Ellis, J., Jardine, A.P. & Allison, W. (2021). Low-energy electron ionization mass spectrometer for efficient detection of low mass species. *Review of Scientific Instruments*, **92**. 35

[37] Chambers, A. (1998). *Basic Vacuum Technology*. CRC Press. 39, 41

[38] Hillenkamp, M., Keinan, S. & Even, U. (2003). Condensation limited cooling in supersonic expansions. *The Journal of Chemical Physics*, **118**, 8699–8705. 42

[39] Mikhlin, S.G. (1967). *Approximate methods for solution of differential and integral equations p.23*. Modern Analytic and Computational Methods in Science and Mathematics ; 5, American Elsevier, New York. 43

[40] Krüger, C., Lisitsin-Baranovsky, E., Ofer, O., Turgeon, P.A., Vermette, J., Ayotte, P. & Alexandrowicz, G. (2018). A magnetically focused molecular beam source for deposition of spin-polarised molecular surface layers. *Journal of Chemical Physics*, **149**. 44

[41] Fouquet, P., Jardine, A., Dworski, S., Alexandrowicz, G., Allison, W. & Ellis, J. (2005). Thermal energy ^{3}He spin-echo spectrometer for ultrahigh resolution surface dynamics measurements. *Review of Scientific Instruments*, **76**, 053109. 48

[42] Dworski, S., Alexandrowicz, G., Fouquet, P., Jardine, A., Allison, W. & Ellis, J. (2004). Low aberration permanent hexapole magnet for atom

and molecular beam research. *Review of Scientific Instruments*, **75**, 1963–1970. 51

[43] Dworski, S. (2003). Atom optical methods for surface studies. *PhD Thesis, University of Cambridge*, 82–94. 52

[44] Alexandrowicz, G. (2005). Helium spin echo spectroscopy : measuring the dynamics of atoms, molecules and surfaces. *PhD Thesis, University of Cambridge*, 55–58. 59

[45] Pijper, E. & Kroes, G.J. (1998-1-19). New predictions on magnetic rotational transitions in scattering of H_2 by LiF(001). *Physical Review Letters*, **80**. 81, 114

[46] Brusdeylins, G., Doak, R.B. & Toennies, J.P. (1983-3-15). High-resolution helium time-of-flight studies of rayleigh surface-phonon dispersion curves of LiF, NaF, and KCl. *Physical Review*, **27**. 84

[47] Wolken Jr, G. (1973). Collision of a diatomic molecule with a solid surface. *The Journal of Chemical Physics*, **59**, 1159–1165. 114

[48] Boato, G., Cantini, P. & Mattera, L. (1976). Elastic and rotationally inelastic diffraction of hydrogen molecular beams from the (001) face of LiF at 80°K. *The Journal of Chemical Physics*, **65**, 544–549. 114

[49] Horne, R. & Hermans, L. (1988). Large Rotational Polarization Observed for H_2, D_2, and HD Scattered from LiF(001). *Physical Review Letters*, **60**, 2777. 114

[50] Horne, R. & Hermans, L. (1991). Role of corrugation in molecule-surface interaction: flow experiments using the LiF(001) surface in two orientations. *Chemical Physics Letters*, **179**, 58–62. 114

[51] Cueto, M.d., Zhou, X., Muzas, A.S., Diaz, C., Martin, F., Jiang, B. & Guo, H. (2019). Quantum Stereodynamics of H_2 Scattering from Co (0001): Influence of Reaction Channels. *The Journal of Physical Chemistry C*, **123**, 16223–16231. 114

[52] Luntz, A., Kleyn, A. & Auerbach, D. (1982). Observation of rotational polarization produced in molecule-surface collisions. *Physical Review B*, **25**, 4273. 114

[53] Sitz, G.O., Kummel, A.C. & Zare, R.N. (1988). Direct inelastic scattering of N_2 from Ag(111). I. Rotational populations and alignment. *The Journal of Chemical Physics*, **89**, 2558–2571. 114

[54] Sitz, G.O., Kummel, A.C., Zare, R.N. & Tully, J.C. (1988). Direct inelastic scattering of N_2 from Ag(111). II. Orientation. *The Journal of Chemical Physics*, **89**, 2572–2582. 114

[55] Vattuone, L., Gerbi, A., Rocca, M., Valbusa, U., Pirani, F., Vecchiocattivi, F. & Cappelletti, D. (2004). Stereodynamic Effects in the Adsorption of Ethylene onto a Metal Surface. *Angewandte Chemie International Edition*, **43**, 5200–5203. 115

[56] Cao, K., van Lent, R., Kleyn, A.W., Kurahashi, M. & Juurlink, L.B. (2019). Steps on Pt stereodynamically filter sticking of O_2. *Proceedings of the National Academy of Sciences*, **116**, 13862–13866. 115

[57] Dwivedi, S. (2022). Graphene based electrodes for hydrogen fuel cells: A comprehensive review. *International Journal of Hydrogen Energy*. 117

[58] Taleb, A.A., Yu, H.K., Anemone, G., Farías, D. & Wodtke, A.M. (2015). Helium diffraction and acoustic phonons of graphene grown on copper foil. *Carbon*, **95**. 118, 121, 136

[59] Gray, D., McCaughan, A. & Mookerji, B. (2009). Crystal Structure of Graphite, Graphene and Silicon. *Physics for Solid State Applications*, **6**, 730–732. 123

[60] Chadwick, H., Alkoby, Y., Cantin, J.T., Lindebaum, D., Godsi, O., Maniv, T. & Alexandrowicz, G. (2021). Molecular spin echoes; multiple magnetic coherences in molecule surface scattering experiments. *Physical Chemistry Chemical Physics*, **23**, 7673–7681. 134

[61] Godsi, O., Corem, G., Alkoby, Y., Cantin, J.T., Krems, R.V., Somers, M.F., Meyer, J., Kroes, G.J., Maniv, T. & Alexandrowicz, G. (2017). A general method for controlling and resolving rotational orientation of molecules in molecule-surface collisions. *Nature Communications*, **8**, 1–7. 135

[62] al Taleb, A., Anemone, G., Farías, D. & Miranda, R. (2016). Acoustic surface phonons of graphene on Ni(111). *Carbon*, **99**, 416–422. 136

[63] Politano, A., Borca, B., Minniti, M., Hinarejos, J., de Parga, A.V., Farías, D. & Miranda, R. (2011). Helium reflectivity and Debye temperature of graphene grown epitaxially on Ru(0001). *Physical Review B*, **84**, 035450. 136

[64] Dahal, A. & Batzill, M. (2014). Graphene–nickel interfaces: a review. *Nanoscale*, **6**, 2548–2562. 136

[65] Wijzenbroek, M. & Kroes, G. (2014). The effect of the exchange-correlation functional on H_2 dissociation on Ru(0001). *The Journal of Chemical Physics*, **140**, 084702. 136